

Hydrogen energy storage in porous media

Hashemi, L.

DOI

[10.4233/uuid:cd0f2c4b-45b8-44ca-b0b0-d58222254375](https://doi.org/10.4233/uuid:cd0f2c4b-45b8-44ca-b0b0-d58222254375)

Publication date

2024

Document Version

Final published version

Citation (APA)

Hashemi, L. (2024). *Hydrogen energy storage in porous media*. [Dissertation (TU Delft), Delft University of Technology]. <https://doi.org/10.4233/uuid:cd0f2c4b-45b8-44ca-b0b0-d58222254375>

Important note

To cite this publication, please use the final published version (if applicable).
Please check the document version above.

Copyright

Other than for strictly personal use, it is not permitted to download, forward or distribute the text or part of it, without the consent of the author(s) and/or copyright holder(s), unless the work is under an open content license such as Creative Commons.

Takedown policy

Please contact us and provide details if you believe this document breaches copyrights.
We will remove access to the work immediately and investigate your claim.

Hydrogen Energy Storage in Porous Media



Leila Hashemi

HYDROGEN ENERGY STORAGE IN POROUS MEDIA

HYDROGEN ENERGY STORAGE IN POROUS MEDIA

Dissertation

for the purpose of obtaining the degree of doctor
at Delft University of Technology,
by the authority of the RectorMagnificus prof.dr.ir. T.H.J.J. van der Hagen,
chair of the Board for Doctorates
to be defended publicly on
Tuesday 23rd January 2024 at 15:00 o'clock

by

Leila HASHEMI

Master of Science in Reservoir Management,
Petroleum University of Technology, Tehran, Iran,

born in Tehran, Iran.

This dissertation has been approved by the promotor.

Composition of the doctoral committee:

Rector Magnificus,	chairman
Prof. dr. ir. C. Vuik,	Delft University of Technology, promotor
Prof. dr. H. Hajibeygi,	Delft University of Technology, promotor

Independent members:

Prof. dr. ir. A.W. Heemink,	Delft University of Technology
Prof. dr. ir. T.J. Heimovaara,	Delft University of Technology
Prof. dr. M.J. Blunt ,	Imperial College London, UK
Prof. dr. K.E. Thompson,	University of Louisiana, US
Prof. dr. M.Prodanović,	University of Texas at Austin, US

Prof. dr. W.R. Rossen,	Delft University of Technology, reserve member
------------------------	--

This research work has been conducted with the support of the Adaptive Dynamic Multiscale Integrated Reservoir-Earth (ADMIRE) and the Delft Institute of Applied Mathematics (DIAM) groups.



Keywords: Energy storage, underground hydrogen storage, pore-scale simulation, quasi-static pore network modelling, dynamic pore network modelling, wettability, contact angle measurement

Printed by: Ridderprint | www.ridderprint.nl

Front & Back: Designed by Inmywork Studio

Copyright © 2023 by Leila Hashemi

ISBN 978-94-6384-530-4

An electronic version of this dissertation is available at <http://repository.tudelft.nl/>.

To my family

*Science is a wonderful thing
if one does not have to earn one's living at it.*

Albert Einstein

CONTENTS

Summary	ix
1 Introduction	1
1.1 Overview of Underground Hydrogen Storage	2
1.2 Motivation & Objectives.	5
2 Pore-scale modelling and sensitivity analyses	9
2.1 Introduction	10
2.2 Methods	12
2.3 Results	16
2.3.1 Test Case 1: benchmarking Pore-Network Modelling (PNM) and Corey functions	17
2.3.2 Test Case 2: Hysteretic upscaled transport functions for cyclic transport	17
2.3.3 Test Case 3: Impact of fluid properties on the hysteretic upscaled functions.	18
2.3.4 Test Case 4: Impact of rock properties on the hysteretic upscaled functions.	20
3 Contact Angle for Hydrogen/Brine/Sandstone System	25
3.1 Introduction	26
3.2 Methods and Materials	27
3.2.1 Materials.	27
3.2.2 Microscopic image analysis of rock samples	27
3.2.3 Experimental setup	27
3.2.4 Experimental procedure	28
3.2.5 Image analysis	28
3.2.6 Calibration of the setup	30
3.2.7 Summary of the test cases	31
3.3 Results and Discussion	31
3.3.1 Effect of bubble size on the contact angle	32
3.3.2 Test Case 1: Effect of pressure and temperature	32
3.3.3 Test Case 2: Effect of salinity	35
3.3.4 Test Case 3: Effect of rock type	35
3.4 Conclusions and Outlook	36
4 Contact Angle for mixtures of Hydrogen-Methane /Brine/Sandstone System	39
4.1 Introduction	40
4.2 Materials and Methods	42
4.2.1 Materials.	42

4.2.2	Experimental Apparatus and Procedure	43
4.2.3	Image analysis	43
4.2.4	Theoretical analyses based on Young-Laplace equation	43
4.3	Results and discussion	45
4.3.1	Effect of bubble size and gas composition	46
4.3.2	Effect of pressure, temperature and salinities	46
4.3.3	Sensitivity analysis of the captive-bubble cell approach	47
4.4	Conclusions.	48
5	Dynamic pore network model	53
5.1	Introduction	54
5.2	Methodology	55
5.2.1	Description of the pore space	56
5.2.2	Displacements and Transport properties	56
5.2.3	Two-phase flow modelling	59
5.3	Results and Discussion	62
5.3.1	Discussion	67
5.4	Conclusions and Recommendations	67
5.4.1	Conclusions	67
5.4.2	Recommendations.	68
6	Conclusions and future work	71
A	Overview of UHS projects and Simulation Data	75
B	Contact angle measurements for H₂-Brine	85
C	Contact angle measurements for mixture of (H₂-CH₄) - Brine	93
D	Developed dynamic pore network models	101
E	Pore network modelling (PNM)	105
E.1	The structure of the network data files for PNMs	106
E.1.1	Classical format (Statoil protocol)	106
E.1.2	DuMux format	108
E.2	Pore network modelling.	109
E.2.1	Description of the Pore Space	110
E.2.2	Flow process: Drainage and Imbibition	112
E.2.3	Threshold capillary pressures	113
E.2.4	Transport Properties	116
	References	119
	Curriculum Vitæ	135
	Scientific Contributions	137
	Acknowledgements	139

SUMMARY

The demand for sustainable and clean energy sources has become increasingly vital in addressing the challenges of climate change and energy security. Hydrogen, with its high energy density and potential for carbon-free energy conversion, has emerged as a promising candidate for future energy systems. Efficient storage and retrieval of hydrogen are crucial for its widespread utilization, for which a promising approach is underground hydrogen storage in geological porous media. This thesis aims to explore and advance the understanding of hydrogen storage in geological porous media, specifically focusing on pore-scale modeling and contact angle analysis.

This research aims to overcome the limitations of current hydrogen storage methods and develop more efficient energy storage systems. Porous materials like sandstones have special characteristics that make them suitable for storing hydrogen underground. To design and operate underground hydrogen storage on a large scale, it is important to understand how fluids move through these materials. The way hydrogen is stored and released is influenced by complex processes happening at a very small scale (μm). To accurately simulate these processes, we need to study how fluids move in the pores, including factors like capillary pressure (the pressure difference between nonwetting and wetting phases, which is one of the main forces acting at pore scale transport) and relative permeability (how easily fluids flow through the pores where other fluids are also present).

Pore-scale modeling is a useful tool for simulating and understanding how hydrogen behaves in the tiny pore spaces of porous materials. These models help us see how hydrogen moves, spreads out, and interacts with the pore walls at a very small level. Another important aspect is studying the contact angles in the system of hydrogen, water, and porous material. These angles tell us about the way these substances interact at the interfaces between solids, liquids, and gases. By studying these processes and measuring contact angles, we can gain a better understanding of how hydrogen is stored and released, considering factors like pressure, temperature, the type of material, and how easily fluids flow through the pores. This knowledge will help us design better systems for storing hydrogen energy in porous materials on a larger scale.

The primary objectives of this thesis are as follows: To develop pore-scale models for simulating and understanding underground hydrogen storage in geological porous media. To investigate the contact angle between hydrogen, brine, and sandstone systems and their influence on storage and release mechanisms. To analyze the contact angle for a mixture of hydrogen-methane in the brine/sandstone system and assess its implications for hydrogen storage. To develop a dynamic pore network model to capture the dynamic behavior of hydrogen in geological porous media. To draw conclusions from

the findings and propose future research directions in the field of hydrogen energy storage.

This thesis is structured as follows:

Chapter 1 provides an introduction to the research topic, outlining its significance, motivation, objectives, and overall structure of thesis.

Chapter 2 of the thesis focuses on underground hydrogen storage (UHS) in porous rocks saturated with brine. It presents a pore-scale modeling study to understand the behavior of hydrogen at the reservoir scale. The study quantifies important functions like relative permeability and capillary pressure and assesses their dependence on fluid and rock properties. It also explores cyclic multiphase flow and investigates the sensitivity of hydrogen flow to micro-scale characteristics such as contact angle and rock structure. The research aims to provide insights into site selection and the safe operation of hydrogen energy storage systems.

Chapter 3 investigates the contact angle for the hydrogen/brine/sandstone system. It describes the experimental methods and materials used to measure the contact angle and presents the results and discussion on the effects of bubble size, pressure, temperature, salinity, and rock type on the contact angle.

Chapter 4 explores the contact angle for a mixture of hydrogen-methane in contact with the brine/sandstone system. It details the experimental apparatus and procedures employed for contact angle measurements and provides results and discussions on the influence of bubble size, gas composition, pressure, temperature, and salinity on the contact angle.

Chapter 5 introduces a dynamic pore network model for analyzing hydrogen energy storage in geological porous media. It presents the methodology employed in the model, the description of the pore space, displacement and transport properties, and two-phase flow modeling. The results and discussions from the dynamic pore network model are also included.

Chapter 6 concludes the thesis, summarizing the main findings, contributions, and implications of the research. It also proposes future research directions and areas for further exploration.

In summary, this thesis aims to contribute to the understanding of hydrogen energy storage in geological porous media through pore-scale modeling and contact angle analysis. The subsequent chapters will delve into the specific aspects of this research, providing in-depth analyses and findings that advance the field of hydrogen energy storage.

PREFACE

Dear reader,

I am excited to share the journey that led me to this moment - presenting my PhD dissertation at TU Delft. While I will not go into the details but will highlight the key moments that shaped my path.

My journey began in early 2020, just two months before the global pandemic took hold. In the face of these initial hurdles, I found good support from my supervisor, Prof. Hadi Hajibeygi, as well as my colleagues and friends at TU Delft. It was a trying time for everyone, but it also marked the beginning of an incredible and unforgettable adventure.

Hadi gave me the chance to share my knowledge in a master course that I developed during my master's thesis. I was thrilled to have this opportunity since it allowed me to delve into my favorite topic of micro-scale modeling. Meanwhile, I began learning and researching underground hydrogen storage, which turned out to be a promising solution to the world's challenge of global warming. I was excited to be part of one of the leading projects in this field. This endeavor also opened doors for me to collaborate with Prof. Martin Blunt and publish our first paper, which served as a comprehensive literature survey at the time. In the process, we addressed some critical gaps in information required for a better understanding of the unique characteristics of hydrogen systems. This provided me with the opportunity to work in the lab alongside Dr. Rouhi Farajzadeh and master's students. Despite the challenges posed by the pandemic, this period proved to be exceptional as it allowed me to learn from experiments, a vastly different experience from computer modeling. Learning from experiments felt like being taught by nature itself, while developing code or simulators resembled nurturing a child through teaching. Hadi also entrusted me with the responsibility of assisting in organizing the first online InterPore conference, an experience that was both special and transformative. It taught us how to adapt and work effectively in a completely remote environment.

As this project evolved, it eventually transformed into a PhD opportunity, thanks to Hadi's dedication. This brought the brilliant prospect of being supervised by Prof. Kees Vuik not only introduced me to the numerical analysis group at DIAM but also welcomed me into a supportive and friendly atmosphere. It was within this environment that I was able to integrate quickly, and it gave rise to numerous wonderful memories. Throughout our weekly meetings, Kees provided invaluable insights from his expertise and beyond academia, he also played a significant role in shaping my personality and provided guidance whenever I needed it.

I am grateful to Prof. Rainer Helmig for granting me the opportunity to spend a month in Stuttgart, familiarizing myself with their simulator and shaping our collabora-

tion for the final phase of my PhD work. Together with all the international conferences and collaborations, this journey helped me meet and connect with so many wonderful people in my field of work.

One of the highlights of my journey was an internship at TNO, which not only broadened my network but also exposed me to a different working environment. I enjoyed the company of welcoming colleagues and made lasting friendships there.

My story is one of resilience, growth, and the power of teamwork. I eagerly look forward to sharing more about my research and experiences in the pages that follow.

Yours Sincerely,

Leila Hashemi
Delft, October 2023

1

INTRODUCTION

"The beginning is the most important part of the work."

Plato

Addressing the urgent need for sustainable energy solutions, hydrogen has gained significant attention due to its high energy density and potential for carbon-free energy conversion. To enable the widespread use of hydrogen, efficient methods for storage and retrieval are essential. Hydrogen energy storage in geological porous rocks offers a promising approach to achieving this goal. This thesis aims to enhance our understanding of hydrogen storage in geological porous rocks by investigating pore-scale modeling and analyzing contact angles. By delving into these areas, the research aims to contribute to the development of efficient and reliable hydrogen energy storage systems.

1.1. OVERVIEW OF UNDERGROUND HYDROGEN STORAGE

Hydrogen energy storage in underground porous reservoirs plays a crucial role in addressing the challenges of sustainable and clean energy at the scale of 100s TWh. Porous formations, such as saline aquifers and depleted hydrocarbon reservoirs, offer significant storage capacities, making them suitable for large-scale hydrogen storage [1, 2, 3]. This is essential for balancing the variable renewable energy supply and meeting the energy demands of consumers. Moreover, underground hydrogen storage provides geographical independence and flexibility, allowing for efficient storage and retrieval of excess renewable energy, even in locations far from population centers [1]. To illustrate the storage capacity of hydrogen in different media, Figure 1.1 presents a cross-section comparison. It shows that to store 100 terawatt-hours (TW h) of hydrogen energy, a certain volume of various media is required. Notably, the storage volume of hydrogen equivalent to that of one depleted reservoir is approximately equal to 388 salt caverns [4].

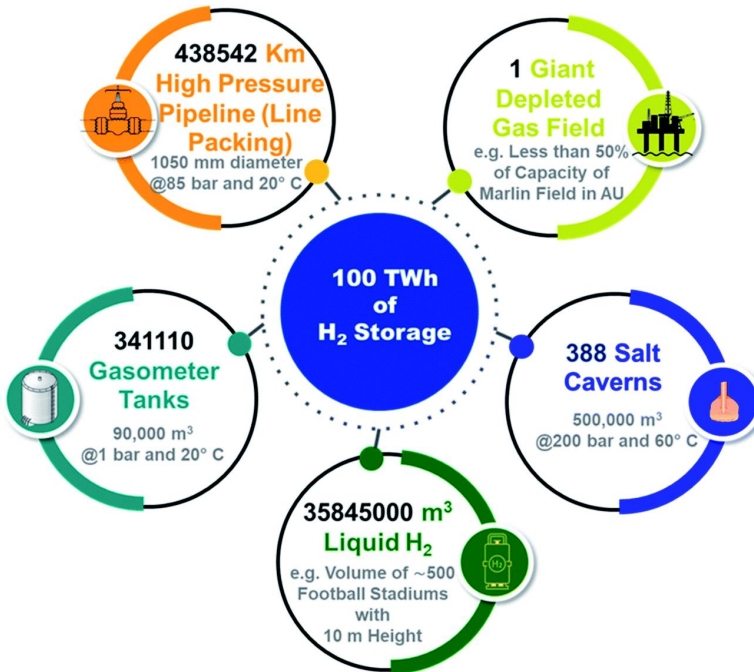


Figure 1.1: To store 100 terawatt-hours (TW h) of hydrogen energy, it would require a certain volume of various media. Specifically, the storage volume of hydrogen equivalent to that of one depleted reservoir is approximately equal to 388 salt caverns [4]. Source: Adapted from Emmanuel I. Epelle et al. (2022) under CC BY License.

The decarbonization of the heating and transport sectors is another important aspect of hydrogen storage in porous rocks. By decarbonizing these sectors through hydrogen utilization, greenhouse gas emissions can be reduced, contributing to a low-carbon economy and climate change mitigation goals [1, 5]. Additionally, the integration of hydrogen storage in porous rocks with existing infrastructure, such as natural gas pipelines

and storage facilities, offers a comprehensive and streamlined approach to energy storage [6, 7]. Several studies have been conducted to investigate subsurface porous rocks' hydrogen storage. A numerical model was used to simulate the operation of hydrogen storage in a hypothetical storage site based on an actual geological structure. The simulations showed that the storage could supply approximately 20% of the average electrical energy demand in the state of Schleswig-Holstein, Germany, for a week-long period [8]. Another study developed a scenario for subsurface porous rocks' hydrogen storage and simulated the operation using a numerical model. The results showed that the storage could store large amounts of energy over periods ranging from days to months to mitigate the fluctuating power generation from renewable sources [9].

However, there are still several scientific challenges associated with underground hydrogen storage (UHS) that must be addressed to ensure the safe and efficient large-scale commercial deployment of UHS. These challenges include understanding the geomechanical behavior of the reservoir, ensuring the compatibility of hydrogen with the subsurface environment, and managing the potential growth of hydrogen-consuming microbes [1].

In addition to the mentioned challenges, there are other concerns related to the cyclical nature of hydrogen storage operations. Pressure and stress changes within the reservoir can affect the integrity of the well, the reservoir, the caprock, and the entire subsurface storage complex [7]. This highlights the need for a thorough understanding of the reservoir's geomechanical behavior and the development of appropriate monitoring and mitigation strategies.

Another challenge is the safe storage of hydrogen. Ensuring the stability of hydrogen in the subsurface environment is crucial to prevent leaks, explosions, or other safety hazards [1]. This requires a thorough understanding of the chemical processes occurring within the reservoir and their potential impact on the operations of the storage system.

Hydrogen-consuming microbes in the reservoir can also affect the performance of the storage system. These microbes can consume hydrogen and produce byproducts that may cause corrosion, clogging of pore throats, or other issues [1]. Understanding the behavior and activity of these microbes in the storage environment is essential for developing strategies to mitigate their impact on hydrogen storage performance.

Moreover, the dynamic behavior of hydrogen once injected into the subsurface reservoir needs to be thoroughly studied [1]. Predicting how hydrogen will move through the reservoir and interact with the surrounding geological formations is critical for ensuring the efficiency and safety of the storage system.

Large-scale storage of hydrogen in porous rocks is still largely untested, and addressing these scientific challenges is essential for enabling its widespread adoption [1]. By conducting multidisciplinary research and addressing these knowledge gaps, it is possible to develop and deploy safe and efficient large-scale hydrogen storage systems that can support a net-zero carbon future.

To address these challenges, multidisciplinary research, including reservoir engineering, chemistry, geology, and microbiology, is required, which is more complex than that required for CH₄ or CO₂ storage [1, 5, 3]. By addressing these scientific obstacles, the vision of a global hydrogen economy and a sustainable future can be realized [1, 5]. To provide a visual representation of the different processes and phenomena involved in

UHS, Figure 1.2 presents a graphical illustration of various physical, geochemical, and microbial reactions associated with UHS [10].

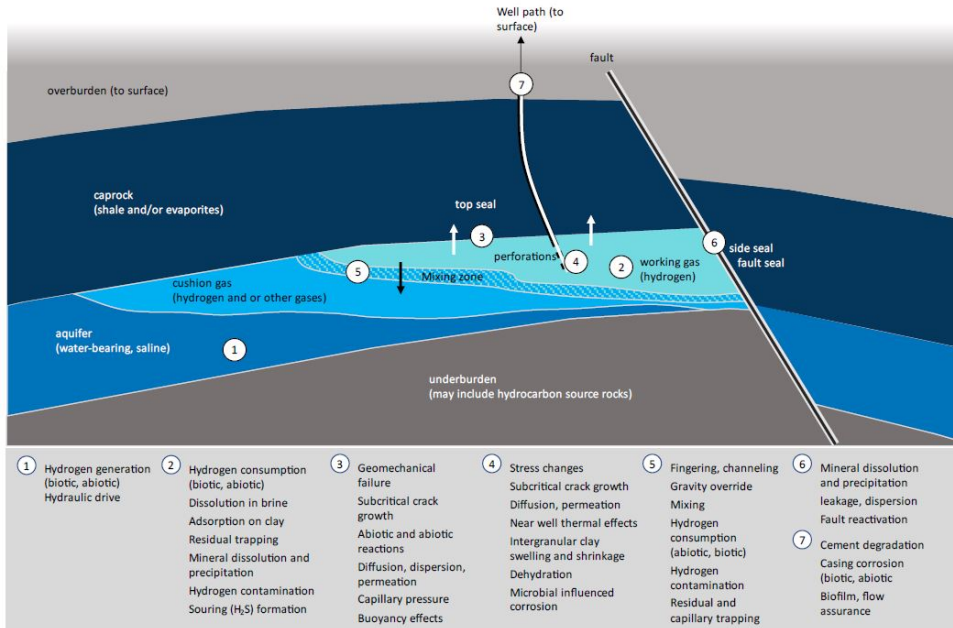


Figure 1.2: This illustration provides a visual representation of the different processes and phenomena involved in UHS, including but not limited to geological formations, chemical reactions, and microbial activity [10]. Source: Adapted from van Gessel and Hajibeygi et al., (2023), Hydrogen TCP-Task 42 Technology Monitor Report 2023.

Therefore apart from the economic, social, and legal factors discussed in H2STORE, HyUnder, ANGUS+, UndergroundSunStorage, Road2HyCOM, ADMIRE and US projects [10, 11, 12, 13, 14], several potential causes of hydrogen loss during storage and production operations, which directly impact the effectiveness of underground hydrogen storage (UHS), are outlined as follows:

- Leakage through cap rock or borehole

Characterizing geological formation to investigate the integration of cap rock is the key factor to selecting the proper site location for hydrogen storage and optimizing the rate and the pressure during injection and production cycles [13, 15]. For instance, in salt caverns as a rule of thumb, the range of gas operating pressure should be [24-80]% of overburden pressure. The upper bound avoids creating fractures and a lower value is suggested to preserve the injectivity of the reservoir [16]. Moreover, the mechanical stability of the salt cavern was addressed in ANGUS+ project [17]. In porous reservoirs, obtaining a proper production rate could be a vital operational parameter to avoid up-coning of the aquifer into the perforation

of well [18, 19]. Also, the other source of leakage of hydrogen can be through the borehole and well. That is one of the main subjects of HyINTEGRER project where integration of well in terms of corrosion reactions within casing and interaction of rock and cementation were investigated [20].

- Bio- and geo-chemical reactions

The injected hydrogen within the reservoir can undergo chemical reactions with the host rock and fluids, resulting in its consumption. These reactions can lead to changes in porosity and permeability through mineral dissolution or precipitation and the growth of biomasses [11, 12, 21]. Consequently, various UHS projects, such as H2STORE, ANGUS+, UndergroundSunStorage, and French projects, have examined these reactions and their effects [22, 12]. Most studies on geochemical interactions have shown limited activity, especially under moderate conditions [11, 23, 24, 25, 26, 27, 28]. However, in rocks containing pyrite, hydrogen-reductive activities can be significant, even at low temperatures, resulting in the undesired production of H₂S gas [21, 28]. Conversely, bio-reactions are considered the main factor contributing to hydrogen loss [11, 22, 29, 21, 25, 26, 27, 30, 31]. In the context of underground hydrogen storage, four common microbial reactions are methanogenesis, acetogenesis, sulfate reduction, and ferric reduction, which produce methane (CH₄), acetic acid (CH₃COOH), hydrogen sulfide (H₂S), and iron oxide (Fe₃O₄), respectively [11].

- Transport phenomena

The solubility and diffusion of injected gases into brine are inherent phenomena that occur during gas storage in geological formations. In the case of the H₂-brine system, these phenomena can result in hydrogen loss through cap rock and also affect the thermodynamic equilibrium, leading to increased pH and chemical reactions [11, 21]. Consequently, experimental and numerical studies have been conducted to quantify the dissolution of hydrogen into brine (listed in the appendix, Table A.3), which is dependent on pressure, temperature, and salinity [24, 32]. However, due to the very small diffusion coefficient (as shown in the appendix, Table A.3) and the solubility of hydrogen in brine, these findings indicate minimal losses through cap rock, estimated at approximately 1-3% per year in aquifers [12, 15, 33, 34], 0.16-3% in gas reservoirs [21], and 0.1% in gas reservoirs [26].

1.2. MOTIVATION & OBJECTIVES

Pore-scale modeling plays a crucial role in simulating and understanding the behavior of hydrogen within the intricate pore networks of porous rocks.

The importance of understanding hydrogen storage in porous rocks and its relevance to large-scale energy storage, geographical independence, and decarbonization has motivated the need for further investigation in this field. While experiments provide valuable insights, there are inherent limitations in characterizing the complex process of hydrogen transport in porous rocks. To overcome these limitations and enhance our understanding, pore-scale modeling serves as a powerful complementary approach [35].

Pore-scale modeling plays a crucial role in simulating and understanding the behavior of hydrogen within the intricate pore networks of porous rocks. By developing

accurate pore-scale models, we can capture the flow phenomena that occur at the microscopic level. These models provide valuable insights into the spatial distribution of hydrogen within the porous rocks, the interaction between hydrogen and the pore walls, and the factors affecting hydrogen storage and release.

To illustrate the concept of pore-scale modeling for underground hydrogen storage in porous rocks, Figure 1.3 presents an illustration. It showcases how the model captures the intricate pore network and provides insights into hydrogen transport and storage processes.

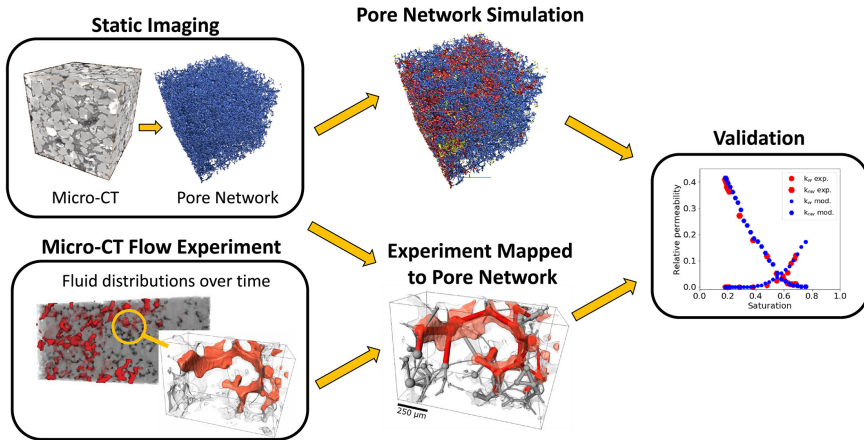


Figure 1.3: Illustration of the steps involved in the validation process, starting with the extraction of a pore network model from a micro-CT scan of the sample. Fluid distributions in the pore network model are generated using either numerical simulation or experimental micro-CT imaging. The simulation is then evaluated based on its ability to fill pores in approximately the right order compared to the experiment, particularly in predicting upscaled flow properties [36]. Source: Adapted from Tom Bultreys et al. (2020) under CC BY License.

The motivation behind conducting pore-scale modeling for underground hydrogen storage (UHS) in porous rocks lies in the need to understand hydrogen transport characteristics in the subsurface, which is essential for the appropriate selection of a feasible and safe storage site [35]. Pore-scale modeling allows researchers to quantify crucial reservoir-scale functions, such as relative permeability and capillary pressure, and their dependencies on fluid and reservoir rock conditions [35].

One of the key motivations for utilizing pore-scale modeling is the lack of robust experimental data available to properly characterize hydrogen transport in porous rocks. While experiments provide valuable information, they often face challenges in capturing complex pore-scale processes and measuring contact angles. Pore-scale modeling can fill this knowledge gap by providing insights into the flow of hydrogen in storage formations and quantifying the sensitivity to micro-scale characteristics such as contact angle and porous rock structure.

Moreover, pore-scale modeling serves as a complement to experiments by allowing rigorous sensitivity analysis. By varying fluid and rock properties, researchers can quantify the impacts of uncertainties on reservoir-scale functions, improving our understanding of the factors that influence hydrogen transport and storage. This, in turn, enables

more accurate predictions and facilitates informed storage site selection.

By integrating pore-scale modeling with experimental data, we can enhance our understanding of hydrogen storage in porous rocks. This comprehensive approach allows us to overcome the limitations of experiments alone and provides a deeper insight into the complex processes governing hydrogen transport and storage. Therefore, the objectives of this thesis encompass the development of pore-scale models, alongside experimental investigations, to comprehensively study underground hydrogen storage. Through this integrated approach, we aim to optimize storage site selection, improve safety, and enhance the efficiency of hydrogen storage systems, ultimately contributing to the advancement of sustainable and low-carbon energy solutions.

The objectives of this thesis are designed to address key aspects of underground hydrogen storage in porous rocks. Firstly, the aim is to develop pore-scale models that can accurately simulate and enhance our understanding of hydrogen storage in such systems. These models will enable us to investigate the transport and diffusion processes of hydrogen within the intricate pore networks of porous rocks.

Secondly, the objective is to analyze the contact angle between hydrogen, brine, and sandstone systems. By measuring and understanding this contact angle, we can gain insights into the wetting behavior and interfacial interactions that govern the storage and release mechanisms of hydrogen. Furthermore, the objective includes assessing the contact angle for a mixture of hydrogen-methane in the brine/sandstone system, which will provide valuable information about the behavior and potential synergistic effects of different gas components.

To capture the dynamic behavior of hydrogen in porous rocks, a dynamic pore network model will be developed as part of the objectives. This model will allow us to simulate the time-dependent processes and evaluate the impact of various factors, such as pressure, temperature, and flow rate, on hydrogen storage and release.

Lastly, the objectives include drawing conclusions from the research findings and proposing future research directions in the field of hydrogen energy storage. By accomplishing these objectives, this thesis aims to contribute to the advancement of knowledge and provide valuable insights into optimizing the design and operation of underground hydrogen storage systems in porous rocks.

2

PORE-SCALE MODELLING AND SENSITIVITY ANALYSES

"The only way to do great work is to love what you do."

Steve Jobs

Underground hydrogen storage (UHS) in porous rocks is a promising large-scale energy storage technology, due to hydrogen's high specific energy capacity and the high volumetric capacity of aquifers. Appropriate selection of a feasible and safe storage site vitally depends on understanding hydrogen transport characteristics in the subsurface. Unfortunately, there exist no robust experimental analyses in the literature to properly characterize this complex process. As such, in this work, we present a systematic pore-scale modelling study to quantify the crucial reservoir-scale functions of relative permeability and capillary pressure and their dependencies on fluid and reservoir rock conditions. To conduct a conclusive study, in the absence of sufficient experimental data, a rigorous sensitivity analysis has been performed to quantify the impacts of uncertain fluid and rock properties on these upscaled functions. The parameters are varied around a base-case, which is obtained through matching to the existing experimental study. Moreover, cyclic hysteretic multiphase flow is also studied, which is a relevant aspect for cyclic hydrogen-brine energy storage projects. The present study applies pore-scale analysis to predict the flow of hydrogen in storage formations, and to quantify the sensitivity to the micro-scale characteristics of contact angle (i.e., wettability) and porous rock structure.

Parts of this chapter have been published in Scientific Reports **11**, 8348 (2021) [35].

2.1. INTRODUCTION

Renewable energy sources such as wind and solar are intermittent in nature. Therefore, to develop a low-carbon-based energy mix in the future, large-scale storage technologies need to be developed. Hydrogen is an attractive energy storage option, since it has a high specific energy capacity of 120 MJ/kg, and its combustion products are clean. However, hydrogen has a low density of 0.09 kg/m³ at standard conditions. As such, large-scale volumes, much beyond the scope of surface-based facilities, are required to store energy in the scale of GWhr to TWhr [37]. Geological formations, such as aquifers, depleted hydrocarbon reservoirs, and salt caverns provide ample volumes for storing hydrogen at high pressure (thus high energy densities). These formations conveniently allow for large-scale (G-TWhr) storage of hydrogen gas [11, 18, 19, 23, 24, 38, 39, 22, 40, 41, 29, 20].

Among the potential sites for underground hydrogen storage (UHS), deep saline aquifers, which have been widely considered for CO₂ storage [42], provide significant gas storage capacities. Introducing hydrogen into the subsurface, however, can potentially drive many interactions with the existing fluid in the reservoir and the host rock. Note that experimental studies on sandstone rocks have reported low reactivities with the stored hydrogen in the absence of clay [11, 19].

The feasibility of UHS has become an attractive subject only in recent years, while the initial studies go back to the 1970s. In 1979, Foh et al. published their final techno-economic report for UHS [12, 43]. Later, as shown in Table 2.1, several UHS field and research projects have been established around the world. More information regarding these projects is provided in the appendix A.

Table 2.1: Worldwide underground hydrogen storage projects [11, 12]. More information is provided in the supplementary materials.

Type	Country	Location
Salt Cavern	The UK	Tesside
	The US	Moss Bluff
		Spindletop
		Clemens
	Germany	Bad Lauchsttdt Kiel
Aquifer	Germany	Ketzin
	France	Beynes
	Czech	Lobodice
	Russia	Kasomovskoie
Depleted Gas Reservoir	Argentina	Hychio

The economic, societal, and legal aspects of UHS have been addressed in several projects, including H2STORE, HyUnder, ANGUS+, UndergroundSunStorage, Road2HyCOM, and projects in the US [11, 12, 13]. These studies classify potential sources of hydrogen loss and reactivities in three major categories: (1) Leakage through cap rock and borehole, (2) bio- and geo-chemical reactions, and (3) diffusivity of hydrogen into the brine. All these important aspects are briefly revisited below.

Characterization of the sealing properties of the cap rock and borehole zone is essential for site selection and operational conditions [13, 15]. For instance, in salt caverns, as a rule of thumb, the range of gas operating pressure should be between 24% to 80% of the overburden pressure [16]. The upper bound is set to avoid creating fractures, while the lower one is determined based on maintaining the injectivity of the reservoir and avoiding cavern collapse [16]. In porous reservoirs, the appropriate production rate is a vital parameter to avoid coning of aquifer brine into the good perforation zone [18, 19]. Furthermore, as shown in HyINTEGRER, another source of hydrogen leakage can be through the well borehole and casing materials [20].

Bio-chemical and geo-chemical reactions also stand as key factors in the UHS studies. More specifically, stored hydrogen in the reservoir can be consumed by chemical reactions with the host rock and pre-existing fluids. Further consequences of these reactions are changes in porosity and permeability by dissolution or precipitation of minerals or growing biomass [11, 12, 21]. Therefore, in many UHS projects (i.e., H2STORE, ANGUS+, UndergroundSunStorage, projects in France) these reactions and their consequences were investigated in detail [22, 12]. Most of these studies report very limited geochemical interactions, especially at moderate conditions (reservoir pressure and temperature) [11, 23, 24, 25, 26, 27, 28]. However, for pyrite-bearing rocks, hydrogen-reductive activities might be considerable, even at low temperatures, which can produce highly-toxic H₂S gas [21, 28]. Furthermore, bio-reactions are known to be the main factor contributing to hydrogen loss [11, 22, 29, 21, 25, 26, 27, 30, 31]. Four common microbial reactions in the context of underground hydrogen storage are methanogenesis, acetogenesis, sulfate-reduction, and ferric-reduction that produce methane (CH₄), acetic acid (CH₃COOH), hydrogen sulfide (H₂S), and iron oxide (Fe₃O₄), respectively [11].

Finally, like many other gases, solubility and diffusion and fingering of injected hydrogen into the reservoir brine can be another source of hydrogen loss in geological formations. Even though cushion gas (e.g., N₂ or CO₂) is expected to prevent (at least most of) the stored hydrogen from reaching the brine, it is still important to quantify the transport properties of H₂-brine, so to appropriately design the system when H₂ and brine come to contact in the reservoir. The dissolved hydrogen in the brine also changes the thermodynamic equilibrium conditions, which can change the pH and increase the chemical reactivity [11, 21, 44]. Experimental and numerical studies have been conducted to quantify the dissolution of hydrogen into brine (listed in the supplementary materials). The dissolution is found to depend on pressure, temperature, and salinity [24]. Because the dissolution and diffusion coefficients (listed in the supplementary materials) are small, the solubility of hydrogen into the brine is reported to be minimal, i.e., about 1-3%/year in aquifers [12, 15, 33, 34, 32] and 0.1-3% in depleted gas reservoirs [21, 26].

In several studies such as H2STORE, ANGUS+, UndergroundSunStorage, HyUnder, American, and French projects, reservoir-scale simulations were performed to estimate the storage efficiency. Except for one experimental study at a specific condition for the storage projects in France [11], there exist no other experimental studies to characterize H₂-brine transport properties (i.e. capillary pressure and relative permeability). One group of studies has used literature data from natural gas (methane) reservoirs [18, 21]. Alternatively, another group of studies has used empirical functions such as van

Genuchten and Brooks & Corey for the hydrogen-brine system [19, 8]. It is therefore essential to critically analyze the pore-scale transport dynamics of the hydrogen-brine system, and report the range of relative permeability and capillary pressure suitable to simulate this complex process at the scale of the storage site, especially in the absence of robust experimental data. It is also important to investigate whether the use of classical hydrocarbon-based functions is justified, in the new context of hydrogen-brine systems.

This paper reports the first pore-scale-based effective functions to consistently describe hydrogen-brine transport at the reservoir scale. It also reports the sensitivity of the system with respect to uncertain parameters and indicates the key parameters to characterize the system accurately for a given storage scenario. This study also accounts for cyclic hysteretic physics, to appropriately analyze primary drainage (hydrogen injection), secondary imbibition (hydrogen withdrawal), and secondary drainage (hydrogen re-injection), which are all important and in some aspects unique (e.g. cyclic transport), for seasonal H_2 storage in aquifers.

The rest of the paper is organised as follows. Next, the pore-network methodology is briefly revisited, emphasising novel developments, specific to the H_2 -brine system, including hysteretic contact angles and relevant parameters obtained by processing the existing experiment in the literature. Then results are presented for a systematic study, in which cyclic transport is upscaled to find relative permeability and capillary pressure as a function of saturation. This section also elaborates on the ranges of H_2 -brine upscaled functions, their hysteretic behaviour through cyclic transport, and whether empirical functions in the literature are valid. Note that the supplementary materials provide complementary data sets that were left out of the main manuscript and a list of all UHS projects.

2.2. METHODS

Multiphase flow properties in subsurface reservoirs can be predicted by several methods including laboratory measurements and numerical simulations [45, 46, 47, 48, 49, 50]. Experimental approaches are costly and time-consuming and are found for limited samples and conditions [45]. Numerical modelling and simulations are therefore crucial to complement the laboratory studies to allow for a wider range of studies and sensitivity analyses.

In this study, the most computationally-efficient pore scale approach, which is called quasi-static pore network modelling “PNM”, was used to simulate the fluid flow of UHS at the pore-scale and to estimate the macro-scale properties, i.e., capillary pressure and relative permeability. Quasi-static PNM is an appropriate method for the capillary-dominated flow regime where the capillary number is less than 10^{-4} [51]. This is a common range for immiscible two-phase flow in many subsurface applications. All the simulations in this paper were implemented by using open-source software from Imperial College London, called “pnflow” [52], which is validated with experimental results for hydrocarbon reservoirs [51, 53].

Below, the key components of pore-network modelling are first presented. Then the specific developments relevant to H_2 -brine transport are discussed. Detailed information about the well-developed pore-network modelling approach can be found in the literature [45]. Here, for the sake of brevity, we focus on new developments relevant to

H₂-brine systems.

- Pore-Network Modelling (PNM) description

PNM uses a topologically and geometrically equivalent network of a rock sample to predict capillary pressure and relative permeability by simulating fluid flow through the elements of the network. Processing 3D micro-CT images of a core plug provides information about the network and its elements including radius, volume, length, coordination, clay volume, etc. [54, 55]. The elements with larger volumes represent “pores” and the elements which connect the pores are called “throats” [45, 56]. Figure 2.1 shows an illustration of a 3D image of a sandstone and its extracted pore network [51].

All the elements are uniform ducts with various cross-sectional shapes which are classified into circle, square, and triangle shape factors G , which is defined as A/P^2 , where A is the cross-sectional area and P is the perimeter length [45, 57]. Figure 2.1 presents an illustration of pore shapes. Most of the earliest network models assumed circular cross-sections for simplicity [58]. One major disadvantage of a circular shape is that it cannot accommodate more than one fluid in a stable configuration in a single pore. Therefore, it does not allow for any films or layers of additional phases to be formed during displacement. In contrast, it can be clearly seen from thin section images of rocks that real pore shapes are very irregular and have many corners. Experimental studies have shown that in pores with angular cross sections, the wetting phase can occupy the corners with the non-wetting phase in the centre. These corner-wetting layers provide additional phase connectivity and hence have an impact on trapping. Thus, networks that have pore elements with angular cross sections provide the opportunity to predict experiments where corner flow is crucially important.

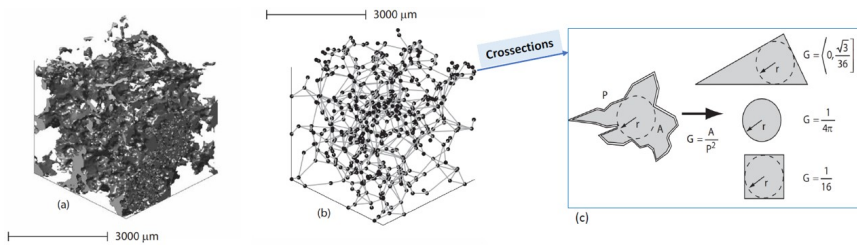


Figure 2.1: (a) 3D image of sandstone along with (b) a topologically equivalent network representation (c), and categorizing the cross-section of elements based on the shape factor (G) [51, 45].

In a quasi-static network model, the capillary pressure is the driving force that determines the saturation evolution in the model. This quantity is changed gradually and, for each capillary pressure value, the equilibrium position of the fluid-fluid interfaces is determined. The displacements or changes of fluid configurations occur sequentially, according to the entry capillary pressure criteria and the connectivity of each fluid to the inlet and outlet of the network. Since the network is

initially saturated with the wetting phase, the displacement process starts with primary drainage followed by secondary imbibition, and finally, secondary drainage to simulate cyclic injection and withdrawal. The details of the fluid-flow simulation procedure and governing equations have been explained in the literature [51].

2

- Fluid and rock parameters

In the available experimental report for the hydrogen-brine system, Yekta et al. [11, 59] used sandstone rocks from the Buntsandstein formation (Vosges level). Two core flooding tests were performed under conditions representative of shallow and deep aquifers. The properties of the rock and the fluids are given in Table 2.2.

Table 2.2: Reported fluid and rock properties for H₂-brine experimental primary drainage tests [11, 59].

Rock	Formation		Porosity (%)				Permeability (mD)	
	Vosges- sandstone		19.8				46	
Fluid	Depth	$\sigma_{\text{H}_2, \text{brine}}$ (mN/m)	μ (Pa.s) $\times 10^6$		ρ (kg/m ³)		$\cos(\theta_r)$	θ_r (degrees)
			H ₂	brine	H ₂	brine		
	Shallow (5 MPa, 20°C)	51	8.94	999	5.6	1000.5	0.93	21.56
Deep (10 MPa, 45°C)	46	9.54	597	7.2	994.5	0.82	34.9	

In this work, we define the base-case for the H₂-brine system as the one obtained based on the experiment described previously [11, 59]. Since the experimental data for hydrogen-brine is limited to only the primary drainage cycle (initial injection of H₂), to estimate advancing contact angles in all models, the Morrow relationship, as shown in Figure 2.2, was used. However, for receding angles more than approximately 12°, if one follows the Morrow curves, the corresponding advancing contact angle becomes bigger than 90°. This shows the rock becomes hydrogen-wet, which is very unlikely to be realistic. To resolve this challenge, in this study, the maximum advancing contact angle is, therefore, set to 85°, as shown in Figure 2.2. This modification guarantee that hydrogen is the non-wetting phase in all cases. Additionally, a uniform distribution of contact angle (a constant value in all pores) is employed for all the simulations in this paper.

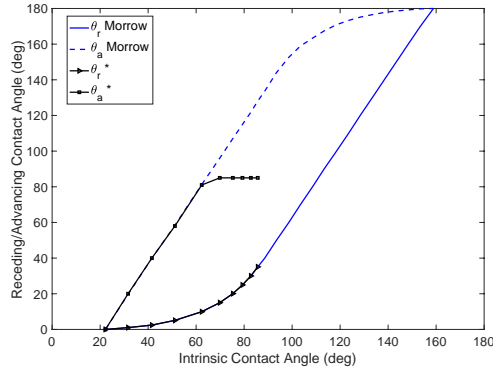


Figure 2.2: Relationship between receding θ_r and advancing θ_a contact angles as functions of intrinsic contact angle θ_i , based on the literature [60, 51]. * indicates the modified relationship, which is defined in this work, to maintain water-wet rock conditions at all times.

Also, as for the rock, relatively homogeneous Berea sandstone is considered, unless otherwise stated. The extracted network data is illustrated in Figure 2.3 [61].

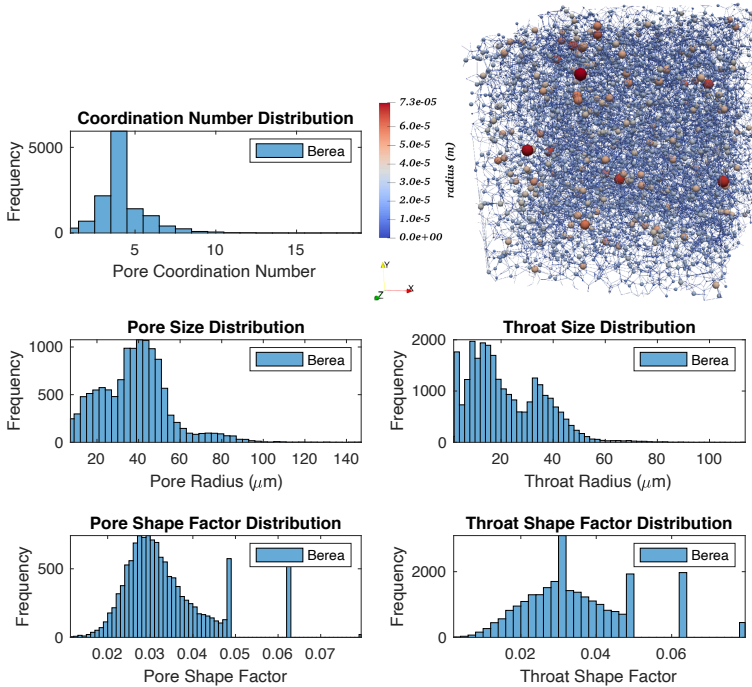


Figure 2.3: Illustration of the pore network model characteristics for Berea sandstone [61].

The base case scenario for our analyses is defined as follows. The base rock is consid-

ered to be the Berea sandstone with the characteristics presented above. The receding contact angle and the interfacial tension for H₂-brine in the base case are defined following the available experimental data at the core scale [11, 59]. The receding contact angle, assumed to be constant across the micro-scale sample, was found by fitting to the measured capillary pressure. As presented in the literature, this results in $\theta_r = 21.56^\circ$ and $\sigma = 51$ [mN/m], as shown in Table 2.2. Based on the modified-Morrow hysteresis curve, Figure 2.2, the advancing contact angle for the base case is set as $\theta_a = 85^\circ$. Using these data sets, the relative permeability and capillary pressure for the base case are presented in Figure 2.4. Note that the base case properties correspond to the Shallow formation reported in Table 2.2. Moreover, the results corresponding to the fluid properties of the Deep formation are also presented in Figure 2.4. Consistent with the reported experiments, our pore-network model results also confirm insensitivity towards different pressure and temperature values of Shallow and Deep formations. This is because we only have a small change in interfacial tension, which affects the capillary pressure, and no change in advancing contact angle, leading to identical relative permeabilities in the two cases.

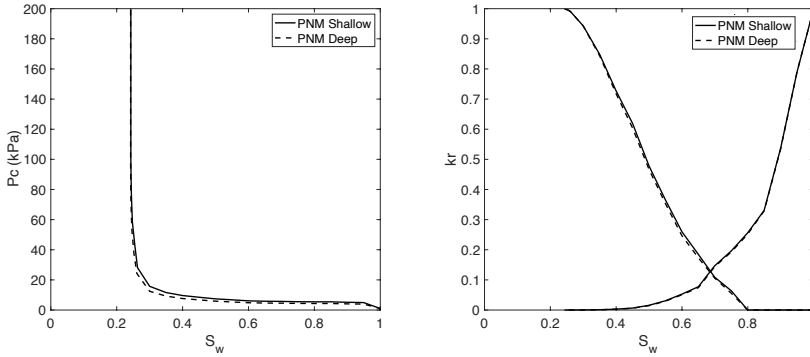


Figure 2.4: Capillary pressure (left) and relative permeabilities (right) for the base case, i.e., for Berea sandstone using the experimentally-relevant fluid properties of $\theta_a = 85^\circ$, $\theta_r = 21.56^\circ$ and $\sigma = 51$ [mN/m]. The base case corresponds to the Shallow formation of Table 2.2. Also shown are the results corresponding to the fluid properties of the Deep formation.

What comes next is a systematic analysis and quantification of uncertainty for cyclic transport within the parameter range of the available experimental data [11, 59]. In addition, we investigate whether empirical Corey functions [8] are acceptable for upscaling hydrogen-brine transport. Rock and fluid parameters are listed in Table 2.3. Note that to differentiate the effect of different rock parameters such as clay volume and coordination number (i.e., the number of throats connected to a pore), statistical models were generated [61].

2.3. RESULTS

Hydrogen-brine transport for energy storage applications is unique in some aspects. Firstly, the upscaled transport functions need to be benchmarked against empirical func-

Table 2.3: Parameters used in the simulations.

	Category	Parameter	Range
Fluid properties	Wettability	1. contact angle	$\theta_r \in [5 - 30]^\circ, \theta_a \in [58 - 85]^\circ$
Rock properties	Extracted Network	2. structure of sandstones	Table 2.5
		3. structure of carbonates	
	Generated Network Statistics	4. clay volume	[0-30]%
		5. averaged coordination number	[3-6]

tions employed in the literature for other gas-brine systems, especially Corey functions. Our first test case addresses this important aspect. Then, the cyclic nature of the storage application requires the simulation of cycles of injection and production. This leads to adding the secondary drainage into the pore-network modelling framework. The second test case deals with this important aspect and quantifies the hysteretic nature of the upscaled functions around the base case scenario. Lastly, uncertainty in the fluid and rock properties needs to be investigated, to find their impact on the upscaled multiphase flow functions. The last two test cases address the uncertainty in the fluid and rock properties, respectively. With these studies, we aim to highlight the key aspects of hydrogen-brine transport for energy storage. A summary of the test cases is given in the list below.

Test Case 1: Benchmarking pore-network upscaled functions with those obtained with the widely-used Corey equation.

Test Case 2: Hysteretic upscaled transport functions for cyclic transport

Test Case 3: Impact of fluid properties on the hysteretic upscaled functions

Test Case 4: Impact of rock properties on the hysteretic upscaled functions

2.3.1. TEST CASE 1: BENCHMARKING PORE-NETWORK MODELLING (PNM) AND COREY FUNCTIONS

Figure 2.5 shows the relative permeabilities for hydrogen injection into brine-saturated rock. Since in the literature no hysteresis effects were considered [8], the PNM results are also plotted only for primary drainage. The best fit to the PNM results, constrained with Corey equation parameters [62], resulted in different values for the exponents of hydrogen and brine, 1.31 and 4.36 respectively. However, in the literature, the constant exponent of 2.5 for both hydrogen and brine has been used [8]. As such, the PNM-based studies indicate that different exponents for hydrogen and brine need to be considered. This makes physical sense since the exponents are related to pore structure and wettability and are higher for the wetting (brine) phase as it fills the smaller pores, as opposed to lower exponents (higher relative permeabilities) for the non-wetting phase (hydrogen) that preferentially occupies the larger regions of the pore space.

2.3.2. TEST CASE 2: HYSTERETIC UPSCALED TRANSPORT FUNCTIONS FOR CYCLIC TRANSPORT

In real-field hydrogen storage projects, there are repeated cycles of injection and withdrawal. As such, both primary and secondary drainage processes will occur in addition

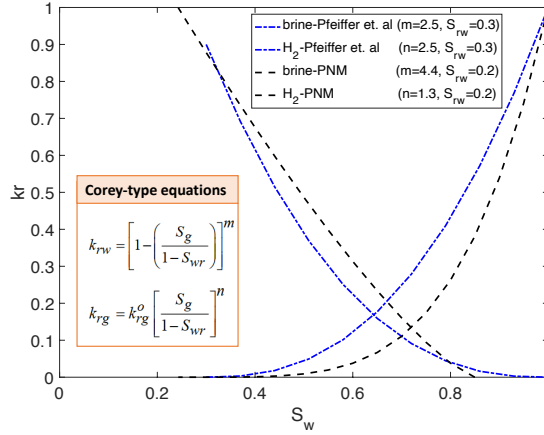


Figure 2.5: Benchmarking H_2 -brine relative permeability values for primary drainage between PNM and Corey functions with exponents that were used in the literature [8].

to secondary imbibition. To investigate this, Figure 2.6 shows the impact of cyclic injection and withdrawal of hydrogen on capillary pressure and relative permeability. Note that, as discussed in the Methods Section, the modified Morrow values for advancing and receding contact angles have been used. Compared with primary drainage, secondary drainage shows lower relative permeability values at the same saturation. This is due to the disconnection of the hydrogen phase after secondary imbibition, as well as the presence of a trapped wetting-phase (brine) in some pores. Also, the remaining hydrogen phase, after secondary imbibition, leads to a decrease in capillary pressure values for the secondary drainage stage. Additional cycles of injection and production of hydrogen into the network of Berea sandstone are also investigated and provided in the supplementary material. Our observations indicate that the hysteresis effect stays the same for subsequent drainage and imbibition displacement, after the first injection-production cycle.

2.3.3. TEST CASE 3: IMPACT OF FLUID PROPERTIES ON THE HYSTERETIC UPSCALED FUNCTIONS

Among the fluid properties, wettability is found to have major impacts on the upscaled functions. The findings are discussed in two separate parts as follows.

1. Effect of wettability

The range of simulated contact angles for H_2 -brine is given in Table 2.4. Simulation results are shown in Figure 2.7. Note that increasing contact angles (which are less than 90°) changed the wettability of system and made it less water-wet. Since the receding contact angles varied between 5° to 30° , there is no significant effect on the results for primary drainage. However, during secondary imbibition and secondary drainage, increasing contact angles resulted in a smaller amount of trapped hydrogen (lower capillary pressure). Also, the maximum relative perme-

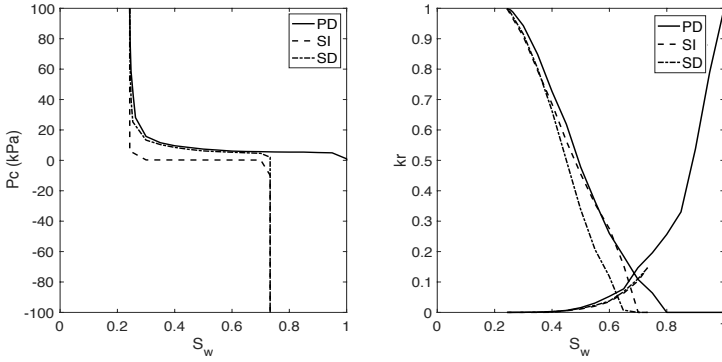


Figure 2.6: The impact of cyclic transport on capillary pressure and relative permeabilities for primary drainage (PD), secondary imbibition (SI), and secondary drainage (SD).

ability of the brine phase is shown for the strongly water-wet system with $\theta_i = 51^\circ$. Relative permeabilities of hydrogen during secondary drainage are mostly similar. However, during secondary imbibition, increasing contact angles towards neutral wettability (i.e., when intrinsic contact angles are close to 90°) increases the relative permeability of hydrogen. This is due to the reduced amount of trapped hydrogen.

Table 2.4: Fluid and rock properties used for the wettability sensitivity analysis, by changing advancing (θ_a) and receding (θ_r) contact angles. * indicates the base-case from the literature [11].

Rock	Formation		Dimensions (mm ³)	No. of pores	No. of throats	Porosity (%)	Permeability (mD)
		(big) Berea sandstone		$3 \times 3 \times 3$	12349	26146	18.33
Fluid	Test No.	$\sigma_{H_2,brine}$ (mN/m)	θ_r (degrees)	θ_a (degrees)	θ_i (degrees)	Viscosity ratio	Density difference (kg/m ³)
	1	51	5	58	51	111.745	994.9
	2	51	10	81	62	111.745	994.9
	3 *	51	21.56	85	75	111.745	994.9
	4	51	30	85	83	111.745	994.9

2. Effect of the difference between advancing and receding contact angles, i.e., $\Delta\theta = \theta_a - \theta_r$, with $\theta_r = 21.56^\circ$

In this set of tests, all the parameters of the base-case remained constant except the advancing contact angle. Figure 2.8 shows the impact of the difference between receding and advancing contact angles on capillary pressure and relative permeabilities. The maximum trapped hydrogen was observed for the case with equal advancing and receding contact angles. For the higher advancing contact angles, rock becomes less water-wet. Therefore, the relative permeability of hydrogen increases. There is also less trapping of hydrogen.

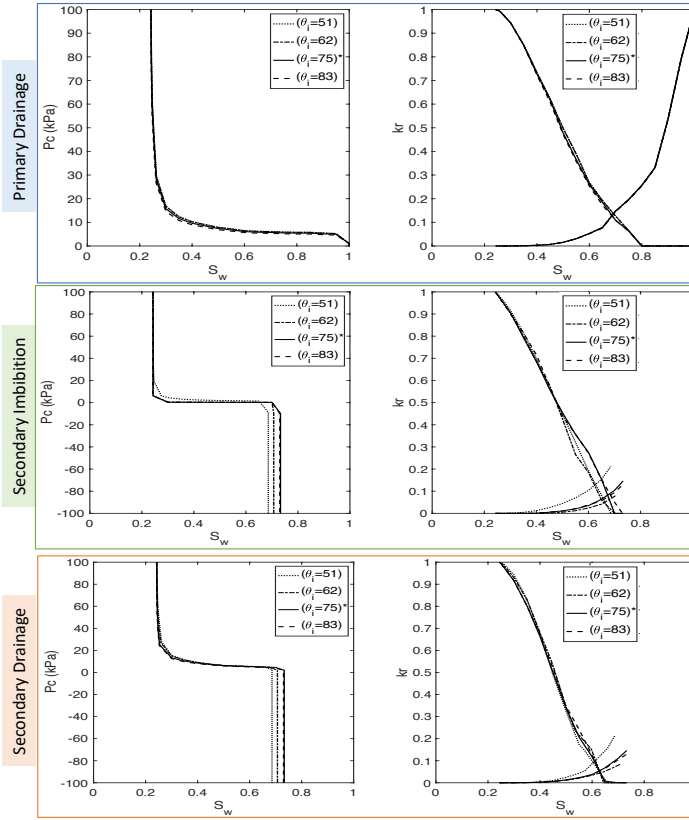


Figure 2.7: Sensitivity analysis for the H_2 -brine system for primary drainage, secondary imbibition, and secondary drainage due to changing receding and advancing contact angles. θ_i indicates the intrinsic contact angle, and * indicates the base-case which corresponds to the experimental data reported in the literature [11], i.e., $\theta_r = 21.56^\circ$ and $\theta_i = 75^\circ$.

2.3.4. TEST CASE 4: IMPACT OF ROCK PROPERTIES ON THE HYSTERETIC UP-SCALED FUNCTIONS

Rock structure has an important role in the transport behavior of fluids. To study changes in the saturation-dependent functions for various rock types, five extracted pore network models from images of sandstones and carbonates were used [61]. The properties of these samples and the system of the fluids (H_2 -brine) are given in Table 2.5. Moreover, detailed rock structures for all samples are provided in the supplementary materials. The outcome of the simulations is shown in Figure 2.9. Among the three sandstone models, small Berea and A1 showed almost zero water saturation trapped after injecting hydrogen which implies that they contain no clay. Similar patterns are observed for flow properties during primary drainage. Sample A1 which had the highest porosity and absolute permeability had the smallest residual hydrogen saturation and, as expected the highest values for the relative permeability of brine in secondary imbibition. A comparison of the two models from carbonate reservoirs indicates the impact of a complex pore

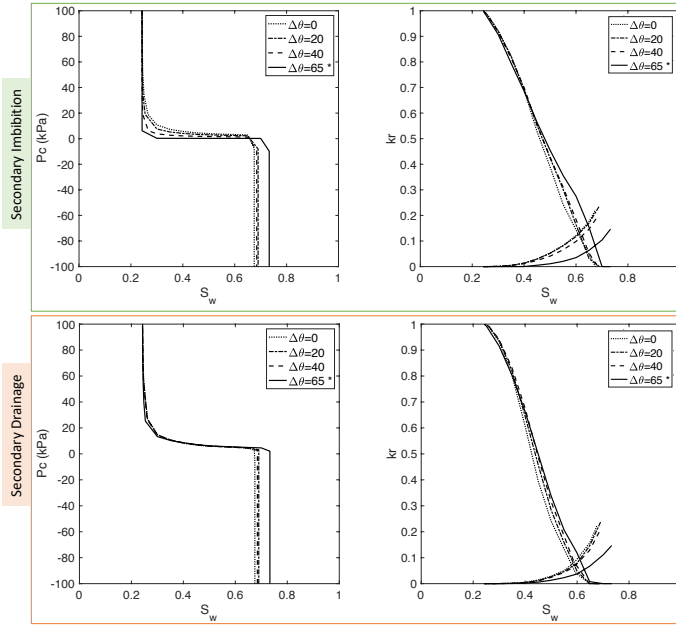


Figure 2.8: Effect of advancing contact angle on flow properties of H₂-brine for secondary imbibition. Note that the receding contact angle is fixed at 21.56°. * indicates the base-case which corresponds to the modified Morrow relationship as shown in Figure 2.2.

structure. Sample C2 has the smallest pores and restricted connectivity with therefore the highest capillary pressures during all displacement cycles and the highest residual (trapped) hydrogen saturation after secondary imbibition.

Table 2.5: Fluid and rock properties for studying the effect of rock structure on the upscaled transport functions.* indicates the base-case simulations.

Rock	Type	Model Name	Dimensions (mm ³)	No. of pores	No. of throats	Porosity (%)	Permeability (mD)	Ave. coord. number
	Sandstone	Berea *	3.000 × 3.000 × 3.000	12349	26146	18.33	2551.6	4.19
Berea (small)		2.138 × 2.138 × 2.138	6298	12545	19.60	1111.0	3.91	
A1		1.155 × 1.155 × 1.155	3393	11479	42.85	8125.5	6.65	
C1		1.140 × 1.140 × 1.140	4576	6921	24.67	1164.8	2.98	
Carbonate	C2	2.138 × 2.138 × 2.138	8508	10336	15.84	161.61	2.37	
	Fluid	Phases	$\sigma_{H_2,brine}$ (mN/m)	θ_r (degrees)	θ_a (degrees)	Viscosity ratio	Density difference (kg/m ³)	
	H ₂ -brine	51	21.56	85	111.745	994.9		

We define the maximum trapped hydrogen saturation as the one found after production corresponding to a capillary pressure $P_c = -100$ kPa. Figure 2.10 shows that many injection-production cycles do not change the maximum amount of produced hydrogen significantly. However, the maximum trapped hydrogen is affected by the rock structure. Characterization of these models (as provided fully in the supplementary material) indicates that lower connectivities and the smaller pores in model C2 are indeed the reason behind its highest residual hydrogen saturation, among all samples. On the other hand,

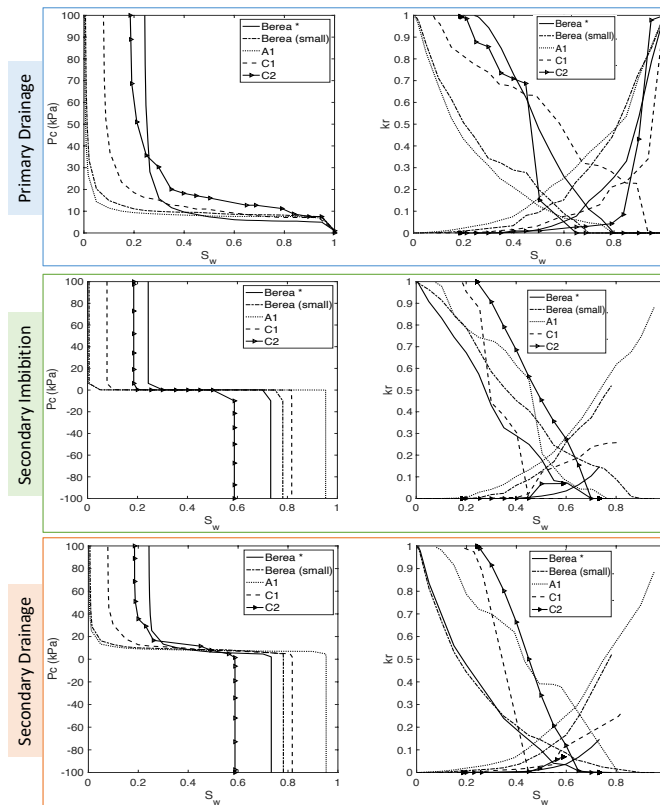


Figure 2.9: Sensitivity analysis of H₂-brine system for different rock types. * indicates the network that was used for the base-case of simulations.

model A1 with the maximum average coordination number and high permeability allows for the highest hydrogen production (i.e., minimum residual hydrogen saturation). In addition, the two models of Berea sandstone, with similar characteristics but different sample sizes, have almost equal storage efficiency.

To differentiate the effect of different rock parameters such as clay volume and coordination number, some statistical models were generated using an open source software [61]. The percentage of clay volume in the network directly changes the trapped water saturation after primary drainage, but the patterns of capillary pressures and relative permeability remain similar. Increasing the coordination number reduces capillary entry pressures and trapped hydrogen saturation during secondary imbibition. Moreover, its effect on relative permeabilities becomes significant during the displacement of hydrogen by water: a higher coordination number facilitates flow and suppresses trapping. Full details are presented in the supplementary material.

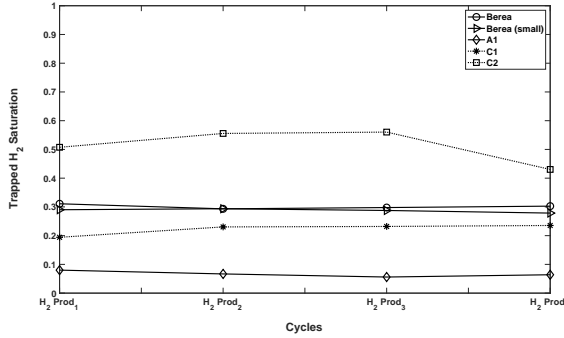


Figure 2.10: Sensitivity analysis of saturation of trapped hydrogen after 4 cycles of production for different rock types with advancing ($\theta_a = 81^\circ$) and receding ($\theta_r = 10^\circ$) contact angles and fluid properties of the base-case.

CONCLUSIONS

H₂-brine transport properties are quantified at the continuum scale through capillary pressure and relative permeability. These functions were predicted based on pore network modelling (PNM) which simulates the pore-scale displacement of fluids. Through several systematic studies, we first benchmarked the PNM fluid parameters with existing experimental data. This allowed us to define a meaningful base case configuration. The brine remains in the wetting phase. When the relative permeabilities are fit to a power-law type empirical model, the exponents are higher than for the non-wetting, hydrogen, phase. This is due to the fact that brine tends to occupy the smaller regions of the pore space. In addition, cyclic hydrogen storage in subsurface geological formations imposes hysteretic behavior. This effect, which needs to be considered for accurate transport simulations at reservoir scales, was studied for both capillary pressure and relative permeability. Systematic sensitivity analyses demonstrated that both capillary pressure and relative permeability are sensitive to contact angles as a representation of wettability. The pore structure also is another key determinant of multiphase flow properties. More precisely, using different image-based models of sandstones and carbonates resulted in very different relative permeabilities and capillary pressures for hydrogen-brine multiphase transport. This sensitivity analysis was further enriched by detailed characteristics of the studied rock samples. Also, various clay percentages affected the end-point values for drainage and imbibition cycles. Coordination number which quantifies the network connectivity also had a significant effect on the residual saturation of the non-wetting phase (hydrogen) after secondary imbibition.

The present study reports the baseline for further research on the characterization of H₂ transport properties while highlighting the need for further investigations in a laboratory environment.

The modelling data and upscaled functions are all made available open access at https://gitlab.tudelft.nl/ADMIRE_Public/PoreScale_H2 repository.

3

CONTACT ANGLE FOR HYDROGEN/BRINE/SANDSTONE SYSTEM

"Success is not final, failure is not fatal: It is the courage to continue that counts. "

Winston Churchill

Subsurface porous formations provide large capacities for underground hydrogen storage (UHS). Successful utilization of these porous reservoirs for UHS depends on accurate quantification of the hydrogen transport characteristics at the continuum (macro) scale, specially in contact with other reservoir fluids. Relative-permeability and capillary-pressure curves are among the macro-scale transport characteristics which play crucial roles in the quantification of the storage capacity and efficiency. For a given rock sample, these functions can be determined if pore-scale (micro-scale) surface properties, specially contact angles, are known. For hydrogen/brine/rock systems, these properties are yet to a large extent unknown. In this study, we characterize the contact angles of hydrogen in contact with brine and Bentheimer and Berea sandstones at various pressures, temperatures, and brine salinity using the captive-bubble method. The experiments were conducted close to the in-situ conditions, which resulted in water-wet intrinsic contact angles, of about 25 to 45 degrees. Moreover, no meaningful correlation was found with changing tested parameters. We monitor the bubbles over time and report the average contact angles with their minimum and maximum variations. Given rock pore structures, using the contact angles reported in this study, one can define relative-permeability and capillary-pressure functions for reservoir-scale simulations and storage optimization.

Parts of this chapter have been published in *Advances in Water Resources* **154**, 103964(2021) [63].

3.1. INTRODUCTION

A successful transition towards low-carbon energy systems depends not only on harvesting more renewable resources but also on advancements in large-scale (TWh) storage technologies. Renewable energy can be stored in TWh scales if it is converted into green molecules such as hydrogen. The green hydrogen can then be stored in underground geological formations, e.g., in depleted hydrocarbon reservoirs and saline aquifers [39, 41, 20].

Several research studies and a few pilot tests related to underground hydrogen storage (UHS) in porous reservoirs have been recently initiated [15, 29, 12, 13, 11]. UHS in porous formations still remains a challenge, due to the lack of characterization data needed as input parameters to perform reservoir simulation and robust storage optimization. Among these input parameters, hydrogen surface properties in contact with reservoir fluids, especially brine, are crucially important [1].

To date, there exist only two experiments for characterizing hydrogen contact angle in subsurface systems. First, a coreflooding test was performed in which hydrogen was injected in brine-saturated Vosges sandstone rock at two different pressure (P) and temperature (T) values of (50 bar, 20 °C) and (100 bar, 45 °C) [59]. It resulted in receding contact angles of 21.56° and 34.9°, respectively, for the first and second (P, T) values [59]. More recently, another study was performed in which receding and advancing contact angles were measured using the tilted plate experimental technique [64]. The study was performed at a pressure range of 0.1-25 MPa and a temperature range of 296-343 K. Both pure and aged quartz samples were used with stearic acid in contact with brine (10 wt% NaCl). The study reported that the increase of pressure or temperature resulted in increasing contact angles from 0° to a maximum of around 50° for pure quartz. However, when the quartz samples were aged for several months with stearic acid, intermediate wetting conditions were observed [64].

Despite its crucial impact in successful development of UHS technology, to date, there exists no hydrogen-specific dataset in general, nor contact angle measurements across scales, to allow for reliable site selection, development, and storage optimization [38, 44, 18, 15, 19, 23, 40, 29]. Specially once the contact angles are known, for a given rock type, one can perform pore-scale modelling to find upscaled relative-permeability and capillary-pressure curves [35, 65, 66, 67]. These functions will be used as input parameters for reservoir scale simulation studies [45, 68, 69]. Note that contact angles in cyclic storage transport is hysteretic [60, 70].

To resolve this knowledge gap, in this work, we perform contact angle measurements for hydrogen/brine/sandstone rock using a captive-bubble cell device. Since there are no external viscous forces to displace fluid and gas phases, our study allows for nearly static (intrinsic) contact angle measurements for hydrogen when it comes in contact with the saturated porous reservoir rock. We first benchmark our measurements for nitrogen gas with the published literature and then introduce hydrogen gas in the system. Table B.1, in the appendix, provides a summary of different contact angle measurement methods in the systems of gas/brine/solid surface. The study is performed under different pressures, temperatures, and salinity of the brine; so to represent a fair assessment of the in situ conditions. Our findings shed new light on the characteristics of the hydrogen surface characteristics when it is stored in the subsurface reservoirs.

The structure of this chapter is as follows. First, the experimental setup and procedure to measure the contact angle will be described in detail. Then the image processing methodology to measure the contact angles from the captured images is presented. In its following section, results and their relevance for UHS will be discussed. Finally, concluding remarks are presented.

3.2. METHODS AND MATERIALS

In this study, the captive-bubble method was utilized to measure intrinsic contact angles using a gas bubble at a solid-liquid interface. This method is advantageous over the alternative sessile drop method, because spreading and diffusion of the brine into porous hydrophilic substrates in the latter method poses experimental challenges, making the data less reliable [71].

3.2.1. MATERIALS

Hydrogen with a purity of 99.99 mol%, produced by Lindegas, was used. The rock slabs were taken from sawed homogeneous Bentheimer and Berea sandstone blocks. The properties of Bentheimer and Berea have been studied in literature [72, 73, 74]. The samples were mainly composed of quartz (95%) which was evenly distributed throughout the rock matrix (see appendix Figures B.2, B.1). The average porosity of the Bentheimer and Berea sandstones was about 20%, and permeability was around 2 to 3, and 0.1 Darcy, respectively. Each slab had dimensions of $30 \times 6 \times 12$ mm. In addition to brine containing NaCl, a synthetic seawater [75] with the composition in Table 3.1 was also used in the experiments.

Table 3.1: Synthetic seawater composition.

Salt	Quantity (ppm)
NaCl	24,500
KCl	670
MgCl ₂ .6H ₂ O	10,150
CaCl ₂ .2H ₂ O	1,450

3.2.2. MICROSCOPIC IMAGE ANALYSIS OF ROCK SAMPLES

To quantify the surface roughness of rock slabs, 2D and 3D microscopic images were taken using a LEICA 3D stereo explorer 3.1. The surface profiles were characterized based on the internationally-recognized standard of EN ISO 287, where the so-called P_a factor defines the surface roughness [76]. P_a is the arithmetic mean of the absolute ordinate height values $Z(x)$ within a sampling length (l_p). The average roughnesses of the Bentheimer and Berea slabs have been measured 0.030 and 0.025 mm, respectively.

3.2.3. EXPERIMENTAL SETUP

The captive-bubble setup, modified after Kaveh et. al. [76], was used to measure contact angles in the system of hydrogen/brine/rock at high pressures and temperatures. The schematic of the experimental setup is given in Figure 3.2. The setup comprises a single steel cell, which holds the rock sample and brine. The injection of the brine and other

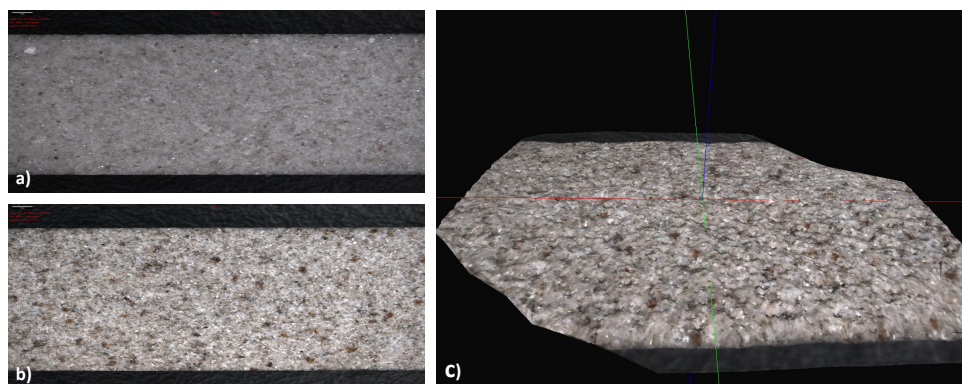


Figure 3.1: Microscopic surface images: a) 2D-Bentheimer, b) 2D-Berea, and c) 3D-Berea.

fluids takes place from the bottom and different inlets. Extraction of the brine and gas from the cell was done from the top. The pressure in the cell was held constant by a back-pressure regulator connected to a large nitrogen cylinder. Injection of both brine and hydrogen was done with the use of two Vindum pumps. To bring the brine and hydrogen to equilibrium, a pressure gauge was installed in between the hydrogen pump and the cell. Hydrogen flows through a line with respective inner and outer diameters of 0.25 mm and 1.58 mm to a nozzle from which the hydrogen is released into the brine. The bubble that was created on the rock surface was photographed with a Canon 90 camera (with a maximum resolution of 12.3 MP) attached to an endoscope. The pressure and temperature of the setup were monitored continuously and recorded in a computer connected to the system.

3.2.4. EXPERIMENTAL PROCEDURE

To start the experiment the cell, including the rock sample, was initially filled with the brine overnight to reach equilibrium. Then, at the desired pressure and temperature, a hydrogen bubble was injected through a needle at the bottom of the cell. Due to buoyancy, the bubble arises and sticks underneath the rock sample. The pictures of the released bubbles were taken by using the connected digital camera through the endoscope at one side of the cell and diffusion of the light source at the other side. To get sharp pictures of the bubbles, the resolution of imaging was set to 6.9 MP (3216 × 2136). Due to the diffusion and dissolution of hydrogen into brine, the size of the bubbles changed over time. Consequently, several images were taken after the injection of one bubble at each pressure and temperature. Therefore, for each experimental condition, the minimum and the maximum contact angles were reported in addition to the averaged values.

3.2.5. IMAGE ANALYSIS

To calculate the contact angles, the captured images from the hydrogen bubbles were analyzed using an in-house MATLAB code. The needle diameter inside the cell was used to define the scale of the images. Afterward, the image was converted to grey-scale format

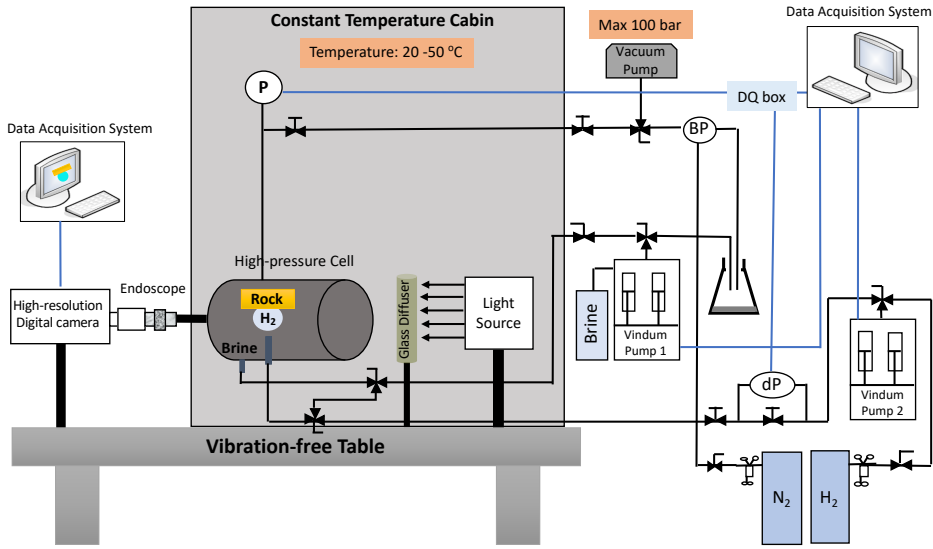


Figure 3.2: Schematic of the captive-bubble cell experimental setup.

and was cropped to only keep the bubble and the rock surface. To find the boundary of the bubble, the image was subsequently binarized. Tracing the boundary of the bubble and detecting the apex as well as contact points were followed by fitting the best curve based on the Axisymmetric Drop Shape Analysis-Profile (ADSA-P) technique [77]. All the main steps of the image analysis are shown in Figure 3.4. The ADSA-P technique fits the best theoretical Laplacian curve on the physically observed bubble interface [77]. The Young-Laplace capillarity equation for two fluid phases is given as

$$\Delta P = \sigma \left(\frac{1}{R_1} + \frac{1}{R_2} \right), \quad (3.1)$$

where σ is interfacial tension, R_1 and R_2 are the two principle radii of the curvature. Because of the axisymmetry of the bubble, the radii are considered equal at the apex ($R_1 = R_2 = R_0$), i.e.,

$$\Delta P_{apex} = \frac{2\sigma}{R_0}. \quad (3.2)$$

Also, by considering gravity as the only external force across the interface, pressure difference was assumed to be a linear function of the hydrostatic pressure ($\Delta\rho gz$) with interception of ΔP_0 at a reference plane, i.e.,

$$\Delta P = \Delta P_0 + \Delta\rho gz. \quad (3.3)$$

As shown in Figure 3.3, the origin of the coordinate system was placed at the apex point. The x-axis is tangent to the origin and normal to the axis of symmetry. Therefore, equation 3.3 can be rewritten as

$$\sigma \left(\frac{1}{R_1} + \frac{\sin(\theta)}{x} \right) = \frac{2\sigma}{R_0} + \Delta\rho g z, \quad (3.4)$$

where R_1 rotates in the plane of x-z and $R_2 = x/\sin(\theta)$ rotates in the plane of z-y. Equation 3.4 is restated as

$$\frac{dx}{ds} = \cos\theta \quad (3.5)$$

$$\frac{dz}{ds} = \sin\theta \quad (3.6)$$

$$\frac{d\theta}{ds} = \frac{2}{R_0} + \frac{\Delta\rho g z}{\sigma} - \frac{\sin\theta}{x} \quad (3.7)$$

which is a set of first-order differential equations in terms of the arc length (s). The initial conditions are applied at the apex of the bubble, positioned along the bubble's surface (arc length, $s_0 = 0$). The initial values of the dependent variables are as follows, $Z_0 = 0$ (Vertical coordinate), $X_0 = 1$ (Horizontal coordinate), $\theta_0 = 0$ (Angle). Finally, the above three differential equations were integrated using the Runge-Kutta numerical approach to find a theoretical Laplacian curve. To find the corresponding contact angle, the objective function is defined to minimize the deviation of the physically-observed curve from a theoretical curve by adjusting parameters: radius of the curvature at the apex, R_0 and interfacial tension, σ . The detail of this procedure has been extensively explained in the literature [77]. Brine and gas density were calculated based on the literature thermodynamic formulation for each specific pressure and temperature condition [78, 79] and reported in the appendix, Tables B.3, B.4, B.5, B.6, B.7, B.8.

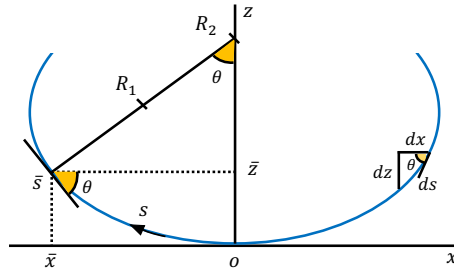


Figure 3.3: Schematic of an axisymmetric drop, modified after Li et al. [77].

3.2.6. CALIBRATION OF THE SETUP

Before starting the main test for the hydrogen gas, the setup was calibrated against the literature data for a nitrogen/brine/quartz system. The literature reports the contact angle of nitrogen on a smooth alpha-quartz crystal surface at a pressure of 13 MPa and temperature of 333K [80]. Under the same experimental conditions, the method used in our study (i.e., captive-bubble method), resulted in the contact angle of $(40.8^\circ \pm 5.9^\circ)$ for nitrogen/brine/Bentheimer sandstone system, which is in close agreement with the

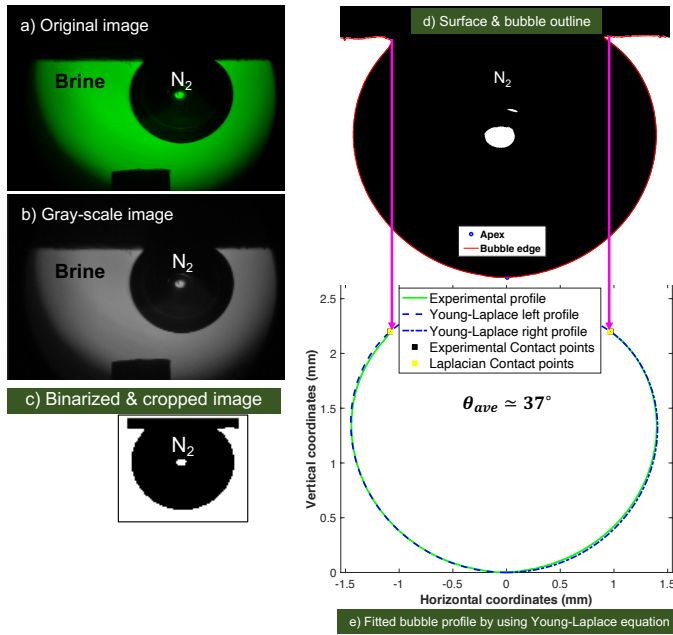


Figure 3.4: The image processing procedure.

reported data [80], i.e, $40.6^\circ \pm 3.9^\circ$. A summary of the validation test is provided in Table 3.2.

Table 3.2: Summary of calibration of the setup with the literature data [80] for nitrogen/brine/sandstone.

Parameters	Literature test [80]	Our test
Liquid phase	5000 ppm NaCl	5000 ppm NaCl
Gas phase	N ₂	N ₂
Rock sample	Smooth alpha-quartz crystal surface	Bentheimer (~95% quartz)
Pressure (bar)	130	130
Temperature (°C)	60	60
Contact angle (°)	40.6 ± 3.9	40.8 ± 5.9

3.2.7. SUMMARY OF THE TEST CASES

Extensive experiments were conducted to examine the effect of pressure, temperature, salinity, and rock type on the contact angle in the hydrogen/brine/sandstone system. The experimental conditions are summarized in Figure 3.5.

3.3. RESULTS AND DISCUSSION

In this section, the results of the experiments will be explained in detail. The impact of each parameter, i.e., pressure, temperature, salinity, and rock type will be separately discussed. Note that, to prove the reproducibility of the results, measurements were repeated up to three times (see appendix Table B.9-B.12).

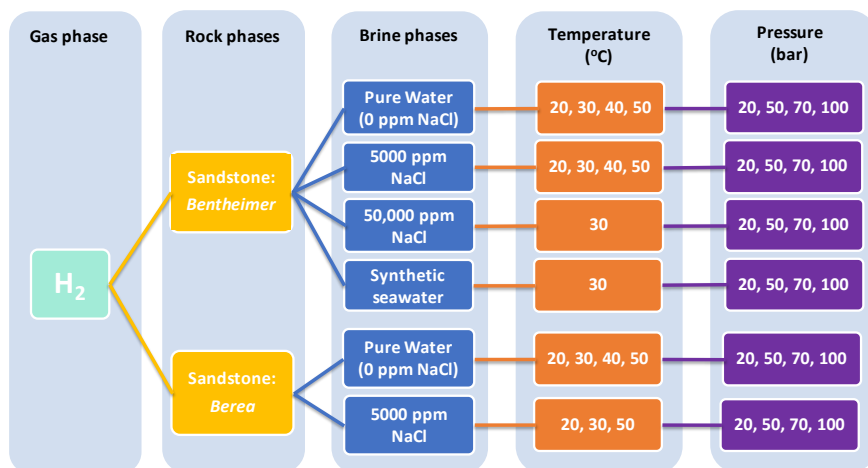


Figure 3.5: Experimental conditions for hydrogen tests.

3.3.1. EFFECT OF BUBBLE SIZE ON THE CONTACT ANGLE

As shown in Figure 3.6, it was noticed that due to the dissolution/diffusion of the hydrogen gas into the brine, the size of the created bubbles continuously decreased during the experiments until they disappeared. Interestingly, as the size of the bubble decreases, the calculated contact angle increases. Similar behavior has been reported by Kaveh et al. [76], Haeri et al. [81], and Jung et al., [82] for CO₂/brine/rock system. Therefore, to capture the effect of the bubble size on the reported contact angles, for each test case, several images were taken from every injected bubble at different times, out of which only four images were analyzed to calculate the minimum and maximum contact angles. The mean contact angle is the arithmetic average of the four measured contact angles, reported in the tables. An example is given in Figure 3.6.a, which results in the contact angles shown in Figure 3.6.b.

3.3.2. TEST CASE 1: EFFECT OF PRESSURE AND TEMPERATURE

Figure 3.7 shows the effect of different pressures and temperatures on the contact angles of the hydrogen/water/Bentheimer system in the absence and presence of NaCl (5000ppm). No obvious correlation was found, as all the data points fall within the accuracy range of the conducted experiments. Detailed results are given in Tables 3.3-3.4.

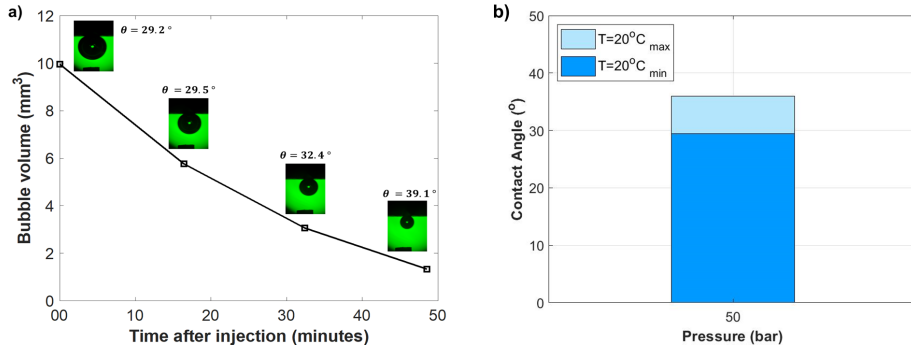


Figure 3.6: Effect of bubble size in the system of hydrogen/water/Bentheimer at 23.5°C and 51.2 bar: a) Volume changes over time, b) Corresponding reported range of contact angles.

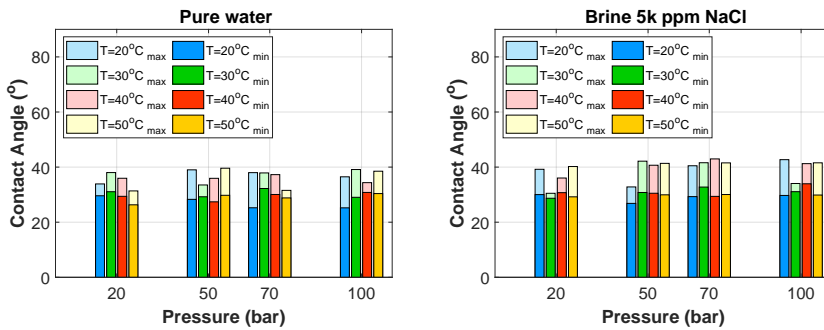


Figure 3.7: Effect of pressure and temperature in the system of hydrogen/brine/Bentheimer at 20, 30, 40 and 50 °C and 20, 50, 70 and 100 bar, pure water (left) and brine with 5000 ppm NaCl (right).

Table 3.3: Contact angle values of hydrogen/pure water/Bentheimer.

Test No.	Temp. (°C)	Press. (bar)	θ_{ave} (°)	θ_{range} (°)	Vol.ave (mm ³)	Vol.range (mm ³)
1 T~20°C	22.3	20.3	30	[28.7, 32.8]	4.56	[2.36, 7.05]
	23.5	50.2	32.6	[29.2, 39.1]	5.49	[1.34, 9.96]
	23.4	70.7	31.1	[25.9, 37.8]	3.93	[1.45, 9.10]
	23.9	100.5	30	[26.0, 36.9]	4.05	[1.48, 7.36]
2 T~30°C	31.9	22	33.7	[30.6, 37.1]	3.48	[2.21, 4.66]
	32.5	51.8	30.5	[29.4, 32.9]	3.09	[2.20, 3.66]
	32.8	71.5	33.9	[32.6, 36.5]	3.39	[2.38, 4.48]
	33.2	100.5	31.7	[29.0, 39.0]	5.27	[1.93, 9.49]
3 T~40°C	39.5	20.3	31.9	[29.0, 35.3]	5.09	[2.61, 8.38]
	39.9	50.2	29.8	[26.3, 35.9]	7.42	[2.21, 12.67]
	40.1	72.8	31.2	[28.9, 36.0]	7.04	[2.27, 12.58]
	40.3	100.3	32	[28.9, 35.2]	3.91	[2.32, 6.02]
4 T~50°C	49.1	19.8	28.4	[26.1, 29.2]	7.42	[3.96, 10.65]
	49.2	50.6	33.2	[29.4, 39.3]	4.7	[1.68, 8.39]
	49.3	70.2	29.8	[28.6, 31.2]	4.41	[2.66, 6.33]
	49.3	101.2	32.8	[29.9, 38.0]	4.12	[2.14, 6.35]

Table 3.4: Contact angle values of hydrogen/brine (5000 ppm NaCl)/Bentheimer.

Test No.	Temp. (°C)	Press. (bar)	θ_{ave} (°)	θ_{range} (°)	Vol.ave (mm ³)	Vol.range (mm ³)
1 T~20°C	21.3	20	33.1	[30.0, 39.2]	3.99	[1.62, 6.14]
	22.1	51.9	29.1	[26.8, 32.8]	4.08	[1.82, 6.53]
	22.3	71.5	33.5	[29.3, 40.5]	3.76	[1.28, 6.50]
	22.9	100.5	33.9	[29.7, 42.7]	4.13	[1.01, 7.37]
2 T~30°C	38.9	21	29.5	[28.7, 30.5]	4.61	[2.67, 6.55]
	32.2	49.9	34.9	[30.8, 42.2]	3.42	[1.21, 5.77]
	32.7	71.1	36	[32.8, 41.6]	2.8	[1.19, 4.72]
	33.1	98.9	31.9	[31.1, 34.1]	5.59	[2.08, 11.13]
3 T~40°C	38.9	19.6	32.7	[30.7, 36.0]	4.33	[2.45, 6.32]
	39.5	50.8	34.1	[30.5, 40.7]	3.91	[1.44, 6.48]
	39.9	69.9	34.3	[29.4, 43.0]	4.06	[1.16, 7.18]
	40.1	100.1	37.3	[34.0, 41.3]	2.24	[1.34, 3.22]
4 T~50°C	47.4	20.7	33.6	[29.2, 40.2]	4.48	[1.51, 7.78]
	48.3	51.3	33.6	[29.9, 41.4]	4.03	[1.40, 6.45]
	49	70.6	34.2	[30.0, 41.5]	4.34	[1.50, 7.91]
	49.2	100.7	33.7	[29.9, 41.6]	5.7	[1.31, 12.66]

3.3.3. TEST CASE 2: EFFECT OF SALINITY

To quantify the impact of salinity, brines with three different salinities, i.e., 0, 5000 and 50,000 ppm NaCl were used at a constant temperature of 30 °C and four different pressures in the range of 20 to 100 bar. The results are shown in Figure 3.8. The change of salinity did not result in a meaningful change in the measured contact angles, indicating that the wetting state of the rock was insensitive to salinity in the presence of hydrogen. Detailed results for salinity of 50,000 ppm NaCl and seawater are also provided in Tables 3.5 and 3.6.

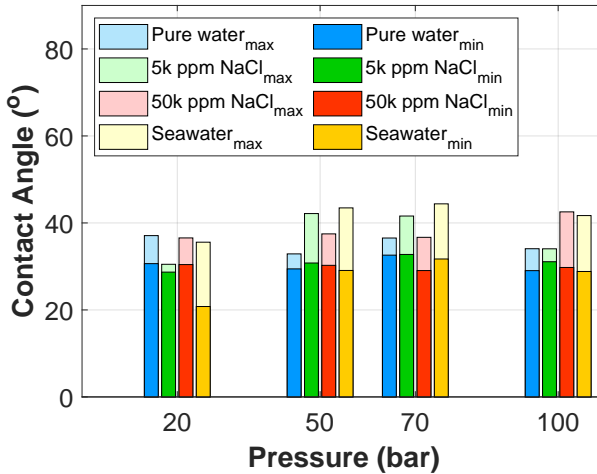


Figure 3.8: Effect of salinity in the systems of hydrogen/brine/Bentheimer using pure water, brine (5000 ppm NaCl), brine (50,000 ppm NaCl), and seawater (36,770 ppm) at about 30 °C for four pressure values of 20, 50, 70, 100 bar.

Table 3.5: Contact angle values of hydrogen/brine (50,000 ppm NaCl)/Bentheimer.

Test No.	Temp. (°C)	Press. (bar)	θ_{ave} (°)	θ_{range} (°)	Vol.ave (mm ³)	Vol.range (mm ³)
1 T~30°C	31.3	21.1	33.3	[30.4, 36.6]	4.02	[2.10, 6.49]
	31.9	51.4	32.8	[30.3, 37.5]	3.54	[1.66, 5.34]
	33	70.6	31.6	[29.1, 36.7]	3.31	[1.53, 5.38]
	33.3	100.7	34.5	[29.8, 42.5]	3.84	[1.36, 5.77]

3.3.4. TEST CASE 3: EFFECT OF ROCK TYPE

Figure 3.9 shows the effect of rock type on the contact angles of the hydrogen/pure water/rock system with Bentheimer and Berea sandstones. No obvious correlation was found, as all the data points fall within the accuracy range of the conducted experiments. Detailed results are given in Tables 3.3, 3.7.

Table 3.6: Contact angle values of hydrogen/brine (synthetic seawater) /Bentheimer.

Test No.	Temp. (°C)	Press. (bar)	θ_{ave} (°)	θ_{range} (°)	Vol. _{ave} (mm ³)	Vol. _{range} (mm ³)
1 T~30°C	31.0	20.5	27.47	[20.8, 35.6]	5.61	[2.62, 8.72]
	31.3	50.2	35.5	[29.1, 43.5]	1.4	[0.42, 2.64]
	31.6	69.6	38.3	[31.7, 44.4]	1.38	[0.61, 2.09]
	31.6	100.7	34.7	[28.8, 41.7]	2.61	[1.11, 4.42]

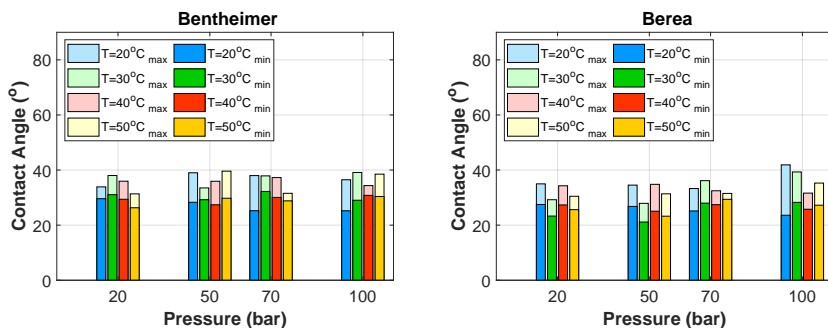


Figure 3.9: Effect of rock type in the system of hydrogen/pure water/rock at 20, 30, 40 and 50 °C and 20, 50, 70 and 100 bar, Bentheimer (left) and Berea (right).

3.4. CONCLUSIONS AND OUTLOOK

The wettability of the rock in contact with brine and hydrogen plays a crucial role in the displacement processes in UHS. This paper reports experimental measurements of the contact angle of the hydrogen/brine/sandstone system, relevant for underground hydrogen storage. This is the first step in understanding and quantifying the impact of different parameters in the accurate prediction of the fate of stored and produced hydrogen. The captive-bubble method was used for measuring the contact angle. To ensure accurate measurements, the setup was successfully calibrated against the existing literature data with nitrogen gas. Then, through several test cases, the intrinsic contact angles were measured under various experimental conditions. It was found that, under our experimental conditions and within the accuracy of the method and setup, the contact angles in the examined systems were not affected by temperature, pressure, and salinity. Under all conditions, the presence of hydrogen did not appear to affect the wettability of the Bentheimer sandstone. All the results indicated water-wet conditions with contact angles in the range of 21.1° to 43°. This general conclusion and contact angles of less than 50° agree well with the conclusions of literature [64, 59]. A major discrepancy between our data and the data reported by [64] is the absence of a general trend between the parameters (pressure, temperature, and salinity) and the measured contact angles. This can be attributed to the differences in the measurement methods, experimental conditions, and sample preparation. It was also observed that the bubble size affects the calculated contact angle values due to the dominance of gravity for the larger gas bubbles, and possibly different surface composition of the rock.

The presented experimental data and images are all made digitally available open-

Table 3.7: Contact angle values of hydrogen/pure water/Berea.

Test No.	Temp. (°C)	Press. (bar)	θ_{ave} (°)	θ_{range} (°)	Vol.ave (mm ³)	Vol.range (mm ³)
1 T~20°C	23.6	20.8	30.4	[27.5, 34.9]	4.96	[1.14, 9.19]
	23.5	50.6	29	[26.8, 34.5]	5	[0.96, 10.74]
	23.7	70.2	29.1	[25.2, 33.3]	5.22	[1.04, 10.28]
	23.9	100.7	29.6	[23.6, 41.9]	4.17	[0.33, 9.51]
2 T~30°C	32.6	19.4	26.1	[23.3, 29.2]	7.65	[1.36, 15.81]
	32.7	50	23.6	[21.1, 27.9]	7.28	[0.79, 14.17]
	32.8	69.3	31.2	[27.9, 36.1]	3.38	[0.54, 7.29]
	33	101.1	31.7	[28.3, 39.3]	3.61	[0.45, 8.59]
3 T~40°C	38.6	21.2	31.1	[27.3, 34.3]	3.01	[0.95, 5.64]
	38.6	51	29.5	[25.1, 34.8]	4.34	[0.94, 9.68]
	38.6	69.4	29.4	[27.4, 32.5]	3.56	[1.17, 7.14]
	38.9	100.7	28.9	[25.8, 31.6]	4.98	[1.52, 10.35]
4 T~50°C	47.6	20.5	27	[25.6, 30.5]	5.57	[0.91, 10.51]
	47.8	49.4	26.4	[23.2, 31.4]	6.49	[0.93, 14.03]
	48.2	70.6	30.1	[29.4, 31.5]	6.68	[5.13, 8.52]
	48.2	99.7	30.5	[27.2, 35.3]	4.55	[0.91, 9.80]

source at https://gitlab.tudelft.nl/ADMIRE_Public/PoreScale_H2 repository.

4

CONTACT ANGLE FOR MIXTURES OF HYDROGEN-METHANE /BRINE/SANDSTONE SYSTEM

"In the midst of chaos, there is also opportunity."

Sun Tzu

Characterizing the wettability of hydrogen (H_2) - methane (CH_4) mixtures in subsurface reservoirs is the first step towards understanding containment and transport properties for underground hydrogen storage (UHS). In this study, we investigate the static contact angles of H_2 - CH_4 mixtures, in contact with brine and Bentheimer sandstone rock using a captive-bubble cell device at different pressures, temperatures, and brine salinity values. It is found that, under the studied conditions, H_2 and CH_4 show comparable wettability behavior with contact angles ranging between $[25^\circ - 45^\circ]$; and consequently their mixtures behave similarly to the pure gas systems, independent of composition, pressure, temperature, and salinity. For the system at rest, the acting buoyancy and surface forces allow for theoretical sensitivity analysis for the captive-bubble cell approach to characterize the wettability. Moreover, it is theoretically validated that under similar Bond numbers and similar bubble sizes, the contact angles of H_2 and CH_4 bubbles and their mixtures are indeed comparable. Consequently, in large-scale subsurface storage systems where buoyancy and capillary are the main acting forces, H_2 , CH_4 , and their mixtures will have similar wettability characteristics.

Parts of this chapter have been published in *Advances in Water Resources* **163**, 104165(2022) [83].

4.1. INTRODUCTION

The development of large-scale (TWh) energy storage technologies is essential in the successful transition towards renewable energy systems. Therefore, energy has to be converted into forms that can be stored at such large scales. One of the attractive energy carriers is hydrogen (H_2), due to its high energy content per mass, 141.86 MJ/kg, and its carbon-free combustion products [84]. However, there exists a major challenge in the development of storage technologies for hydrogen. Being the lightest molecule, its volumetric energy content is relatively low [41, 85]. More specifically, it stores only about 132 KWh in 1 m^3 at a relatively high pressure of 50 bars and temperature of 298 K [86]. As such, to achieve feasible large-scale storage for compressed hydrogen gas, gigantic volumes are needed. These volumes are beyond the technical, economical, land-usage, and safety scope of surface-based storage tanks [87, 88]. Underground reservoirs, on the other hand, provide giant volumes to store hydrogen in the expected TWh scales. These formations can be in the form of solution-mined salt caverns [14] or geological porous reservoirs [89, 15, 39], including depleted hydrocarbon fields and saline aquifers [35].

There exist a few experiences with storing hydrogen or its mixture with methane in porous reservoirs [90, 91] and several pilot projects are currently underway [92, 93]. However, to date, a rigorous understanding of many aspects related to the subsurface storage of pure hydrogen and its mixture with methane is still lacking [1].

In some aspects, underground hydrogen storage (UHS) is similar to that of underground gas storage (UGS), as both are compressed gases being stored cyclically in subsurface formations. However, in many aspects, UHS is expected to behave quite differently than UGS. Firstly, H_2 is very different than CH_4 gas, in its molecular weight, diffusivity, dissolution, density, and surface/interfacial tension. Secondly, the cyclic loading and frequency of the green hydrogen injection and production, supplied by the intermittent green energy production, is expected to be much different than that of UGS. Lastly, hydrogen purity is expected to be maintained during the storage period, as sensitivities towards hydrogen impurities in fuel cells are very high [94]. These differences have recently motivated the scientific community to study hydrogen properties in detail, specially its wettability characteristics in contact with reservoir brine and rock [64, 63, 95]. This is due to the fact that hydrogen will come in contact with brine whether in aquifers or porous rocks containing connate water [35, 1].

H_2 /brine/rock wettability is a key factor in the identification of the hydrogen interaction with reservoir brine and rock. More precisely, it allows for understanding the distribution of hydrogen through the porous rock microchannels. According to Young's equation, it is characterized by the contact angle between the interface of gas/brine in contact with the rock surface [96], i.e.,

$$\cos \theta = \frac{(\sigma_{rb} - \sigma_{rg})}{\sigma_{bg}}. \quad (4.1)$$

Here, σ_{rb} , σ_{rg} , σ_{bg} correspond to the interfacial forces between each pair of the phases, respectively: rock/brine, rock/gas, and brine/gas [97].

Typically, in geological reservoirs, the adhesive forces between brine and rock are much bigger than between gas and rock, because molecules in the liquid phase are much closer

to each other than in the gas phase. Therefore, the contact angle in gas/brine/rock systems is likely to be less than 90 degrees. Consequently, water-wet conditions can be expected during underground hydrogen storage. The distribution of hydrogen and brine in the porous rock influences multiphase flow properties such as relative permeability and capillary pressure. In water-wet systems, the non-wetting phase, in our case hydrogen, will preferentially flow through the larger pores resulting in a higher relative permeability. This facilitates the injectivity of the reservoir, while the amount of capillary-trapped hydrogen will be smaller. Both aspects are favorable for UHS [98, 99].

Wettability of the H₂/brine/rock system has been the focus of some recent studies, all of which were conducted using water-wet rocks [59, 100, 64, 63] with pure hydrogen gas. These studies collectively revealed static [63] and dynamic [59, 100, 64, 95] contact angles of hydrogen by different experimental methods: captive-bubble cell [63, 101], tilted-plate [64, 95], microfluidics [100] and indirectly [59] and directly [101] through core-flooding techniques. A summary of the measured contact angles as well as the conditions and experimental techniques can be found in Table 4.1.

The characterisation of H₂-CH₄ wettability is important for the comparison of UHS and UGS. Despite its importance, there exists no rigorous study that investigates and reports how hydrogen wettability compares with that of methane and hydrogen-methane mixtures of different concentrations. In addition, there can be cases in which H₂ mixes with the reservoir CH₄, for example, if it is used as cushion gas or traces of it exist in the subsurface environment, such as depleted gas fields. Moreover, it is important for industrial applications where first H₂-CH₄ mixture is introduced in the gas grid and storage facilities. As the production of H₂ scales up in the future, the fraction of H₂ concentration in the mixture is expected to be further increased. For example, the first UHS project in Europe, Underground Sun Storage by RAG Austria AG, stored 20% H₂ and 80% CH₄ [102] in a porous reservoir.

Mixing of H₂ with CH₄ impacts the physio-chemical properties of the injected hydrogen and consequently its displacement process [103, 104, 105, 106]. This can potentially impact the upscaled multiphase flow functions of capillary pressure and relative permeability [35, 107, 68, 108, 109]. A correct description of these upscaled flow functions is needed to ensure the safety of underground hydrogen storage, as well as to optimize the cyclic injection and production of hydrogen. As such, characterisation of the H₂-CH₄ mixture wettability is crucially important, which is the focus of the present study.

In this work, we directly measure the static contact angles of H₂-CH₄ mixtures in contact with brine and sandstone rock using a captive-bubble cell experimental methodology [76, 63]. We systematically analyse contact angles of different size gas bubbles and different mixture concentrations. By providing a modeling analysis, we validate our methodology and the findings of this study. The structure of the paper is as follows. In the Materials and Methods section, a description of the methodology and test conditions are presented in detail. This is followed by the results and interpretation of the data. A sensitivity analysis is also performed, on the basis of the Young-Laplace equation, to better analyse and justify the experimental observations. Finally, the main learning points are presented in the conclusion.

Table 4.1: Overview of the reported measurements for the range of advancing (ACA), receding (RCA), and static (SCA) contact angles for H₂-brine systems. Here (S) stands for sandstone porous rock.

Measuring technique	ACA (°)	RCA (°)	SCA (°)	P (bar)	T (°C)	Brine phase	Medium
Captive-bubble cell ¹			25-45	20-100	20-50	0-50k NaCl	Bentheimer (S)/Berea (S)
Captive-bubble cell ²			27-39	68.9-206.8	25	0-5k NaCl	Bentheimer (S)
Tilted plate ³	0-48.3	0-44.1		50-250	23-70	100k NaCl	Quartz
Microfluidics ⁴	13-39	6-23		10	20	pure water	Borosilicate glass
Indirect Core-flood ⁵		21.6, 34.9		50, 100	20, 45	pure water	Vosges (S)
Direct Core-flood ²			39.77, 59.75	6.9 - 172.4	25	0-2k KI	Bentheimer (S)

¹[63], ²[101], ³[64], ⁴[100], ⁵[59].

4.2. MATERIALS AND METHODS

In this study, static contact angles for H₂-CH₄ gas mixtures, as well as pure CH₄ gas, in contact with brine and Bentheimer sandstone rock are measured using the captive-bubble cell device [76, 63].

4.2.1. MATERIALS

The gas mixtures consisted of 99.99 mol % purity H₂ and 99.5 mol % purity CH₄ both produced by Linde-gas Company. The gas mixture was prepared by filling up the pump with both gases in the desired concentration at the desired pressure, having the pump with the gasses stand for one day so to allow for a fully mixed gas-liquid system. The brines were made by dissolving NaCl in deionized water. A Bentheimer sandstone rock slab with dimensions of 30 × 6 × 12 mm was used in the experiments. The sample was untreated and cut from the same clean Bentheimer sandstone block as in the Bentheimer rock sample used in [63]. The permeability of the sample was 2-3 Darcy and the porosity was around 20 %. The mineral composition consisted for 95% of quartz which was evenly distributed throughout the rock matrix [72]. The surface roughness was 0.03 mm and was determined by microscopic analysis [63]. The experimental conditions used for each H₂-CH₄ gas mixtures and pure CH₄ gas can be found in Table 4.2.

Table 4.2: Experimental conditions.

Rock phase	Gas phase	Brine phase (ppm)	Temperature (°C)	Pressure (bar)
Bentheimer Sandstone	CH ₄	Pure water	30, 50	20, 50, 70, 100
		5k NaCl		
	50k NaCl			
	20% CH ₄ - 80% H ₂	Pure water	30, 50	20, 50, 70, 100
50% CH ₄ - 50% H ₂	5k NaCl			
	Pure water	30, 50	20, 50, 70, 100	
80% CH ₄ - 20% H ₂	5k NaCl			
	Pure water	30, 50	20, 50, 70, 100	
		5k NaCl		

4.2.2. EXPERIMENTAL APPARATUS AND PROCEDURE

A schematic of the experimental apparatus can be seen in Fig. 1 of C.1. It is similar to the setup used by [63], adapted in this study for gas mixtures. The apparatus consisted of a high-pressure/high-temperature single steel cell with a volume of 150ml filled with brine. The rock sample was attached to the center of the cell. The cell was placed in an oven to control the temperature. Brine was continuously injected at a flow rate of 0.02ml/min from the bottom of the cell. The pressure was regulated with a back-pressure device connected to the top of the cell and attached to an N₂ cylinder. Gas bubbles of approximately 2mm in diameter were released from a nozzle at the bottom of the cell into the brine. The bubble buoyantly rose until it reached the rock surface. The bubble slowly dissolved and diffused into the brine resulting in bubbles of different sizes. Images with a resolution of 6.9 MP (3216×2136) were taken at evenly spaced time intervals using a Canon 90 camera (with a maximum resolution of 12.3 MP) attached to an endoscope. The pressure and temperature in the cell were continuously monitored. The lines of the system were thoroughly cleaned with water and ethanol at the start of each experiment to avoid any impact of contamination on the contact angle measurements.

4.2.3. IMAGE ANALYSIS

Contact angles were derived for each of the images taken during the experiment using an in-house MATLAB code which is based on the ADSA-P technique [77]. The ADSA-P technique fits the best theoretical Laplacian curve on the physically observed bubble interface and is based on the Young-Laplace equation (Next section). For this purpose, the images are cropped and binarized such that the interface including the apex and contact points can be detected. To find the size of the bubble, the outer diameter of the nozzle is used. The brine and gas density values used in the analysis are reported in C, Tables 12 - 22. For more details about the image analysis procedure, the reader is referred to [63].

4.2.4. THEORETICAL ANALYSES BASED ON YOUNG-LAPLACE EQUATION

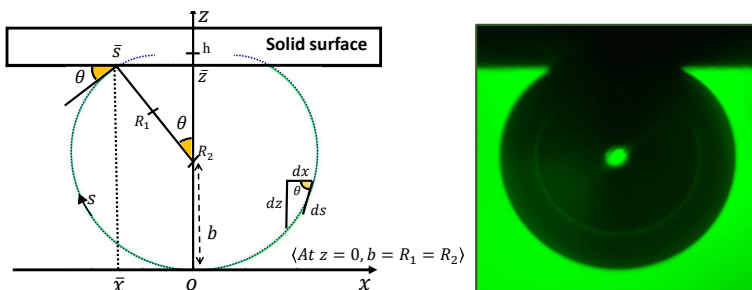


Figure 4.1: Schematic of an axisymmetric gas bubble below a solid rock surface (left). The blue contour indicates the gas/brine interface. Shown on the right is an image of a H₂-CH₄ mixture bubble in contact with porous sandstone rock, captured by the camera.

Figure 4.1 shows a schematic of an axisymmetric gas bubble. The blue contour indicates the gas/brine interface. The pressure difference across this interface, i.e., ΔP , can be described by the Young-Laplace equation [77] as

$$\Delta P = \sigma \left(\frac{1}{R_1} + \frac{1}{R_2} \right), \quad (4.2)$$

where σ [N/m] is the interfacial tension and R_1 [m] and R_2 [m] are the principle radii of the curvature. The pressure difference across the interface is due to the interfacial tension, as well as the force of gravity, i.e.,

$$\Delta P = \Delta P_0 + \Delta P_g. \quad (4.3)$$

At gravity-capillary equilibrium, the pressure difference across the interface can be described as a function of depth, z [m], i.e.,

$$\Delta P = \Delta P_0 + \Delta \rho g z. \quad (4.4)$$

Here, $\Delta \rho$ [kg/m³] is the density difference between the gas and the brine phase, and g [m/s²] is the gravitational acceleration. Since the apex point is taken as the reference, i.e., $z = 0$, no gravity term is considered there and thus one can write $R_1 = R_2 = b$ at this point. Therefore, at the apex point, Eq. 4.2 can be written as

$$\Delta P_{apex} = \frac{2\sigma}{b}. \quad (4.5)$$

By substituting Eq. 4.4 into Eq. 4.2 it is found that

$$\sigma \left(\frac{1}{R_1} + \frac{1}{R_2} \right) = \frac{2\sigma}{b} + \Delta \rho g z \quad (4.6)$$

holds for any depth (z). In cylindrical coordinates, one can write

$$\frac{1}{R_1} = \frac{d\theta}{ds} \quad (4.7)$$

and

$$\frac{1}{R_2} = \frac{\sin\theta}{x}. \quad (4.8)$$

Here θ [°] is the contact angle and s [m] is the distance along the surface contour, as illustrated in Fig. 4.1. By replacing R_1 and R_2 in Eq. 4.6 with Eqs. 4.7 and 4.8, respectively, one obtains

$$\frac{d\theta}{ds} = \frac{2}{b} + \frac{\Delta \rho g z}{\sigma} - \frac{\sin\theta}{x}. \quad (4.9)$$

Equation 4.9 can be stated in dimensionless form as

$$\frac{d\theta}{ds^*} = \frac{2}{b^*} + \frac{\Delta \rho g R^2}{\sigma} z^* - \frac{\sin\theta}{x^*}, \quad (4.10)$$

where the bubble radius R is used as characteristic length scale, i.e., $x^* = x/R$, $s^* = s/R$, $b^* = b/R$, $z^* = z/R^2$. The second term on the right hand side of Eq. 4.9 is the Bond number (N_{Bo}), defined as

$$N_{Bo} = \frac{\Delta\rho g R^2}{\sigma}. \quad (4.11)$$

N_{Bo} is the ratio of gravitational forces to interfacial forces [110, 111, 112].

4.3. RESULTS AND DISCUSSION

Contact angles for H₂-CH₄/brine/rock systems were measured using the captive bubble cell method. Although this method does not take into account the impact of pore structures and flow dynamics on wettability, it sheds light on the wettability behavior in systems where buoyancy and capillary are the main driving forces. Furthermore, it provides insights into the overall wettability state of sandstone rock in contact with gas mixtures of H₂-CH₄ and brine. The experiments were carried out for a range of pressures, two temperatures, and two different brine salinities, the results of which can be seen in Fig. 4.3 and Tables 1 - 11 of C. The results for pure H₂ are based on the experimental observations of [63] who used the same captive-bubble cell device to measure contact angles for the H₂/Brine/Bentheimer system. In addition, in Fig. 4.6 the contact angles for pure H₂ measured on a third Bentheimer sandstone sample are presented to highlight the systematic change in contact angle that is observed when different samples are used. All Bentheimer sandstone samples used in this study were cut from the same Bentheimer sandstone block. To verify whether changes in the chemical composition or rock structure occurred over time and consequently changed the contact angle, experiments were repeated. Figure 4.2a shows the contact angle for different bubble sizes for three hydrogen experiments carried out on the same rock slab. Between each of the experiments, the rock slab was taken out of the apparatus and put in the vacuum oven to dry. It can be seen that similar results were obtained for each of these experiments. This indicates that no mineral alteration or other changes in the structure of the rock surface have taken place that significantly impacted the wettability.

The bubble size decreased with time, which is likely due to dissolution and diffusion into the brine. To verify whether dissolution into the brine would have an impact on the contact angle measurement, experiments were carried out using brine with different levels of hydrogen saturation. Figure 4.2a shows the contact angle versus volume while Figure 4.2b shows the contact angle versus time for a system where the brine was highly saturated with hydrogen and a system where the brine was unsaturated. It can be seen that the dissolution rate of the unsaturated brine is almost 10 times higher than the (highly) saturated brine. However, the contact angles obtained are the same in each of the experiments. This shows that the contact angle is a function of the bubble size and does not depend on the saturation level. Using unsaturated brine allowed us to make contact angle measurements for a range of bubble sizes. It is observed that the contact angle increases with decreasing bubble size. The minimum and maximum contact angle values in Fig. 4.3 correspond to the largest and smallest bubble sizes.

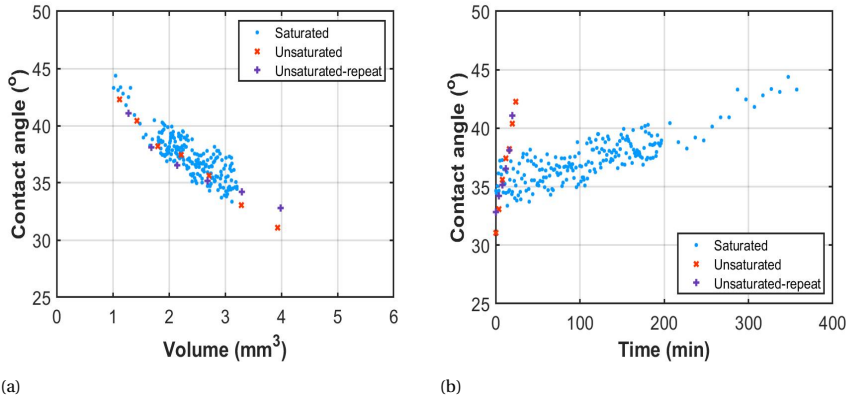


Figure 4.2: Contact angle versus volume (a) and time (b) for a system where the brine was highly saturated with hydrogen (blue dots) and a system where the brine was unsaturated (red and purple dots). For the experiment with the highly saturated brine images were taken every minute for the first 197 minutes, after which images were taken every 10 minutes. For the experiments with unsaturated brine images were taken every 4 minutes.

4.3.1. EFFECT OF BUBBLE SIZE AND GAS COMPOSITION

The gas bubbles were released in under-saturated brine solutions and slowly dissolved and diffused into the brine. Images were taken every minute, except for pure H₂, where the time-step between images was four minutes. For each of these images, the contour of the interface was detected and contact angles were calculated. Figure 4.4 shows the contours of the interfaces at each time-step as well as the corresponding bubble volume and contact angle for three H₂-CH₄ mixtures, pure H₂ and pure CH₄, for a system with pure water at 30 °C and 100 bar. Due to the roughness of the sample pinning of the gas bubble occurred and as a result, the dissolution was not symmetric. In some cases, this pinning led to higher contact angles as can be observed in figure 4.4 for 50% H₂-CH₄ mixture for bubbles bigger than 4 mm³. Overall, the gas bubbles of the different mixtures show comparable behaviour. Although, the contact angles of the H₂ bubbles are slightly higher. This is likely due to the fact that a different Bentheimer sandstone sample, although obtained from the same block, was used for the H₂ experiments since the contact angles of the different mixture compositions are indistinguishable. The contact angle is a function of the bubble volume and no distinction can be made between the different gases. This behavior of increasing contact angle with decreasing bubble volume has also previously been reported for CO₂/brine/rock systems [76, 113, 81, 82].

4.3.2. EFFECT OF PRESSURE, TEMPERATURE AND SALINITIES

For all experimental conditions, water-wet behaviour was observed with contact angles ranging between [25°–45°] for all H₂-CH₄ mixtures as well as for pure H₂ and pure CH₄ as can be seen in Fig. 4.3. No obvious correlation between the measured contact angle and the pressures, temperatures, or salinity could be observed. Note that the range of bubble sizes was different for the different experiments. High contact angle values correspond to smaller bubble sizes. However, for similar bubble sizes, all the data points

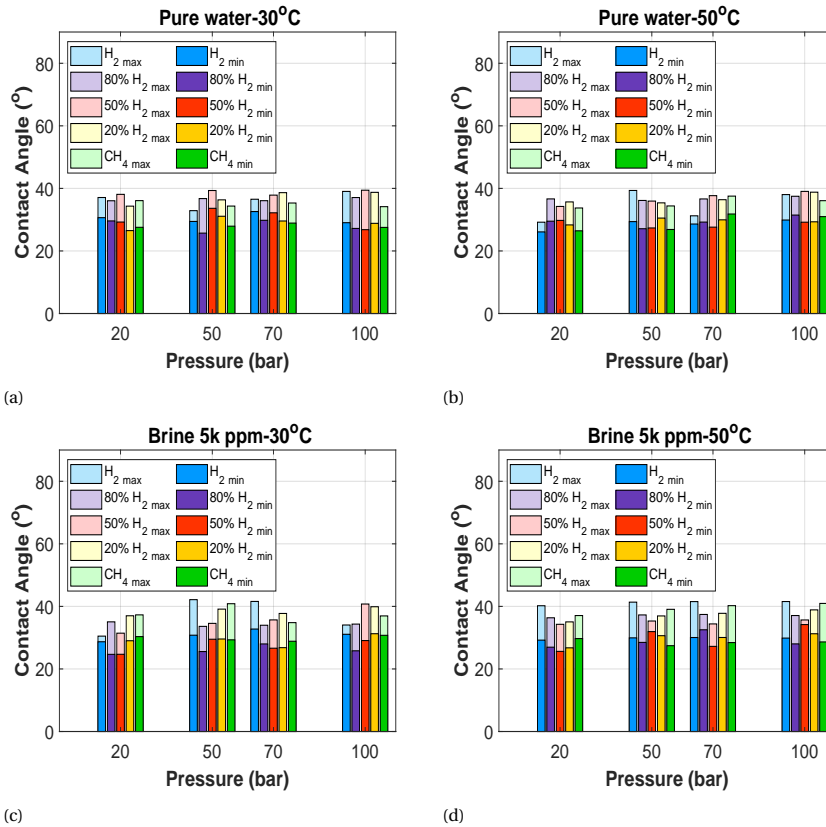


Figure 4.3: Contact angle results for all 5 different gas compositions as a function of pressure and 2 different temperatures of 30°C and 50°C, pure water (a, b) and brine 5000 ppm NaCl (c, d) in contact with Bentheimer sandstone. The results for pure H₂ are based on the experimental observations of [63].

fall within the accuracy range of the conducted experiments ($\pm 3^\circ$). To validate our findings a sensitivity study of the captive-bubble cell approach to measure wettability, based on the Young-Laplace equation, has been performed. This is presented in the following section.

4.3.3. SENSITIVITY ANALYSIS OF THE CAPTIVE-BUBBLE CELL APPROACH

The contact angles presented in this study were obtained by fitting Eq. 4.9 onto the captured images of the gas bubbles. A closer look at Eq. 4.9 shows that three parameters impact the fitting curve formula: apex radius (b), density difference ($\Delta\rho$) and interfacial tension (σ), of which the combined impact can be characterized by the Bond number, as defined in Eq.4.11. To investigate the impact of each of these three parameters on the contact angle, a systematic sensitivity analysis has been performed, the results of which can be seen in Fig. 4.5.

Based on the experimental observations, the ratio of the surface position to the height h ,

(see the Fig. 4.1) is changing from 0.8 to 0.95, corresponding to the biggest and smallest bubble sizes, respectively. Therefore as the base-case, σ was set to 60 mN/m , $\Delta\rho$ to 1000 kg/m^3 , b to 1 mm and the surface location, z , was set to 0.9 of the bubble height. It is important to note that the ratio of the surface position to the height h depends on the wetting state of the system.

Figure 4.5a shows the results of the analysis for the apex radius effect. It can be seen that the contact angle increases with decreasing apex radius, similarly as was observed from the experiments. The effect of the density contrast on the contact angle is presented in Fig. 4.5b. Here, the contact angle increases with decreasing $\Delta\rho$. However, for the $\Delta\rho$ of this study, which is in the range of $900\text{--}1000 \text{ kg/m}^3$ the contact angle ranges between $[41.7\text{--}43.4]^\circ$, which is within the accuracy range of the measuring technique. Figure 4.5 shows the effect of interfacial tension on the contact angle. It can be seen that the contact angle increases with increasing interfacial tension. For the pressures and temperatures of our study, the interfacial tensions of the different $\text{H}_2\text{-CH}_4$ mixtures likely ranged between $[50\text{--}70] \text{ mN/m}$ [84, 114, 115]. In this range, the contact angle varies between $[38.3^\circ\text{--}44^\circ]$. For a particular set of conditions, this is again within the accuracy range of the measuring technique. The above analysis shows that no significant pressure, temperature, and salinity dependency is expected in systems where buoyancy and capillarity are the main driving forces such as our captive bubble cell, which validates our results. However, in different systems where other driving forces come into play, including different experimental measurement techniques, these factors could have a bigger impact on the contact angle, as has been observed in the literature.

The Bond number for the H_2/water and CH_4/water experiments are plotted in Fig. 4.6a, as a function of radius at the apex point. It can be seen that the Bond numbers of both the H_2/water and CH_4/water systems are comparable, and depend on the size of the bubble. Figure 4.6b shows that under similar Bond numbers and similar bubble sizes, the contact angles of H_2 and CH_4 bubbles and their mixtures are indeed comparable. The slight difference between the contact angle plots is due to the fact that different Bentheimer sandstone samples were used.

The experiments of this study were carried out for pressures ranging between $[20\text{--}100]$ bar and temperatures between $[20\text{--}50]$ °C. Bond numbers for much higher pressures $[0\text{--}450]$ bar and temperatures $[25\text{--}175]$ °C were also calculated and plotted in Fig. 4.7, using the literature values for σ and $\Delta\rho$. It can be seen that the Bond number stays relatively constant through the entire studied range, and only a small increase with temperature is observed. This analysis shows that the Bond numbers of H_2 and CH_4 are indeed comparable, even for this wide range of conditions. This indicates that in real field processes in which buoyancy and capillary are the main acting forces, H_2 , CH_4 , and their mixture in contact with brine, will have similar wettability characteristics independent of pressure and temperature.

4.4. CONCLUSIONS

In this study static contact angles for $\text{H}_2\text{-CH}_4$ mixtures, pure H_2 and pure CH_4 in contact with brine and Bentheimer sandstone rock were measured using the captive-bubble cell device for a range of pressures (20-100bar), two temperatures (30°, 50°), and two salinities (pure water, 5000ppm). Strongly water-wet conditions were observed with contact

angles ranging between $[25^{\circ}-45^{\circ}]$ for all $\text{CH}_4\text{-H}_2$ mixtures. All of the gas mixtures showed comparable behaviour and no pressure, temperature, or salinity dependency was observed. The size of the injected gas bubbles decreased with time due to dissolution and diffusion into the brine, which allowed for static contact angle measurements for various bubble sizes. Our analysis showed that contact angles increased with decreasing bubble volume.

For the static system, the acting buoyancy and surface forces allow for analytical sensitivity analysis for the captive bubble cell approach, which is based on the Young-Laplace equation, to characterise the wettability. Three parameters in the Young Laplace equation affect the contact angle: radius at the apex, density difference, and interfacial tension. The sensitivity analysis showed an increase in contact angle for a decrease in radius at the apex similar to what was observed in the experiments. Furthermore, for the range of interfacial tensions and density differences that correspond to the experimental conditions of this study, the analysis showed that the changes in contact angle are such that they fall within the accuracy range of the experiment validating our results.

It is mathematically shown that for comparable bubble sizes and under similar Bond numbers the contact angles of hydrogen and methane bubbles and their mixtures in contact with brine will indeed be comparable. This indicates that for real field processes in which buoyancy and capillary are the main acting forces, hydrogen, methane, and their mixture will have similar wettability characteristics.

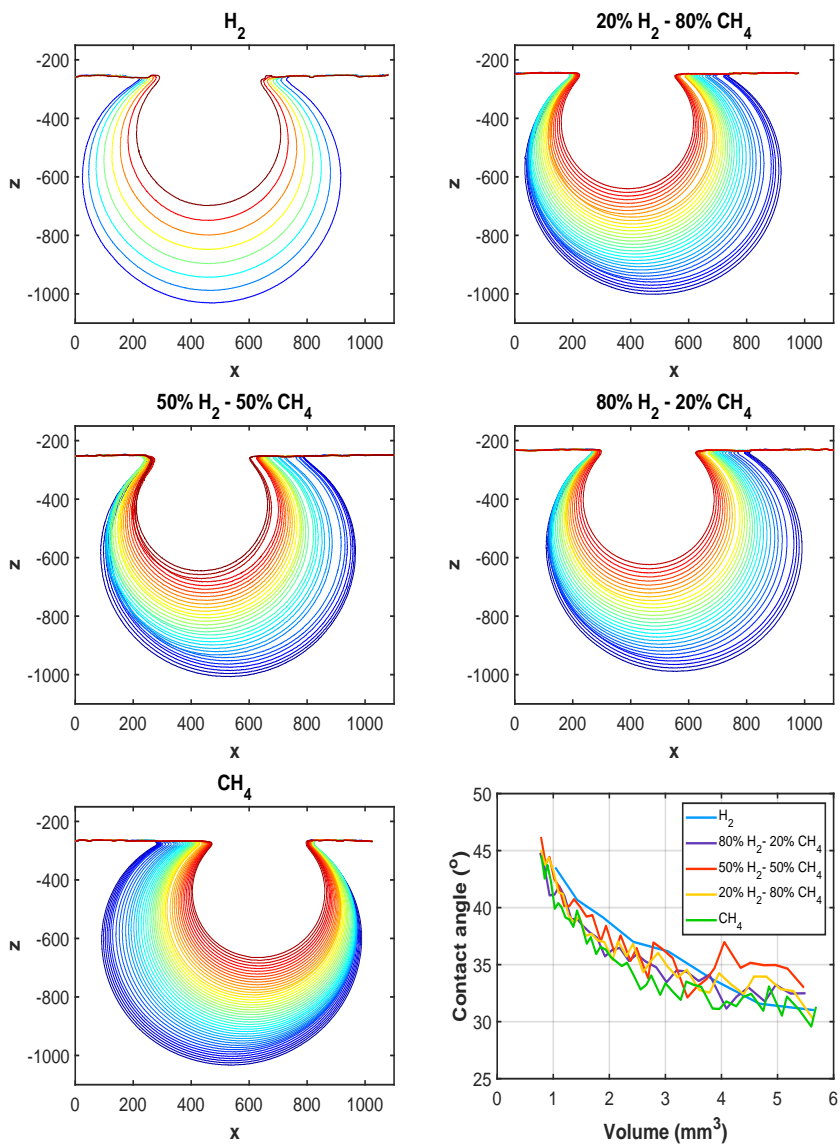


Figure 4.4: Bubble contours over time for 5 different gas compositions and pure water in contact with Bentheimer sandstone, at 30°C and 100 bar, and their contact angles versus bubble volumes (f).

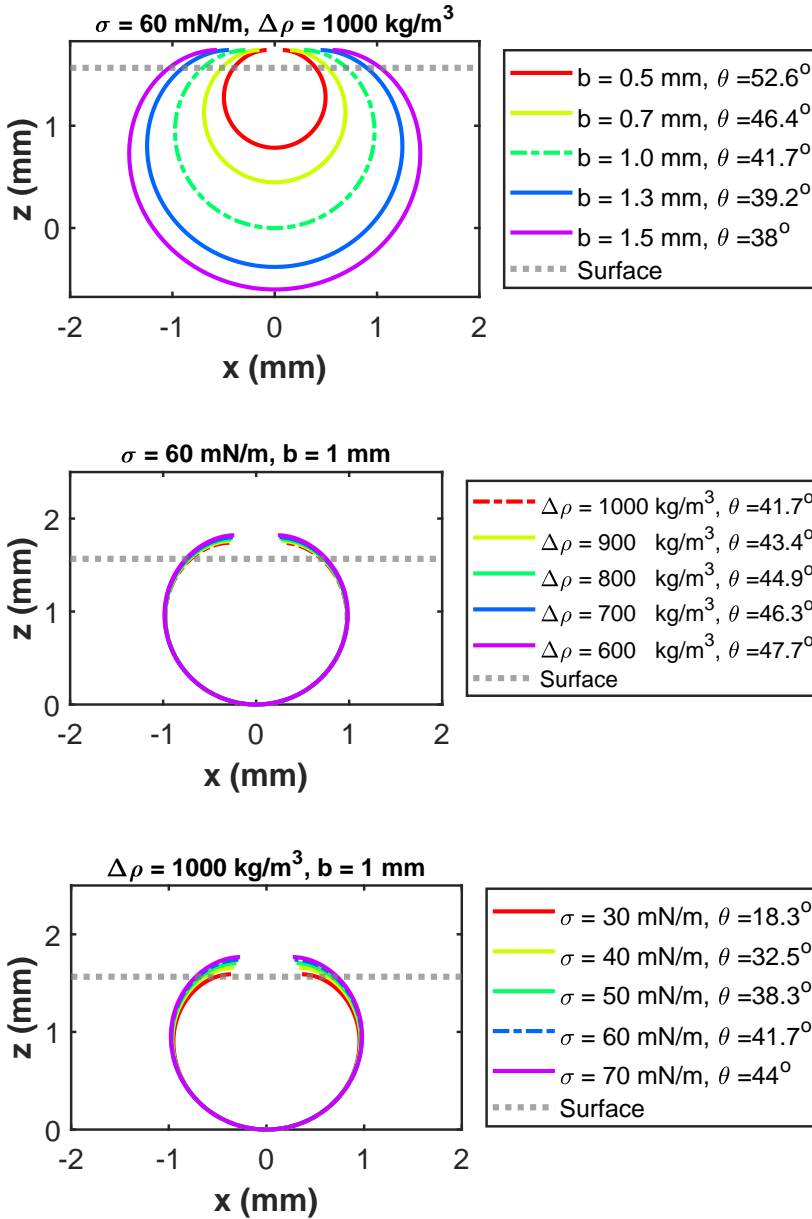


Figure 4.5: Sensitivity analysis for the captive-bubble method for wettability characterization: effect of apex radius (top), density difference (middle), and interfacial tension (bottom) on the contact angle.

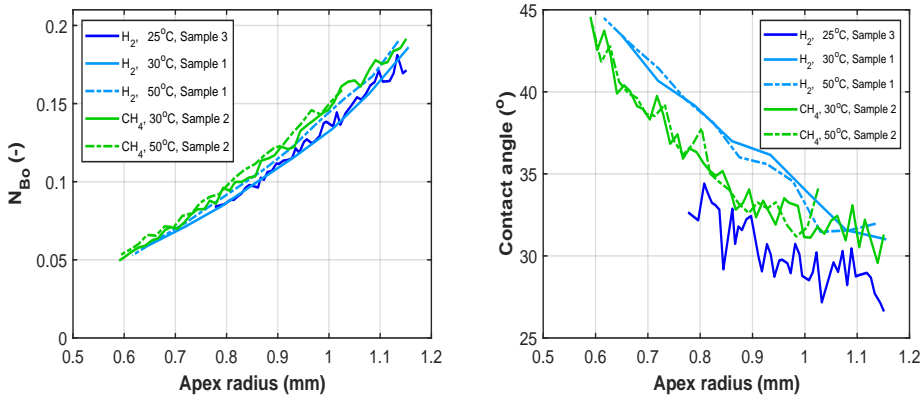


Figure 4.6: Bond number (left) and contact angle measurements (right) for H_2 and CH_4 versus different apex radii corresponding to the bubble size changes over time, at the fixed pressure of 100 bar and temperatures of $30^\circ C$ and $50^\circ C$. The slight difference between the contact angles of H_2 and CH_4 is due to the fact that different samples were used because Fig. 4.4 (bottom right) shows that for the same samples, the contact angles match.

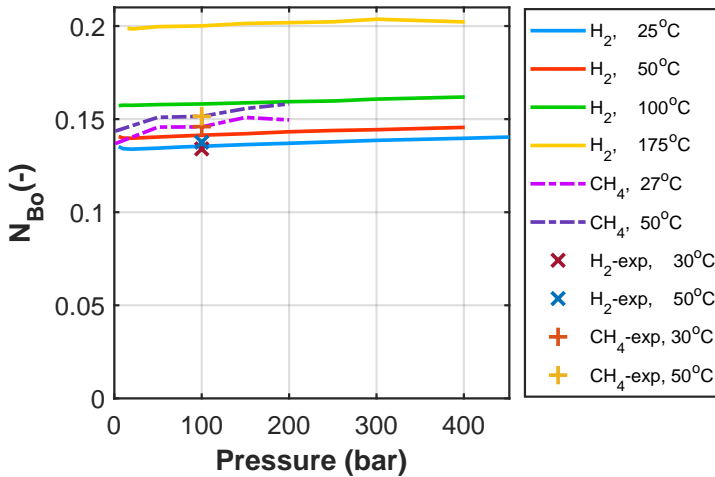


Figure 4.7: Theoretically calculated Bond number based on the IFT [114] and density [115] values of H_2 and CH_4 from the literature. Calculations are made for the constant apex radius of 1 mm. The x and $+$ markers indicate the Bond numbers corresponding to Fig. 4.6 with the apex radius of 1 mm.

5

DYNAMIC PORE NETWORK MODEL

"A wise person can learn more from a foolish question than a fool can learn from a wise answer."

Bruce Lee

This study explores the suitability of quasi-static pore-network modeling for simulating the transport of hydrogen in networks with box-shaped pores and square cylinder throats. The dynamic pore-network modeling results are compared with quasi-static pore-network modeling, and a good agreement is observed when the simulations reach steady-state, for a capillary number of $N_c \leq 10^{-7}$. This finding suggests that the quasi-static approach can be used as a reliable and efficient method for studying hydrogen transport in similar networks.

Parts of this chapter have been submitted to the journal of Advances in Water Resources.

5.1. INTRODUCTION

Underground Hydrogen Storage (UHS) in porous formations is a promising technology for large-scale (TWh) energy storage. To ensure the efficiency of the storage operation, multiscale modeling and simulation strategies are essential, in which the micro-scale physics are studied to derive input parameters for the continuum-scale dynamic models. Therefore to extend the initial study of this complex process using quasi-static pore-network modelling [35] and properly characterize the dynamics of the system, the present study uses a dynamic pore-network modeling (D-PNM) approach [116] to simulate the immiscible two-phase flow of hydrogen and water through a pore network model of a porous structure. The model input parameters are based on the experimentally obtained fluid-gas properties as presented in the literature [35]. As for the rock, statistical pore network models are generated to mimic the digital network information which is based on 3D X-ray images of porous samples. To preserve the simulation stability, the developed D-PNM solves the transient multi-phase Stokes equations fully implicitly, for pressure and phase volume concentrations. Through several test cases, we analyze the transport characteristics of the hydrogen/water interface, especially the fingering and spreading physics. These results shed new light on how a representative continuum-scale model should be created to study the process at the field scale.

Pore network modelling

Large-scale numerical simulation of multi-phase flow in porous media is crucial for predicting various phenomena in hydrology, environmental engineering, and petroleum engineering. Accurate descriptions of macroscopic properties such as capillary pressures and relative permeabilities are necessary for numerical reservoir simulations of multi-phase flow [117]. These properties can be measured by costly laboratory experiments, or alternatively, physically-based models can be developed to predict multi-phase flow at the pore scale and estimate these macroscopic properties at the macro-scale [118].

To simulate multi-phase flow in porous media, an accurate pore space structure is required. This can be obtained from CT imaging [119] or 3D reconstructions [120]. Pore network modelling provides an effective tool for estimating macroscopic transport properties with arbitrary wetting conditions, making it an attractive option for numerical simulations of multi-phase flow. For more detailed information, readers are referred to the literature [45]. The appropriate model can be used by considering the existing flow regimes [121]. Two main types of network modelling tools are defined by the flow regime: capillary-dominated and viscous-dominated. In the case of a low capillary number [122, 123, 56], N_c , which is defined as, $N_c = \frac{\mu u}{\sigma} \leq 10^{-5}$ where μ is viscosity, u is fluid velocity and σ is interfacial tension, the viscous forces are insignificant and the flow is governed by capillary forces. In this case, quasi-static network modelling can be applied. Otherwise, dynamic network modelling should be used where both viscous and capillary forces are accounted for.

Developed dynamic pore network models

Dynamic pore network models have become a powerful tool for understanding fluid behavior in porous media, allowing for the capture of changing fluid properties and pore structure over time [124, 125, 126]. While previous dynamic pore network models have used explicit or semi-implicit approaches, these had limitations in accurately capturing

the complex behavior of the fluid flow. To overcome these limitations, researchers have developed new modeling approaches, such as fully implicit dynamic pore network models, which improve accuracy and provide greater insight into two-phase flow and phase change in porous media [127, 128].

The behavior of residual fluids in porous media is an important topic of study with a range of applications, including oil recovery, groundwater management, carbon sequestration, and energy storage. Dynamic pore network modeling has been used in several studies to investigate residual fluid behavior in porous media [129, 130, 131]. For instance, Li et al. [131] used dynamic pore network models to investigate the effect of heterogeneity on residual fluid configurations during the imbibition process. They found that heterogeneity significantly affects residual fluid configurations, and the spatial distribution of residual fluids is highly dependent on the degree of heterogeneity in the porous medium.

Chen et al. [127] presented a study that investigated various numerical modeling approaches and quantified their level of accuracy in dynamic pore-network modeling of two-phase flow and phase change in porous media. The study demonstrated the limitations of explicit and semi-implicit approaches and presented fully implicit approaches for dynamic pore network modeling.

Similarly, Weishaupt et al. [128] presented a dynamic pore network model that used a fully implicit approach to simulate two-phase flow in porous media. The authors validated their model using a synthetic porous media structure and demonstrated its ability to accurately simulate complex fluid flow behavior.

Overall, these new modeling approaches offer promising ways to more accurately simulate the behavior of two-phase flow in porous media and provide greater insight into the underlying physics of fluid flow. They have potential applications in a range of fields, including the oil and gas industry, environmental science, and materials science. For more information on the developed dynamic pore network models, please refer to Appendix I, which includes tables D.1-D.2.

The structure of the chapter is as follows. First, the methodology and simulation approach will be described. Then the numerical modelling results of the dynamic simulation for the hydrogen-brine system are reported in comparison with the quasi-static modelling and air-water systems. In the following section, the results of cyclic modelling by using experimentally measured contact angles for the hydrogen-brine system are shown. Finally, concluding remarks are presented.

5.2. METHODOLOGY

The following chapter aims to provide a summary of the methodology that has been used in DuMux which is an open-source simulator for flow and transport in porous media [128]. The readers for more detailed information are referred to this reference [132]. Additionally, Appendix E offers an overview of the Pore Network Modeling (PNM) approach and its formulations

5.2.1. DESCRIPTION OF THE PORE SPACE

In pore network modeling, the pore space refers to the empty space within a porous material where fluids can flow or be stored. It is the network of interconnected voids or pores that characterize the porous structure of a material, such as a rock, soil, or membrane.

The description of the pore space in pore network modeling involves characterizing the geometry, topology, and connectivity of the pores within the material. This can be done using various techniques, such as imaging [119], and statistical modeling [120]. The resulting data can then be used to construct an equivalent model of the pore network, which can be used to simulate fluid flow and transport processes within the material. The structure of the network data files is reported in appendix D.

The pore space can be characterized by several parameters, such as the pore size distribution, the tortuosity of the pores, and the connectivity of the network. These parameters can have a significant impact on the fluid flow behavior and transport properties of the material, such as absolute and relative permeability, and capillarity. The detailed information can be found in the literature [133, 134]

Therefore, an accurate and detailed description of the pore space is crucial for understanding the transport and storage behavior of porous materials and for optimizing their performance in various applications, such as oil and gas recovery, water filtration, and energy storage.

5.2.2. DISPLACEMENTS AND TRANSPORT PROPERTIES

In addition to characterizing the pore space, it is also important to understand the displacement and transport properties of fluids in porous media. Displacement refers to the movement of one fluid by another fluid in the pore space, and transport properties refer to the ability of fluids to move through the porous material.

Threshold capillary pressure

Threshold capillary pressure is an important parameter that affects displacement behavior in porous media. It is the minimum pressure required to initiate fluid displacement in a pore network. When fluid flows through a porous medium, the narrowest parts of the medium, known as pore throats, limit the rate of drainage. To pass through the throat, a minimum pressure, known as the entry capillary pressure, must be exceeded. This pressure is determined by the radius of curvature and the contact angle of the liquid as it recedes in the throat. This pressure is calculated using the radius of the inscribed pore throat (r_{ij}) and the contact angle of the receding meniscus (θ_r). If the throat cross-section is circular, $p_{c,e}$ can be easily calculated using a simple formula. However, for non-circular throats, the calculation of $p_{c,e}$ is more complex and depends on the presence of wetting layers in the corners of the throat.

The entry capillary pressure for circular throat cross-sections is given by

$$p_{c,e} = \frac{2\gamma \cos(\theta_r)}{r_{ij}}, \quad (5.1)$$

where γ is the surface tension, θ_r is the receding contact angle, and r_{ij} is the inscribed radius of the pore throat connecting pore bodies i and j .

For angular throat cross sections, wetting layers may be present in the corners of the throat only if a certain condition is met, i.e.,

$$\beta + \theta_r < \frac{\pi}{2}, \quad (5.2)$$

where β is the corner half angle. For a rectangular throat with $\beta = \frac{\pi}{4}$, for instance, this means that the wetting phase can only be present in the corner if $\theta_r \leq \frac{\pi}{4}$ to keep a positive capillary pressure, i.e., a concave arc meniscus. The capillary pressure within that layer reads

$$p_c = \frac{\gamma}{r_{am}}, \quad (5.3)$$

where r_{am} is the radius of the arc meniscus.

For the irregular throat cross-sections, the entry capillary pressure can be derived analytically using the Mayer-Stowe-Princen (MSP) method [135]. The MSP method considers an energy balance for displacing the wetting phase and equates the curvature of the arc meniscus with that of the invading fluid's terminal meniscus. Blunt [45] generalized this approach for arbitrary cross-sectional shapes, i.e.,

$$p_{c,e} = \frac{\gamma(1 + 2\sqrt{\pi G}) \cos(\theta_r) F_d(\theta_r, G)}{r_{ij}}, \quad (5.4)$$

where G is the shape factor (the ratio of area to the square of the perimeter) of the cross-section and

$$F_d(\theta_r, G) = \frac{1 + \sqrt{1 + 4GE/\cos^2(\theta_r)}}{1 + 2\sqrt{\pi G}}, \quad (5.5)$$

with

$$E = \pi - \frac{2}{3}\theta_r + 3 \sin(\theta_r) \cos(\theta_r) - \frac{\cos^2(\theta_r)}{4G}. \quad (5.6)$$

The snap-off capillary pressure, also known as the snap-off threshold, refers to the pressure required to cause the sudden disconnection or snap-off of a fluid phase in a porous medium. It is particularly relevant in the context of layer swelling, where the behavior of fluid phases in the porous medium is of interest. The snap-off capillary pressure can be calculated based on the geometry of the throats, which are narrow constrictions within the porous medium. Importantly, unlike other capillary pressure calculations, determining the snap-off capillary pressure does not require an energy balance analysis. This characteristic makes it a convenient parameter to study and analyze the behavior of fluids in porous media. For more detailed information on this topic, refer to the work by Blunt [45] and Appendix E.

Local capillary-pressure saturation relationship To accurately model pressure and saturation in pore-network models, a local capillary-pressure saturation relationship per pore body must be formulated. This relationship is often derived based on geometrical assumptions, as in the case of the cubic pore body i described by Joekar-Niasar et al. [134]. They proposed a simplified relationship for this cubic pore body where the local saturation $S_{w,i}$ is related to the capillary pressure $p_{c,i}$ via Equation (2.35), i.e.,

$$p_{c,i}(S_{w,i}) = \frac{2\gamma}{r_i(1 - \exp(-6.83S_{w,i}))}. \quad (5.7)$$

Meanwhile, a similar relationship for truncated octahedrons can be found in the work of Joekar-Niasar and Hassanizadeh (2012) [136].

Transport properties

Transport properties such as permeability and diffusivity are also critical in predicting fluid flow and transport in porous media. Permeability is a measure of how easily fluids can flow through a porous material, and diffusivity is a measure of how quickly a fluid can diffuse through the material. These properties can be influenced by the pore size distribution, connectivity, and tortuosity of the pore network [45, 132].

Estimation of the macroscopic fluid transport properties, including absolute permeability, relative permeabilities of each phase, and capillary pressure; can be done through the entire pore network.

Absolute permeability is determined by simulation of single-phase flow on the fully saturated network and solving Darcy's law, i.e.,

$$K = \frac{\mu_p Q_{total,sp} L}{A(\Phi_{inlet} - \Phi_{outlet})}, \quad (5.8)$$

where μ_p is the viscosity of a single-phase p , and L and A are the length and cross-sectional area of the network, respectively. Imposing a potential drop at two parallel surfaces of the network creates $Q_{total,sp}$; total flow rate. Therefore, the relative permeability of each phase can be calculated as

$$K_{rp} = \frac{Q_{tmp}}{Q_{tsp}}, \quad (5.9)$$

where Q_{tmp} is the flow rate of phase p in a multiphase flow.

To find the total flow rate, it is required to write mass conservation at each pore body i , i.e.,

$$\sum_j q_{p,ij} = 0, \quad (5.10)$$

where j is used to refer to all the pore throats connected to pore i . The basic assumptions are considering incompressible fluid and ignoring viscous pressure drops compared to the capillary pressure. The volumetric flow rate between the two pore bodies i and j is calculated by the Hagen-Poiseuille equation,

$$q_{p,ij} = \frac{g_{p,ij}}{L_{ij}} (\Phi_{p,i} - \Phi_{p,j}), \quad (5.11)$$

where L is the distance between the centers of the two connected pore bodies i and j .

Therefore, by solving a nonlinear set of mass conservation equations pore body pressures and saturation of phases can be calculated.

5.2.3. TWO-PHASE FLOW MODELLING

The two-phase flow in porous media can be modeled by a set of governing equations.

Quasi-static PNM

The quasi-static PNM assumes that it solves the equilibrium state of two-phase displacements given the global pressure difference across the domain, with no transient behavior involved. Quasi-static PNM models assume that the fluid within the pore space is stationary and there is no pressure gradient. This implies that a constant capillary pressure exists throughout the fluid-fluid interface, which corresponds to a globally applied capillary pressure. The capillary number is very low (10^{-5}). The system is in equilibrium at each time, so the global P_c equals the local P_c . Pressure and saturation can be solved separately (IMPES) since they are decoupled. Both pore-bodies and pore-throats have volumes. The models incrementally increase or decrease this global pressure difference to simulate drainage or imbibition processes, resulting in discrete saturation changes corresponding to equilibrium states. Since the fluid flow is not considered, only the critical threshold capillary pressures are relevant for quasi-static models. However, fluid configurations between the equilibrium states cannot be modeled. During drainage, the bonds of the network are filled based on the ascending order of the entry capillary pressures, under the constraint that only throats adjacent to already filled throats or the inlet of the domain may be invaded. In contrast, imbibition involves smaller pores and their neighboring throats being filled first. Quasi-static models have been used to predict rock properties such as capillary pressure-saturation curves, but they are limited to situations where equilibrium conditions can be assumed or capillary forces dominate the system. This is valid for low capillary numbers, where the ratio of dynamic viscosity and specific bulk flow rate of the invading phase to interfacial tension is small.

Dynamic PNM

Dynamic pore-network models take into account time-dependent phase displacement processes and can model non-equilibrium capillary pressure states while considering the fluid phases' viscosities. These models solve for pressure fields and phase fluxes based on mass or volume conservation, similar to conventional Darcy-type models. However, due to their highly non-linear behavior, dynamic models are computationally more complex and resource-intensive compared to quasi-static models [45]. The dynamic Pore-Network Model (PNM) solves the non-equilibrium state of two-phase flow in porous media. This means that transient behavior is involved. The pressure difference across the domain is not constant but varies over time due to fluid injection or withdrawal. Therefore, global pressure is not necessarily equal to local pressure at each time step.

Joekar-Niasar and Hassanizadeh [136] extensively reviewed the different solution strategies for dynamic two-phase pore-network models. They classified dynamic models into two general types:

1. The first type assigns a single pressure to each pore body, assuming either the exclusive presence of a single phase or the concept of an equivalent pressure that accounts for both phases [124, 137, 125]. While this approach reduces the computational complexity of the problem, Al-Gharbi and Blunt [125] found inconsistencies with respect to equivalent quasi-static simulation results for networks with angular cross-sections.

2. The second type of algorithm used in this study is based on the two-pressure model, initially introduced by Thompson [138]. This model aims to solve for an individual pressure field for each phase and adopts a sequential solution strategy that decouples the pressure and saturation variables to accelerate the solution of the linearized problems. It bears a resemblance to the IMPES (implicit pressure, explicit saturation) method commonly employed in reservoir models.

In the two-pressure model, the algorithm first solves the pressures for each phase. This decoupling enables a faster solution but necessitates the use of small time steps to maintain numerical stability during the explicit saturation update. Although the two-pressure model demonstrated limitations in accurately capturing quasi-static results and was found to be unsuitable for very low capillary numbers (Ca) [138], it provided valuable insights into the dynamics of multiphase flow in porous media.

To enhance the accuracy of the two-pressure model and address the highly non-linear nature of the processes, Joekar-Niasar et al. [139] proposed an improvement by introducing a semi-implicit saturation update. This enhancement allows for a better representation of complex multiphase flow behavior. Since then, this improved two-pressure model has been successfully applied in various studies [140, 141].

In the two-pressure model, the following equations govern the algorithm:

- (a) Conservation of mass for phase 1 (wetting phase)

$$\nabla \cdot (\rho_1 \mathbf{v}_1) = \frac{\partial}{\partial t} (\phi s_1 \rho_1) + \nabla \cdot (\phi s_1 \rho_1 \mathbf{v}_1)$$

- (b) Conservation of mass for phase 2 (non-wetting phase)

$$\nabla \cdot (\rho_2 \mathbf{v}_2) = \frac{\partial}{\partial t} (\phi s_2 \rho_2) + \nabla \cdot (\phi s_2 \rho_2 \mathbf{v}_2)$$

- (c) Darcy's law for phase 1 (wetting phase)

$$\mathbf{v}_1 = -\frac{k_{r1}}{\mu_1} (\nabla p_1 - \rho_1 g \nabla z)$$

- (d) Darcy's law for phase 2 (non-wetting phase)

$$\mathbf{v}_2 = -\frac{k_{r2}}{\mu_2} (\nabla p_2 - \rho_2 g \nabla z)$$

- (e) Capillary pressure-saturation relationship

$$p_c = p_1 - p_2$$

These equations capture the pressure and saturation evolution and provide a foundation for simulating flow behavior in porous media using the two-pressure model.

Highlight the physics/assumptions of quasi-static PNM

The quasi-static Pore Network Modeling (PNM) approach highlights several physics and assumptions regarding the equilibrium state of two-phase displacements. The method focuses on solving the equilibrium state, assuming negligible transient behavior and no time-dependent dynamics. It operates under the assumption of a very low capillary number (typically on the order of 10^{-5}), indicating that capillary forces dominate the fluid flow behavior while viscous forces have a minimal effect. In this approach, the system is considered to be in equilibrium at each time step, where the global capillary pressure (P_c) is assumed to be equal to the local capillary pressure. The pressure and saturation can be solved separately using the Implicit Pressure Explicit Saturation (IMPES) approach, as they are decoupled in the system. Additionally, both pore-bodies and pore-throats are considered to have volumes in this modeling approach.

Considering incompressible phases, mass conservation equations for the wetting and non-wetting phases read [132]:

$$V_i \frac{\partial S_i^w}{\partial t} + \sum_{j=1}^{N_i^j} Q_{ij}^w = Q_i^w, \quad (5.12)$$

$$V_i \frac{\partial S_i^n}{\partial t} + \sum_{j=1}^{N_i^j} Q_{ij}^n = Q_i^n, \quad (5.13)$$

where S_i^w and S_i^n represent the wetting and non-wetting phase saturations in pore i . V_i denotes the volume of pore i , while N_i^j represents the number of throats connected to pore i . Q_{ij}^w and Q_{ij}^n denote the flow rates of the wetting and non-wetting phases between pore i and throat j , respectively. Furthermore, Q_i^w and Q_i^n represent the total flow rates of the wetting and non-wetting phases in pore i , respectively. The relationship between the wetting and non-wetting phase saturations reads:

$$S_i^w + S_i^n = 0. \quad (5.14)$$

The capillary pressure, P_c , can be defined as the pressure difference between the wetting and non-wetting phases, i.e.,

$$P_i^w = P_i^n - P_i^w. \quad (5.15)$$

This system is well-posed with four equations for the four unknowns ($S_i^n, S_i^w, P_i^w, P_i^n$), incorporating local rules to calculate capillary pressure, entry pressure, snap-off mechanism, and conductance.

DuMux¹, an open-source simulator for flow and transport in porous media, provides a platform for simulating and studying these properties. By utilizing a pore network model, DuMux enables the simulation of fluid flow and transport in porous media, allowing for the exploration of various parameter impacts on fluid behavior within the pore space. For further details on the simulation methodology, refer to the references [128, 132].

¹DuMux: <https://dumux.org/>

Simulation approach:

The simulation approach for dynamic PNM is a fully implicit method, which is used when pressure and saturation are strongly coupled, such as in low capillary number flows or unfavorable displacements ($M < 1$). The sequential coupling employed by IMPES and IMP-SIMS can pose numerical challenges in such cases. A fully implicit method ensures numerical stability by treating the pressure and saturation equations simultaneously.

To solve the system of equations using a fully implicit method, numerical schemes such as Newton are used.

The fully implicit method enables the simultaneous solution of the pressure and saturation equations, enhancing numerical stability and capturing the strong coupling between pressure and saturation in low capillary number flows or unfavorable displacements.

5

5.3. RESULTS AND DISCUSSION

In this section, the transport of hydrogen through a network with box-shaped pores and square cylinder throats was studied using dynamic pore-network modeling. The network statistics are summarised in Table 5.1. The simulation results were compared with quasi-static pore-network modeling to assess the accuracy and reliability of the dynamic approach².

Table 5.1: The network statistics are adapted from [132].

Properties	values
Size (side length) [m]	1 E-3
Initial number. of pores	10 * 10 * 10
Probability deletion of the throat connections	90% for all spatial directions
pore radius distribution	log-normal
mean pore radius [m]	4.5 E-5
standard deviation [m]	3 E-6

The saturation of hydrogen-water in a randomly generated network is shown in Figure 5.1, which illustrates the distribution of hydrogen-water saturation throughout the network.

The average saturation of water in the network, denoted as $\langle S_w \rangle$, and the average capillary pressure, denoted as $\langle p_c \rangle$, were calculated using

$$\langle S_w \rangle = \frac{\sum_i (S_w V)_i}{\sum_i V_i} \quad (5.16)$$

$$\langle p_c \rangle = \frac{\sum_i (S_n p_n V)_i}{\sum_i (S_n V)_i} - \frac{\sum_i (S_w p_w V)_i}{\sum_i (S_w V)_i}. \quad (5.17)$$

²To replicate the results of this paper the source code can be accessed via this link <https://git.iws.uni-stuttgart.de/dumux-pub/weishaupt2020a> using the network information in Table 5.1 and the fluid and gas properties reported in Table 5.2

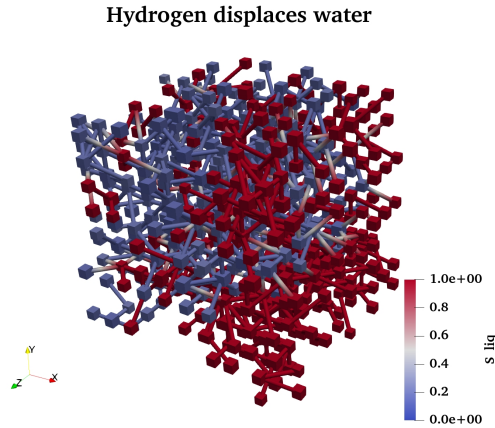


Figure 5.1: Saturation distribution of hydrogen-water in a randomly generated network. s_{liq} in the color bar depicts the saturation of water.

The results of the modelling have been listed as follows.

- The dynamic simulation of hydrogen-water transport was compared with the quasi-static simulation, as shown in Figure 5.2.

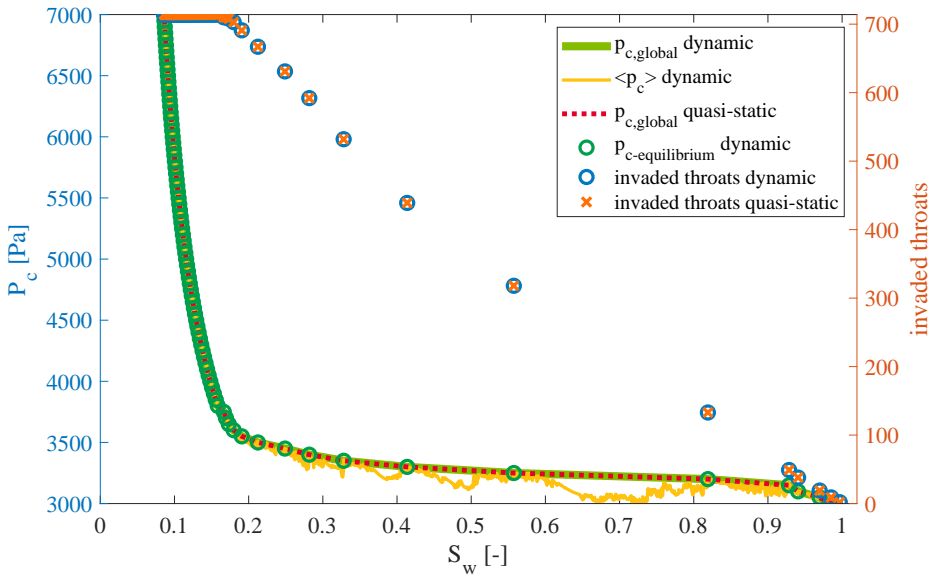


Figure 5.2: Hydrogen-water dynamic simulation compared with static simulation. The left vertical axis shows the capillary pressure and in the right vertical access number of invaded throats is shown.

The simulation results showed a good agreement between the dynamic and quasi-static modeling approaches. When the simulation reached steady-state, with no further changes in the saturation of the two phases, the saturation of hydrogen-water matched well between the dynamic and quasi-static simulations. This indicates that the quasi-static simulation can be used as a reliable and efficient method for studying hydrogen transport in similar networks.

- The capillary pressure function of hydrogen-water against air-water was also analyzed, and the results are presented in Figure 5.3.

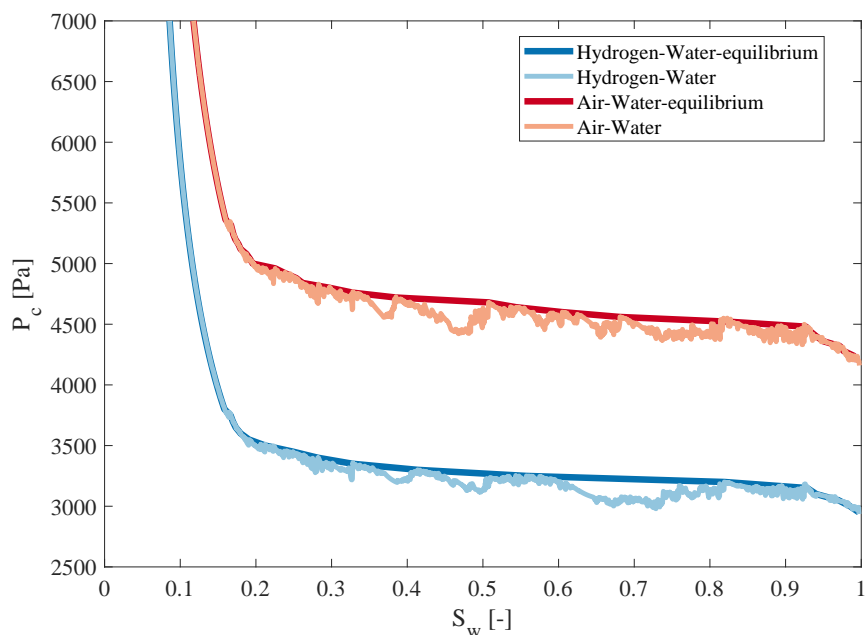


Figure 5.3: Capillary pressure function of hydrogen/water against air-water.

- The behavior of hydrogen-water in the network was analyzed by calculating the N_c and M values for drainage and imbibition processes. The relevant fluid properties and the calculated values are summarized in Table 5.2.

Table 5.2: H_2 -water and air-water properties used for N_c and M calculations.

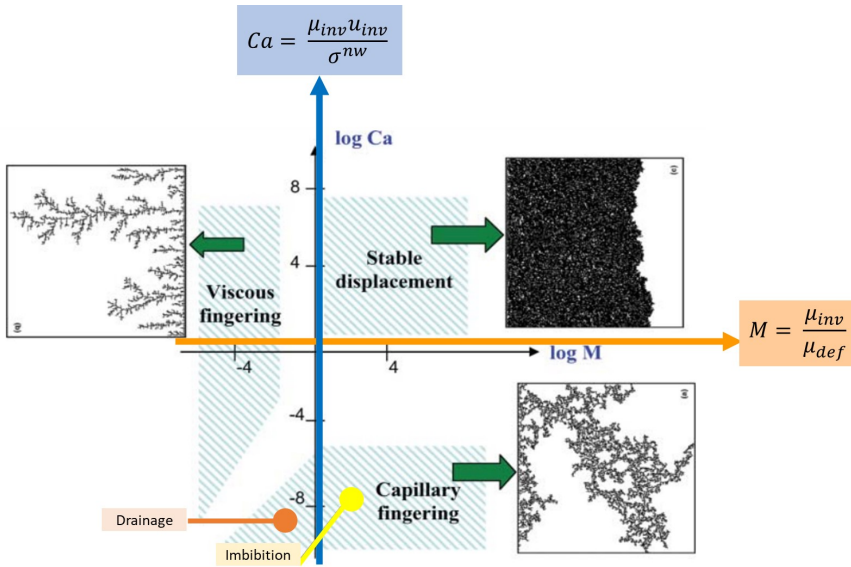
Fluid properties	Depth	IFT (mN/m)	Viscosity_ H_2 (Pa.s) * 10^6	Viscosity_ Brine (Pa.s) * 10^6
H_2 -Water [59]	50 bar, 20 °C	51	8.94	999
	100 bar, 45 °C	46	9.54	597
Air-Water [132]	atmospheric	72.5	17.68	1000

The N_c and M calculations for drainage and imbibition of H_2 -water, assuming a common velocity of 1ft/day in the field are shown in Table 5.3.

Table 5.3: Calculated N_c and M for drainage and imbibition for H_2 -water and air-water.

Fluid properties	Depth	Drainage				Imbibition			
		N_c	$\log(N_c)$	M	$\log(M)$	N_c	$\log(N_c)$	M	$\log(M)$
H_2 -Water [59]	50 bar, 20 °C	6.18E-10	-9.21	0.01	-2.05	6.910E-08	-7.16	111.74	2.05
	100 bar, 45 °C	7.32E-10	-9.14	0.02	-1.80	4.578E-08	-7.34	62.58	1.80
Air-Water [132]	atmospheric	8.60E-10	-9.07	0.02	-1.75	4.866E-08	-7.31	56.56	1.75

- Additionally, a modified Lenormand diagram (Figure 5.4) was used to illustrate the drainage and imbibition processes of hydrogen-water in the network. The diagram confirms that the system is still operating in the capillary-dominated regime, validating the use of the quasi-static pore network model.

Figure 5.4: Lenormand diagram with marked points for drainage and imbibition of H_2 -water with the mentioned assumptions. Modified after [139].

- In continuation of the previous point, the quasi-static pore network model was employed using contact angles determined for H_2 -Brine (Figure 5.6). A comparison was made with previously presented P_c and K_r values obtained using different contact angles (Figure 5.5), as reported in our previous paper [35]. The static contact angle was determined through captive bubble experiments [63], while the dynamic contact angles were measured using microfluidics experiments [100]. Both methods yielded intrinsic contact angles ranging from 25 to 45 degrees. The new results highlight a significant difference when direct contact angle measurements from the experimental work are utilized. This discrepancy is manifested in two main observations: firstly, a higher residual hydrogen saturation during production (secondary imbibition) compared to our previous paper [35], and secondly,

a higher relative permeability of water. These differences align with a lower gas-water contact angle and indicate a shift towards a more water-wet system.

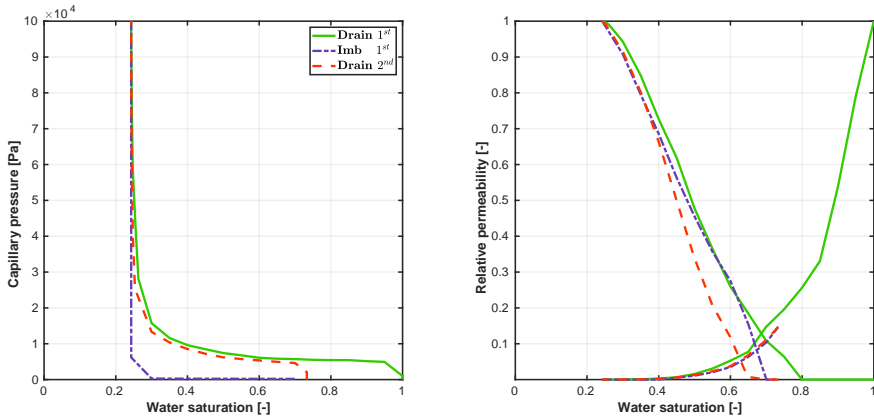


Figure 5.5: Basecase simulation using Berea PNM reported in [35].

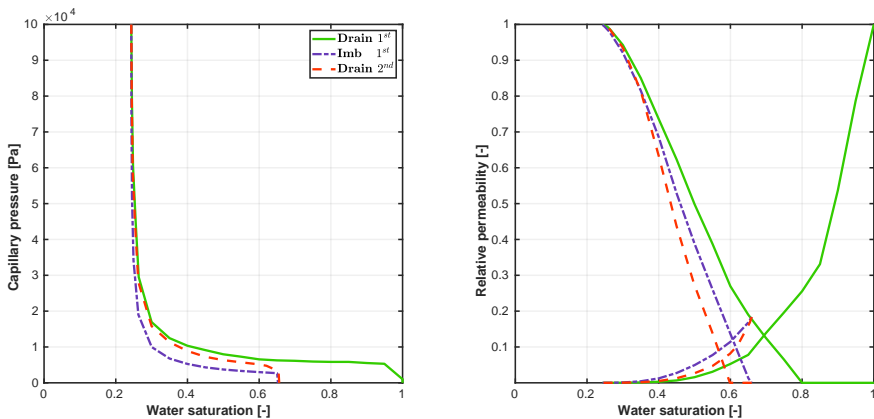


Figure 5.6: Basecase simulation using Berea PNM and reported contact angles in [63].

By utilizing the modified Lenormand diagram, the capillary-dominated regime of the system is reaffirmed, thereby supporting the use of the quasi-static pore network model. Furthermore, investigating the model with contact angles determined for H₂-Brine and comparing the results with previous findings reveals significant variations when different contact angle measurement methods are employed. These additions contribute to a comprehensive understanding of the behavior of hydrogen-water in the network and emphasize the importance of accurate contact angle measurements in simulations.

5.3.1. DISCUSSION

The results obtained from both dynamic and quasi-static pore-network modeling demonstrate a good match, suggesting that the use of quasi-static simulation is acceptable for hydrogen-water systems with smaller interfacial tension (IFT) values compared to air-water. This finding strengthens the validity of using quasi-static modeling to capture the behavior of hydrogen-water in terms of the upscaled parameters of the Pc-Sw curve.

However, it is important to note that flow regimes based on the Lenormand diagram were conducted under the assumption of a common velocity in the field, which is a simplified representation that may not accurately reflect the complex flow patterns found in reality. As a suggestion for future work, it would be beneficial to relax this assumption and incorporate more realistic velocity fields into the modeling approach to gain a better understanding of the system dynamics.

Furthermore, the simulation utilized box-shaped pores and square cylinder throats, which may not capture the full range of pore and throat geometries encountered in real porous media. To enhance the generality of the model, it would be valuable to explore different pore and throat shapes and develop more generalized local rules that can accommodate various pore geometries.

Another limitation of the current simulation is the assumption of a non-zero contact angle. Incorporating contact angles into the simulation could provide more accurate results, as contact angles significantly influence fluid-fluid interactions at the pore scale. By considering contact angles, a more comprehensive understanding of the hydrogen-water system can be achieved.

Additionally, it is worth noting that the simulation only accounted for one cycle of displacement. Conducting simulations for multiple cycles of displacements would provide insights into the hysteresis phenomena associated with the hydrogen-water system, allowing for a more thorough investigation of the fluid displacement behavior and the impact of repeated cycles on the system.

Finally, the efficiency and scalability of the solver used for dynamic pore-network modeling are crucial considerations. Future research could explore strategies to improve the efficiency of the simulation without compromising accuracy, ensuring that large-scale simulations can be performed within reasonable timeframes. Additionally, scaling considerations should be taken into account to accurately represent field-scale conditions in the pore-network model.

Addressing these limitations and conducting further investigations based on the suggestions outlined above would enhance the understanding of the hydrogen-water system and contribute to the development of more robust and accurate simulation approaches for analyzing its behavior in porous media.

5.4. CONCLUSIONS AND RECOMMENDATIONS

5.4.1. CONCLUSIONS

The study conducted a critical assessment of the validity of quasi-static pore network modeling (PNM) in the context of underground hydrogen storage. The results and discussions provided insights into the application of dynamic simulation in comparison to quasi-static PNM. The dynamic simulation results for the hydrogen-water system ex-

hibited good agreement with the quasi-static PNM results, for capillary number $\leq 10^{-7}$ indicating that dynamic PNM is a valid approach for simulating hydrogen transport in these networks, as long as it reaches a steady-state. The study also revealed that quasi-static simulation is acceptable for smaller interfacial tension (IFT) values compared to air-water, considering the upscaled parameters of the Pc-Sw curve.

Furthermore, the study identified several areas that require further research to enhance the validity of quasi-static PNM for hydrogen storage applications. These areas include exploring the scaling and size of the network, investigating different mechanisms, incorporating various pore and throat shapes, developing general local rules for different pore shapes, considering the influence of contact angles, and simulating additional cycles of displacements. Addressing these aspects will contribute to refining the accuracy and reliability of quasi-static PNM in simulating hydrogen storage systems.

Overall, the study emphasizes the importance of critically assessing modeling approaches to ensure the validity of simulation results in real-world applications like underground hydrogen storage.

5

5.4.2. RECOMMENDATIONS

Based on the findings and discussions, the study puts forward the following recommendations for further research:

1. Scale and size of the network: Investigate the impact of network scale and size on the simulation results to determine their influence on the accuracy and applicability of quasi-static PNM.
2. Transport mechanisms: Explore and incorporate additional mechanisms into the PNM model to capture more complex physical phenomena and improve the representation of the hydrogen storage system.
3. Pore and throat shapes: Consider different pore and throat shapes to account for the geometric variations commonly encountered in real-world porous media.
4. General local transport rules: Develop general local rules that can be applied to different pore shapes, enhancing the versatility and robustness of the quasi-static PNM approach.
5. Contact angles: Include the effect of contact angles in the simulation to better understand the impact of wettability on the behavior of the hydrogen storage system.
6. Cycles of displacements: Simulate multiple cycles of displacements to study the system's response and evaluate the long-term performance and stability of the hydrogen storage process.

In addition, to have a well-specified dynamic pore network model (D-PNM) specifically for hydrogen, the following aspects should be considered:

- Cyclicity: Incorporate cyclicity in the simulation to capture the saturation history and accurately represent the cyclic behavior of hydrogen transport.

- High viscosity and density contrast: Account for the high viscosity and density contrast between hydrogen and other fluids in the system to ensure realistic modeling of the flow dynamics.
- Compressibility: Incorporate compressibility effects in the model to accurately represent the behavior of the hydrogen phase under changing pressure conditions.
- Non-zero contact angle: Include non-zero contact angles in the simulation to account for the influence of wettability on the flow and displacement processes in the hydrogen storage system.
- Solver efficiency: Develop efficient and robust solvers tailored for D-PNM to enable accurate and timely simulations of hydrogen transport.
- Scale in terms of time and length: Consider the appropriate time and length scales in the simulation to ensure the model's applicability to real-world hydrogen storage scenarios.
- Reactivity under microbial activities: The impact of bio-geo chemistry of hydrogen transport needs to be investigated.

These recommendations aim to enhance the understanding and predictive capabilities of PNM modeling for hydrogen storage systems, ultimately advancing the development and implementation of underground hydrogen storage technologies.

6

CONCLUSIONS AND FUTURE WORK

The first part of the research focused on quantifying H₂-brine transport properties at the continuum scale using pore network modeling (PNM). Through systematic studies and benchmarking with existing experimental data, the research established a meaningful base case configuration. The results indicated that brine tends to occupy smaller regions of the pore space, leading to higher exponents in the power-law type empirical model for relative permeability compared to the non-wetting hydrogen phase. The study also highlighted the importance of considering hysteresis for both hydrogen and brine in cyclic hydrogen storage, emphasizing its impact on capillary pressure and relative permeability. Sensitivity analyses demonstrated the significance of contact angles and pore structure in determining multiphase flow properties. Additionally, variations in clay percentages and coordination numbers were found to affect drainage and imbibition cycles and the residual saturation of the non-wetting phase. These findings provide a baseline for further research on H₂ transport properties and emphasize the need for additional laboratory investigations.

In the second part of the research, contact angles for H₂-CH₄ mixtures, pure H₂, and pure CH₄ in contact with brine and Bentheimer sandstone rock were measured using the captive-bubble cell device. The experiments showed strongly water-wet conditions, with contact angles ranging between 25° and 45° for all gas mixtures. Contact angles were observed to increase with decreasing bubble volume. The sensitivity analysis, based on the Young-Laplace equation, validated the experimental results by demonstrating that changes in contact angle fell within the accuracy range of the experiment. The analysis further showed that hydrogen, methane, and their mixtures exhibit comparable wettability characteristics under the influence of buoyancy and capillary forces. This finding suggests that these gases would display similar wettability in real-field processes.

In the final part of the research, the validity of quasi-static PNM in the context of underground hydrogen storage was critically assessed. The dynamic simulation results for the hydrogen-water system matched well with the quasi-static PNM results, indicating that dynamic PNM is a valid approach as long as it reaches a steady state. The study recommended further research in areas such as network scaling, pore/throat shapes,

general local rules for different pore shapes, contact angles, and simulating additional cycles of displacements. Addressing these areas would enhance the validity of quasi-static PNM for hydrogen storage applications.

In conclusion, this research provides valuable insights into H₂ transport properties in porous media for underground hydrogen storage. The findings emphasize the significance of PNM in characterizing multiphase flow behavior, the influence of contact angles and pore structure, and the applicability of quasi-static and dynamic modeling approaches. The recommendations for further research highlight the need for continued investigation into various parameters and modeling considerations to improve the accuracy and reliability of simulations in real-world applications.

Therefore it can be summarized in the following points:

- **Validating the Quasi-Static Pore Network Model (PNM):**
Through the use of a quasi-static Pore Network Model (PNM), this research successfully explored the behavior of underground hydrogen storage (UHS) in porous media. Despite the limitations of PNM, the results obtained demonstrated its effectiveness in capturing essential features of the system and providing valuable insights into the flow and transport processes. This highlights the utility of PNM as a practical and efficient tool for studying UHS.
- **Addressing Data Limitations:**
The research identified a critical data gap concerning the H₂-brine system, necessitating the measurement of the contact angle between hydrogen and brine. Collaboration with other researchers allowed for the acquisition of crucial data using captive bubble and microfluidic setups. These measurements significantly enhanced the understanding of the system and provided valuable input parameters for the PNM simulations, ultimately improving the accuracy of the modeling results.
- **Exploring Dynamic Pore Network Modeling:**
Collaboration with the DuMux group in Stuttgart provided an opportunity to investigate the effects of time and dynamics in UHS using a dynamic Pore Network Model. Although the findings did not yield significant deviations compared to the quasi-static approach, this research contributes to the growing body of knowledge regarding dynamic modeling in UHS. It highlights the potential for further investigations into the dynamic behavior of hydrogen storage systems and encourages future researchers to explore this area.

Recommendations for Future Research:

Building upon the insights gained and acknowledging the limitations encountered, several recommendations for future research in the field of UHS can be made. These include:

- Further investigation of alternative modeling approaches beyond the Pore Network Models, such as direct numerical simulations (DNS) or lattice Boltzmann methods, to capture finer details and overcome some limitations of PNM.

- More extensive experimental measurements and characterization of the H₂-brine system, including contact angles and other relevant parameters, to enhance the accuracy and reliability of the models.
- Exploration of dynamic effects and time-dependent behavior in UHS, particularly in terms of pore-scale phenomena, such as flow dynamics, adsorption/desorption kinetics, and capillary forces, to provide a more comprehensive understanding of the system.
- Bio-geochemistry is a crucial aspect to be examined further within the realm of UHS, that requires additional research and exploration.

In summary, despite the limitations and challenges faced, this research contributes to the field of UHS by demonstrating the effectiveness of quasi-static Pore Network Modeling, addressing data limitations, exploring dynamic modeling approaches, and providing valuable recommendations for future research.

A

OVERVIEW OF UHS PROJECTS AND SIMULATION DATA

Table A.1: Research projects related to UHS [22, 12].

Name of project	Description
H2STORE	<p>Duration: started in 2012 [12]</p> <p>Contributed country: Germany [12]</p> <p>Participant(s): the German Federal Ministry of Education and Research (R&D program of Energy Storing), Coordinator: FSU Jena. Partnerships: TU Clausthal, EFZN, GFZ Helmholtz-Centre Potsdam, and LEMTA-University of Lorraine, Nancy [12]</p> <p>Note: This project was related to geo-hydraulic, mineralogical, geochemical and biogenic reactions, by focusing UHS in depleted gas reservoirs, meanwhile aquifers were the other option for storing [12]</p>
InSpEE	<p>Duration: started in 2012 [12]</p> <p>Contributed country: Germany [12]</p> <p>Participant(s): the German Federal Ministry of Education and Research (R&D program of Energy Storing), Coordinator: KBB Underground Technologies. Partnerships: BGR (Federal Institute for Geosciences and Natural Resources); The Leibniz University of Hannover [12]</p> <p>Note: "Informational Systems in Salt Structures" was related to intelligent computer-assisted control of storage behavior [12]</p>
HyUnder	<p>Duration: 2012 - 2014 [12]</p> <p>Contributed country: EU (Germany, Netherlands, Romania) [12]</p> <p>Participant(s): CENEX (Centre of Excellence of Low Carbon and Fuel Cell Technologies), CEA (Commissariat à l'Energie atomique et aux énergies alternatives), DEEP Underground Engineering, ECN (The Energy Research Centre of the Netherlands), E.ON Gas Storage, HINICIO, LBST (Ludwig Bolkow Systemtechnik), KBB Underground Technologies, HYRO (National Hydrogen and Fuel Cell Centre from Romania), and Shell Global Solutions International B.V., Solvay [12].</p> <p>Note: This was the first European R&D project about UHS by focusing on engineering and economic aspects [12].</p>
Hychio	<p>Duration: started in 2006 till present [22]</p> <p>Contributed country: Argentina [22]</p> <p>Participant(s): Argentina [22]</p> <p>Note: This was one of the first field test of UHS in depleted gas reservoirs. So, its pilot started in 2009 and received hydrogen from the electrolyzing of water. Then pure hydrogen is combined with natural gas and by combusting that, the energy is produced again. In addition, another product of electrolyse, Oxygen is sold to the gas market. This project has been working successfully so far [22].</p>
ANGUS+	<p>Duration: started in the mid of 2013 and finished in 2015 [22]</p> <p>Contributed country: Germany [12]</p> <p>Participant(s): the German Federal Ministry of Education and Research (R&D program of Energy Storing), Coordinators: Christian-Albrechts University of Kiel. Partnerships: Deutsches Helmholtz GeoForschungs Zentrum (GFZ), and Helmholtz Centre for Environmental Research-UFZ; Ruhr-University Bochum [12] [22]</p> <p>Note: The main concern of this project is developing mathematical modeling of underground storage by using existing models and approaches, risk assessment techniques, and experimental investigations related to chemical and microbial aspects of thermal storage [12]. Moreover, this project also included the feasibility study of storing natural gas, synthetic methane, hydrogen and compressed air in caverns and porous reservoirs and considered economic, political, and legal aspects, as well [22].</p>
Underground Sun Storage	<p>Duration: started in 2012 [12] [22]</p> <p>Contributed country: Austria [12]</p> <p>Participant(s): coordinated by RAG (Rohol-Aufsuchungs Aktiengesellschaft). Other members of the consortium are the University of Leoben (the Department for Agrobiotechnology), IFA-Tulln of the University of Natural Resources and Applied Life Sciences, Vienna; the Energy Institute at the Johannes Kepler University Linz; Verbund; and Axiom Angewandte Prozesstechnik GmbH [12]</p> <p>Note: This a feasibility study of storing natural gas or synthesized methane with hydrogen in underground porous reservoirs with regarding the engineering, economic, and material characteristic issues of UHS. It has been conducted for implementing a field test of one storage cycle of the gas mixture containing 10% hydrogen [22]</p>

Table A.2: Research projects related to UHS [22, 12], continued.

Name of project	Description
HyINTEGER	<p>Duration: started in January 2016 till 2019 [22]</p> <p>Contributed country: Germany [12] [22]</p> <p>Participant(s): the German Federal Ministry of Education and Research (R&D program of Energy Storing), Coordinator: FSU Jena. Partnerships: TU Clausthal, EFZN, GFZ Helmholtz-Centre Potsdam, LEMTA-University of Lorraine, Nancy, and the University of Mainz [12] [22]</p> <p>Note: This is the follow-up H2STORE project, so by implementing some experimental tests and numerical simulations and developing analytical methods, assessed the chemical-mineralogical, microbiological and petrophysical-geohydraulic-geomechanical processes in reservoir and cap rocks, and the material behavior under the corrosive conditions [22]</p>
A French research project	<p>Duration: started in 2011 [12]</p> <p>Contributed country: Franc [12]</p> <p>Participant(s): the University of Lorraine and the Carnot Institute ICEEL [12]</p> <p>Note: "Self-organization phenomena in bio reactive multi-component transport through porous media: application to Underground Storage of Hydrogen." [12]</p>
Roads2HyCOM	<p>Participant(s): founded by the European Commission [12]</p> <p>Note: this is a program for large-scale hydrogen storage in geological formations [12]</p>
HyLighths	<p>Participant(s): founded by the European Commission [12]</p> <p>Note: this is a program for large-scale hydrogen storage in geological formations [12]</p>
US research	<p>Contributed country: US</p> <p>Participant(s): the Sandia National Lab on behalf of the Department of State for Energy in the United States [12]</p> <p>Note: feasibility studies of UHS in geological formations [12]</p>
ADMIRE	<p>Contributed country: Netherlands</p> <p>Participant(s): Delft University of Technology, Civil Engineering and Geosciences Faculty [10]</p> <p>Note: ADMIRE stands for Adaptive Dynamic Multiscale Integrated Reservoir-Earth, that studies different aspects of UHS, i.e., hydrodynamics, geomechanics [10, 35, 142, 32]</p>

Table A.3: Solubility values of hydrogen in brine.

No.	Solubility	Temperature	Pressure	Brine Composition	Reference(s)
1	[0-4] mol/m ³	[0-700] °F	[0-700] psia	pure water	[24]
2	80 mol/m ³	25 °C	100 bar	pure water	[11]
3	0.784 mol/m ³	25 °C	1 atm	pure water	[11]
4	37 mol/m ³	30 °C	50 bar	pure water	[11]
5	[0.001-0.002] g/kg	[0-100] °F	1 bar	pure water	[11, 143]
6	[6-10] × 10 ⁻⁴ mol/kg	[0-30] °C	1 bar	pure water & 4% NaCl	[11, 144]
7	7.9 × 10 ⁻⁴ mol/kg	25 °C	1 atm	pure water	[25]

Table A.4: Diffusivity values of hydrogen into different brine.

No.	Diffusivity (m^2/s)	Hydrogen into	Reference(s)
1	5×10^{-9}	pure water	[12, 25]
	3×10^{-11}	clay	
2	10^{-9}	pure water	[15]
	10^{-11}	water soaked argillaceous	
3	4.5×10^{-9}	pure water	[11]
	3×10^{-11}	clay	
4	1.6×10^{-9}	liquid	[24]

Table A.5: Receding and advancing contact angles by digitizing Morrow's graph. * indicates modified values for advancing contact angles which were used in this paper.

θ_i	θ_r	θ_a	modified θ_a^*
22	0	0	0
32	1	20	20
42	2	40	40
51	5	58	58
62	10	81	81
70	15	96	85
75	20	107	85
79	25	115	85
83	30	122	85
86	35	128	85
89	40	134	85
94	50	144	
99	60	153	
103	70	159	
109	80	163	
113	90	167	
118	100	171	
124	110	173	
128	120	175	
133	130	177	
138	140	178	
143	150	179	
148	160	179	
153	170	180	
159	180	180	

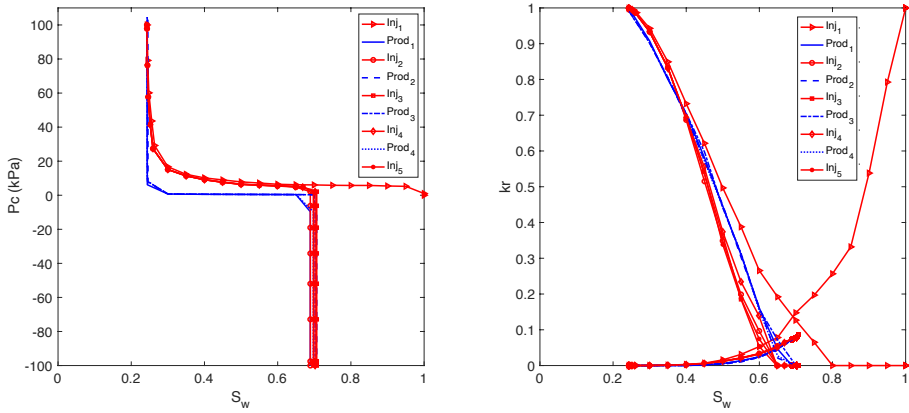


Figure A.1: The impact of cyclic transport dynamics on capillary pressure and relative permeabilities for 9 cycles of injection and production of hydrogen into the network of Berea sandstone with advancing and receding contact angles of $\theta_a = 81^\circ$ and $\theta_r = 10^\circ$, respectively, using the fluid properties of the base-case.

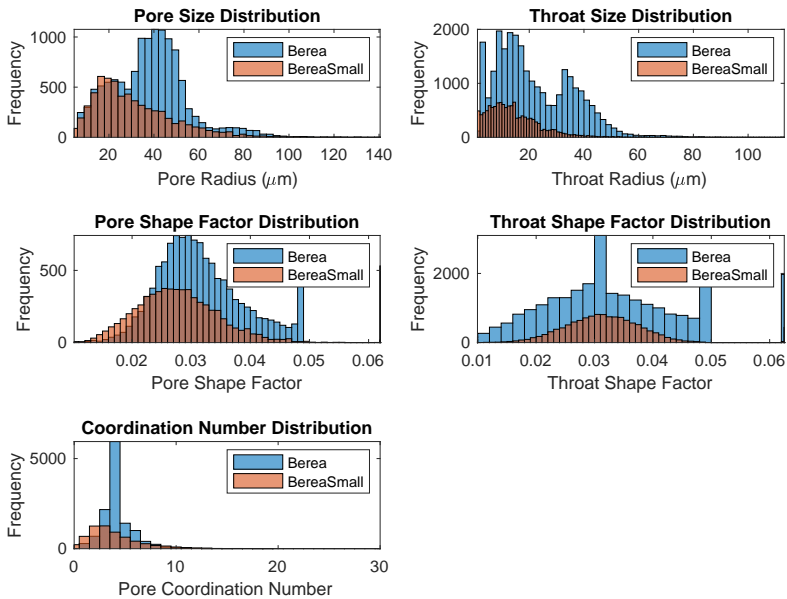


Figure A.2: Pore network characteristics for Berea and small Berea.

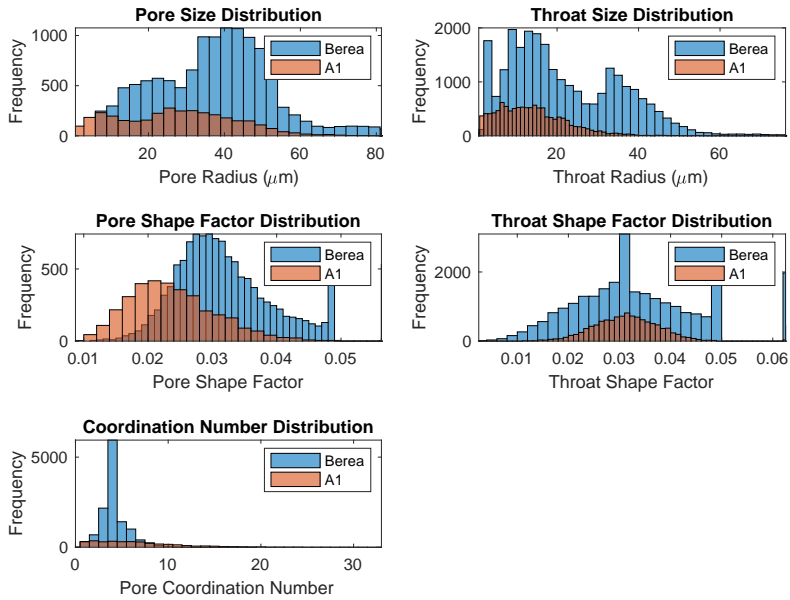


Figure A.3: Pore network characteristics for Berea and A1.

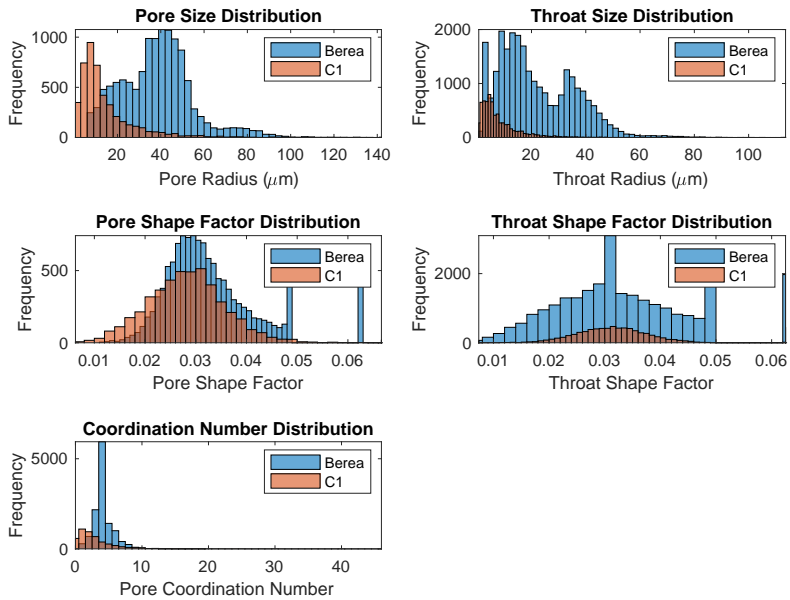


Figure A.4: Pore network characteristics for Berea and C1.

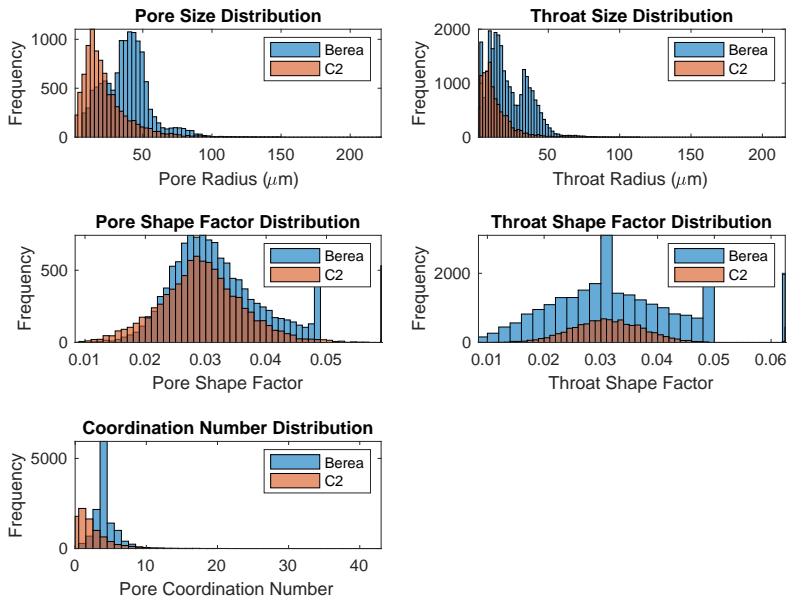


Figure A.5: Pore network characteristics for Berea and C2.

Table A.6: Used fluid and rock properties for clay volume (H_2 -Brine) sensitivity analysis. * indicates the network that was used as the base-case of simulations, in all cases there are 10,000 pores, 28700 throats, and porosity of 20.78, and a permeability of 134.96 mD.

Rock	Test No.	Clay (%)			Dimensions (mm ³)	
	1*	0			$3.47 \times 1.39 \times 0.69$	
2	10			$3.47 \times 1.39 \times 0.69$		
3	20			$3.47 \times 1.39 \times 0.69$		
4	30			$3.47 \times 1.39 \times 0.69$		
5	40			$3.47 \times 1.39 \times 0.69$		
6	50			$3.47 \times 1.39 \times 0.69$		
Fluid	Phases	$\sigma_{H_2,brine}$ (mN/m)	θ_r (degrees)	θ_a (degrees)	Viscosity ratio	Density difference (kg/m ³)
	H2-Brine	51	21.56	85	111.745	994.9

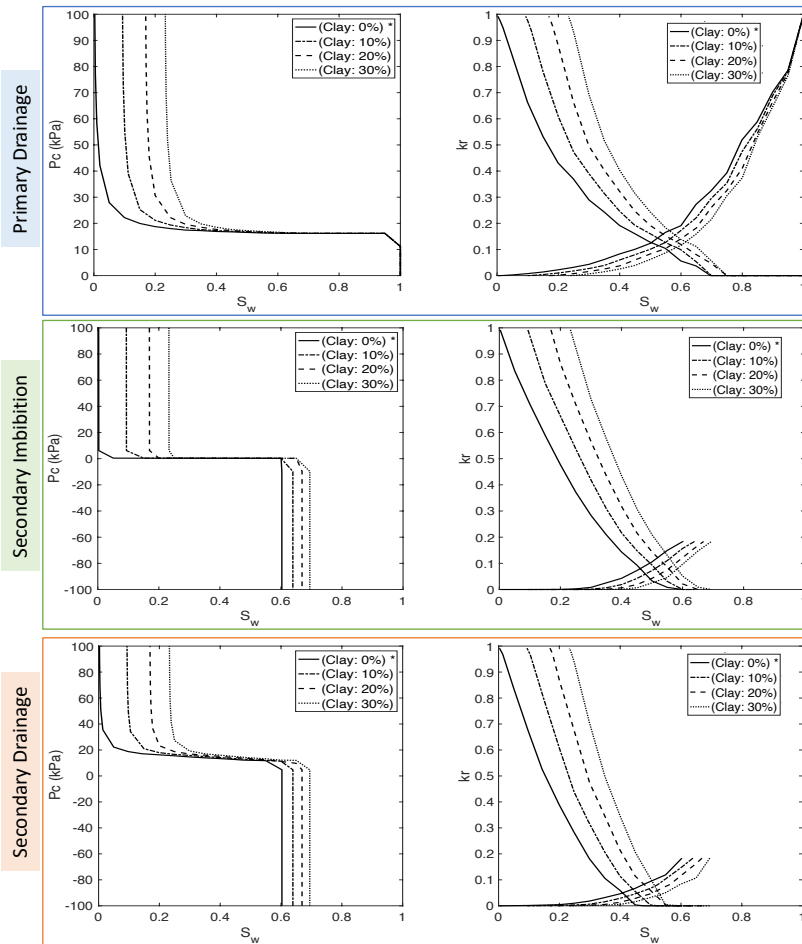


Figure A.6: Sensitivity analysis of H_2 -brine system on clay volume. * indicates the statistical network that was used as the base-case of simulations.

Table A.7: Used fluid and rock properties for coordination number(H₂-Brine) sensitivity analysis. * indicates the network that was used as the base-case of simulations.

Rock	Test No.	Coordination No. (average)	Dimensions (mm ³)	No. of pores	No. of throats	Porosity (%)	Permeability (mD)
	1*	6	3.46 × 1.39 × 0.69	10000	28700	20.57	135.52
	2	5	3.47 × 1.39 × 0.69	10000	23936	18.62	77.03
	3	4	3.45 × 1.38 × 0.69	10000	19302	15.56	30.82
	4	3	3.47 × 1.39 × 0.69	10000	14794	14.56	8.35
Fluid	Phases	$\sigma_{H_2,brine}$ (mN/m)	θ_r (degrees)	θ_a (degrees)	Viscosity ratio	Density difference (kg/m ³)	
	H ₂ -brine	51	21.56	85	111.745	994.9	

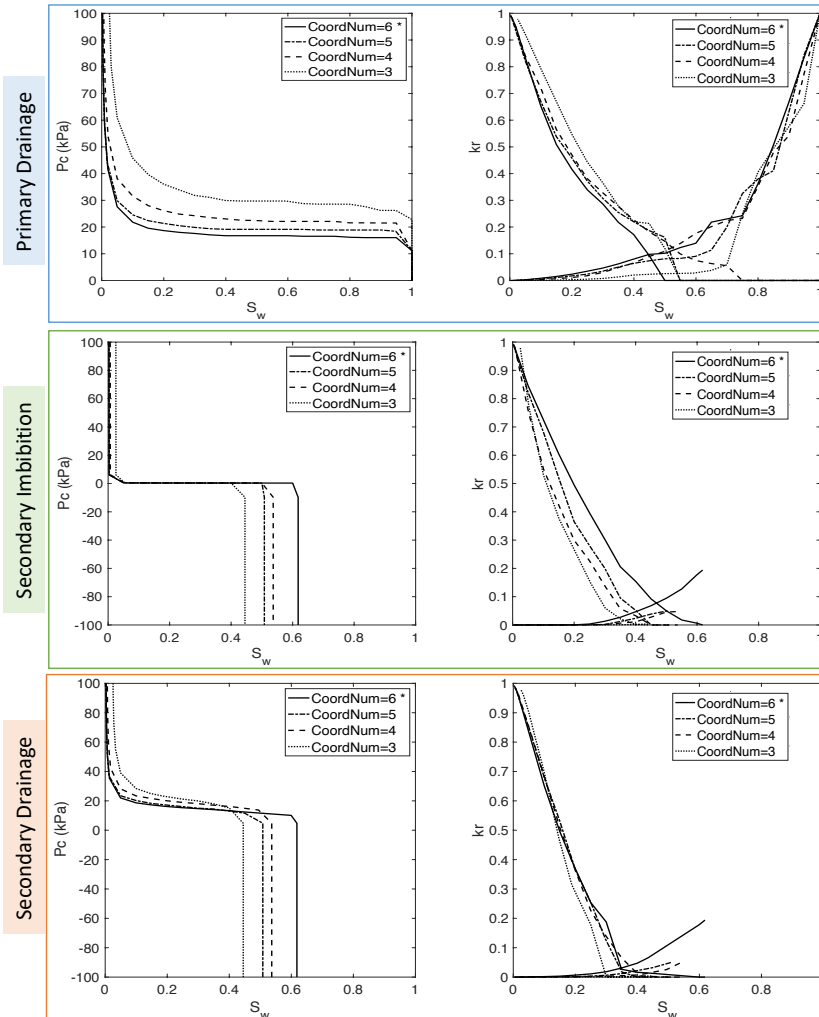


Figure A.7: Sensitivity analysis of H₂-brine system on coordination number. * indicates the statistical network that was used as the base-case of simulations.

B

CONTACT ANGLE MEASUREMENTS FOR H₂-BRINE

Table B.1: Review of literature experimental measurement of contact angles for systems containing Gas/Brine/Rock.

Reference	Substrate	Fluids	Gases	Method	P & T conditions	Comments	Wettability
Yang et al., 2008 [145]	Carbonate Weyburn limestone	Weyburn brine	CO ₂	Sessile-Drop ADSA	0.1-31.6 MPa; 300 & 331 K	θ increases with P θ decreases with T limestone	intermediate wet 27°C (45-100) ^o 58°C (88-135) ^o
Espinosa et al., 2010 [145]	Carbonate, Calcite Sandstone, Quartz, oil-wet Quartz PTFE	water, NaCl, 200 g/l	CO ₂	Sessile-Drop ADSA	up to 20 MPa; 298 K	θ increases with P on nonwetting surfaces: PTFE & oil-wet Quartz θ slightly decreases in water-wet Quartz & Calcite surfaces θ increases with salinity	strongly water-wet Calcite: 20° Quartz: 20° Oil-wet Quartz: 85-90° PTFE: 100-140°
Bikkina, 2011 [145]	Carbonate, Calcite; Sandstone, Quartz	water	CO ₂	Sessile-Drop	1.3-21 MPa; 298-323 K	θ increases with P slightly then decreases slightly and remains fairly constant	weakly water-wet
Mills et al., 2011 [146]	Carbonate, Calcite Sandstone, Quartz Biotite Orthoclase Labradorite	Brine	CO ₂ N ₂	Captive-Bubble	6 MPa & 295 K; 13 MPa & 313 K	θ increases with P slightly	strongly water-wet
Broseta et al., 2012 [147]	Carbonate Calcite Rousse caprock (70% Calcite)	NaCl, 4g/l NaCl, 4g/l, 40g/l, 350g/l	CO ₂ CO ₂	Captive-Bubble	0.5-14 MPa; 308 K 1.1-15.5 MPa; 3.8-413 K	θ increases with P θ increases with P θ remains constant with P θ increases with salinity	weakly water-wet strongly to weakly water-wet
Jung et al., 2012 [82]	Sandstone Silica	water, brine 5M	CO ₂	Captive-Bubble; Sessile-Drop; No difference in results	0.1-25 MPa & 318 K; 20 MPa & 323 K	7-10 MPa, after 10 MPa θ remains constant θ increases with salinity linearly	strongly water-wet
Wang et al., 2012 [148]	Carbonate Calcite	water, Synthetic brines	CO ₂	Captive-Bubble	7 MPa & 303 K; 20 MPa & 323 K	θ increases with P slightly θ decreases with salinity	strongly water-wet

Table B.2: Review of literature experimental measurement of contact angles for systems containing Gas/Brine/Rock (continue).

Reference	Substrate	Fluids	Gases	Method	P & T conditions	Comments	Wettability
Farokhpoor et al., 2013 [149]	Carbonate Calcite	water, NaCl, 0.2 & 0.8 M	CO ₂	Captive-Bubble	0.1-40 MPa; 309 K	θ increases with P on Mica for the rest not significant changes θ increases with T on Quartz	strongly water-wet
	Sandstone Quartz feldspar Mica						
Kaveh et al., 2014 [76]	Sandstone Bentheimer Carbonate	water	CO ₂ CO ₂ +N ₂	Captive-Bubble ADSA	0.2-15 MPa; 318 K	not significant changes with P	water-wet
Andrew et al., 2014 [150]	Ketton limestone (99% Calcite)	KI, 7 wt%	CO ₂	Pore-Scale microCT	10 MPa; 323 K		weakly water-wet
Al-Yaseri et al., 2015 [80]	Sandstone Quartz	water, NaCl, 0.5 wt%	CO ₂ N ₂ CO ₂ +N ₂	Sessile-Drop	13 MPa; 333 K		47° 40.6° 33.9°
Arif et al., 2017 [151]	Carbonate Calcite	water, NaCl, 0-20 wt%	CO ₂	Tilting-Plate	0.1-20 MPa; 308-343 K	θ increases with P & salinity θ decreases with T & roughness [151]	strongly to weakly water-wet
Stevan et al., 2019 [152]	Carbonate Calcite	NaHCO ₃ (aq), 1 mol/kg	CO ₂	Sessile-Drop Tilting plate	up to 30 MPa; 298-373 K	θ increases up to 10 MPa, after 10 MPa θ decreases, and being constant θ decreases with T & roughness	water-wet intermediate-wet
Haeri et al., 2020 [81]	Sandstone Navajo Nugget Bentheimer Bandera Brown Berea Mt. Simon	NaHCO ₃ (aq), 1 mol/kg	CO ₂	Captive-Bubble		No clear trend with P & T	strongly to weakly water-wet
Iglauer et al., 2020 [64]	Sandstone Quartz aged Quartz, in acid	NaCl, 10 wt%	H ₂	Sessil-Drop Tilting plate	0.1-25 MPa, 296-343 K	θ increases with P & T [64]	water-wet less than 50° for aged surface: intermediate-wet

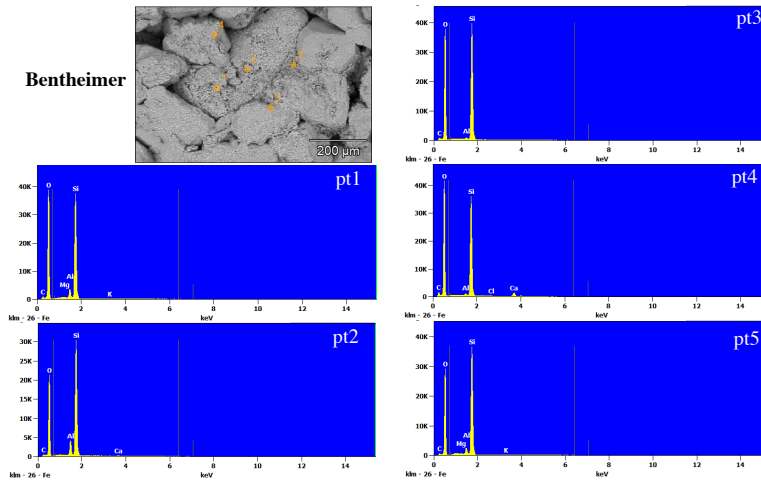


Figure B.1: SEM data of Bentheimer sandstone.

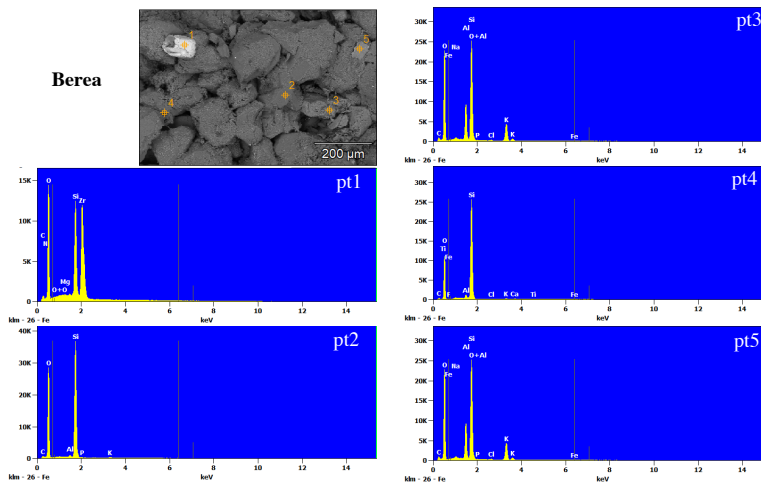


Figure B.2: SEM data of Berea sandstone.

Table B.3: Density of water and hydrogen phases used for contact angle measurement of hydrogen/pure water/Bentheimer tests.

Temp. (°C)	Press. (bar)	$\rho_w(\text{kg/m}^3)$	$\rho_{\text{H}_2}(\text{kg/m}^3)$
22.3	20.3	997.51	1.65
23.5	50.2	998.57	3.98
23.4	70.7	999.51	5.55
23.9	100.5	1000.71	7.73
24.4	23.5	997.16	1.89
24.5	50.7	998.35	4.01
25.0	70.4	999.11	5.49
25.1	100.7	1000.42	7.72
31.9	22.0	995.12	1.73
32.5	51.8	996.25	3.99
32.8	71.5	997.01	5.44
33.2	100.5	998.15	7.51
39.5	20.3	992.68	1.56
39.9	50.2	993.83	3.78
40.1	72.8	994.73	5.41
40.3	100.3	995.84	7.33
38.8	20.7	992.93	1.59
39.0	48.8	994.08	3.69
39.4	70.6	994.88	5.26
39.5	99.2	996.07	7.27
49.1	19.8	989.17	1.47
49.2	50.6	990.44	3.70
49.3	70.2	991.23	5.08
49.3	101.2	992.53	7.20

Table B.4: Density of brine and hydrogen phases used for contact angle measurement of hydrogen/brine (5000 ppm NaCl)/Bentheimer tests.

Temp. (°C)	Press. (bar)	$\rho_w(\text{kg/m}^3)$	$\rho_{H_2}(\text{kg/m}^3)$
21.3	20.0	1000.91	1.63
22.1	51.9	1002.16	4.13
22.3	71.5	1002.99	5.63
22.9	100.5	1004.14	7.76
24.0	20.3	1000.29	1.64
24.8	49.4	1001.39	3.91
24.7	70.9	1002.37	5.54
24.4	100.9	1003.77	7.75
31.7	21.0	998.24	1.65
32.2	49.9	999.36	3.85
32.7	71.1	1000.13	5.41
33.1	98.9	1001.21	7.40
38.9	19.6	995.91	1.51
39.5	50.8	997.05	3.83
39.9	69.9	997.73	5.20
40.1	100.1	998.95	7.32
38.7	20.4	996.02	1.57
39.0	51.1	997.24	3.86
39.2	70.1	997.98	5.23
39.4	100.4	999.20	7.36
47.4	20.7	992.88	1.55
48.3	51.3	993.82	3.76
49.0	70.6	994.35	5.11
49.2	100.7	995.53	7.16

Table B.5: Density of brine and hydrogen phases used for contact angle measurement of hydrogen/brine (50,000 ppm NaCl)/Bentheimer tests.

Temp. (°C)	Press. (bar)	$\rho_w(\text{kg/m}^3)$	$\rho_{H_2}(\text{kg/m}^3)$
31.3	21.1	1004.18	1.66
31.9	51.4	1004.82	3.97
33.0	70.6	1004.43	5.37
33.3	100.7	1005.37	7.52

Table B.6: Density of brine and hydrogen phases used for contact angle measurement of hydrogen/synthetic seawater/Bentheimer tests.

Temp. (°C)	Press. (bar)	$\rho_w(\text{kg/m}^3)$	$\rho_{H_2}(\text{kg/m}^3)$
31	20.5	1006.82	1.61
31.3	50.2	1007.89	3.88
31.6	69.6	1008.51	5.32
31.6	100.9	1009.85	7.57

Table B.7: Density of water and hydrogen phases used for contact angle measurement of hydrogen/pure water/Berea tests.

Temp. (°C)	Press. (bar)	ρ_w (kg/m ³)	ρ_{H_2} (kg/m ³)
23.6	20.8	997.23	1.68
23.5	50.6	998.59	4.01
23.7	70.2	999.42	5.50
23.9	100.7	1000.72	7.75
24.0	20.7	997.13	1.67
23.7	50.7	998.55	4.02
23.5	71.5	999.52	5.60
23.5	100.8	1000.82	7.77
22.4	19.7	997.46	1.60
22.8	49.1	998.69	3.91
32.6	19.4	994.80	1.52
32.7	50.0	996.11	3.85
32.8	69.3	996.92	5.28
33.0	101.1	998.24	7.56
38.6	21.2	993.02	1.63
38.6	51.0	994.30	3.85
38.6	69.4	995.09	5.19
38.9	100.7	996.33	7.39
47.6	20.5	989.78	1.53
47.8	49.4	990.93	3.63
48.2	70.6	991.68	5.12
48.2	99.7	992.90	7.12

Table B.8: Density of brine and hydrogen phases used for contact angle measurement of hydrogen/brine (5000 ppm NaCl)/Berea tests.

Temp. (°C)	Press. (bar)	ρ_w (kg/m ³)	ρ_{H_2} (kg/m ³)
21.6	20.2	1000.85	1.64
21.8	50.6	1002.17	4.04
22.3	70.2	1002.93	5.53
22.6	100.2	1004.20	7.74
32.4	21.6	998.06	1.69
32.4	50.6	999.33	3.90
32.5	71.4	1000.21	5.44
32.5	98.7	1001.39	7.40
47.3	21.6	992.95	1.61
47.7	49.6	993.98	3.65
48.1	69.9	994.68	5.07
48.5	99.6	995.77	7.10

Table B.9: Contact angle values of hydrogen/pure water/Bentheimer, repeated tests.

Test No.	Temp. (°C)	Press. (bar)	θ_{ave} (°)	θ_{range} (°)	Vol.ave (mm ³)	Vol.range (mm ³)
1 T~20°C	24.4	23.5	33.7	[30.5, 38.8]	4.88	[1.99, 8.23]
	24.5	50.7	34.8	[30.3, 42.7]	4.05	[1.21, 7.10]
	25	70.4	37.5	[33.4, 44.4]	2.75	[0.96, 4.41]
	25.1	100.7	36.4	[32.4, 41.8]	3.91	[1.29, 8.37]
2 T~40°C	38.8	20.7	35.3	[31.5, 42.8]	3.92	[1.30, 6.64]
	39	48.8	35.3	[32.4, 41.6]	4.21	[1.41, 7.64]
	39.4	70.6	31.1	[27.3, 34.9]	4.47	[1.79, 8.59]
	39.5	99.2	36.2	[31.6, 42.3]	3.58	[1.15, 7.22]

Table B.10: Contact angle values of hydrogen/brine (5000 ppm NaCl)/Bentheimer, repeated tests.

Test No.	Temp. (°C)	Press. (bar)	θ_{ave} (°)	θ_{range} (°)	Vol.ave (mm ³)	Vol.range (mm ³)
1 T~20°C	24	20.3	33.7	[29.7, 40.4]	3.92	[1.53, 5.56]
	24.8	49.4	35.6	[30.8, 42.6]	3.63	[1.18, 6.79]
	24.7	70.9	35.9	[30.5, 43.1]	3.45	[1.08, 5.97]
	24.4	100.9	32.4	[29.5, 37.5]	4.33	[1.54, 7.46]
2 T~40°C	38.7	20.4	31.3	[30.1, 33.3]	4.06	[2.41, 5.91]
	39	51.1	31.69	[27.4, 35.5]	3.89	[1.78, 6.27]
	39.2	70.1	37.4	[34.5, 40.3]	2.54	[1.32, 3.90]
	39.4	100.4	33.6	[30.5, 38.6]	3.51	[1.18, 6.43]

Table B.11: Contact angle values of hydrogen/pure water/Berea, repeated tests.

Test No.	Temp. (°C)	Press. (bar)	θ_{ave} (°)	θ_{range} (°)	Vol.ave (mm ³)	Vol.range (mm ³)
1 T~20°C	24	20.7	30.5	[26.4,38.6]	5.17	[0.71,10.29]
	23.7	50.7	29.3	[25.3, 37.5]	5.35	[0.57, 12.05]
	23.5	71.5	26.6	[22.7, 32.8]	5.93	[0.76, 13.08]
	23.5	100.8	24.2	[22.2, 26.5]	9.68	[1.34, 17.42]
2 T~20°C	22.4	19.7	22.8	[20.76, 25.06]	8.66	[2.16, 16.84]
	22.8	49.1	26.4	[23.44, 29.44]	6.02	[1.05, 11.97]

Table B.12: Contact angle values of hydrogen/brine (5000 ppm NaCl)/Berea.

Test No.	Temp. (°C)	Press. (bar)	θ_{ave} (°)	θ_{range} (°)	Vol.ave (mm ³)	Vol.range (mm ³)
1 T~20°C	21.6	20.2	27.2	[23.3,30.9]	6.91	[2.86,11.48]
	21.8	50.6	28.7	[25.3,31.8]	6.74	[1.41,15.52]
	22.3	70.2	29.6	[25.6,33.3]	5.21	[0.97,12.11]
	22.6	100.2	27.5	[25.3,30.1]	3.59	[2.15,5.03]
2 T~30°C	32.4	21.6	27.1	[25.1,28.3]	7.21	[3.05,11.91]
	32.4	50.6	27.8	[23.5,31.7]	5.99	[1.57,11.15]
	32.5	71.4	28	[23.7,31.2]	4.19	[1.18,8.15]
	32.5	98.7	27.9	[26.0,30.9]	5.05	[1.22,9.11]
4 T~50°C	47.3	21.6	30.4	[26.5,33.2]	4.71	[2.63,6.96]
	47.7	49.6	29.1	[26.6,33.7]	4.3	[0.94,7.79]
	48.1	69.9	27.3	[19.9,34.5]	3.88	[1.04,7.37]
	48.5	99.6	29.3	[26.6,33.7]	4.86	[0.88,10.18]

C

CONTACT ANGLE MEASUREMENTS FOR MIXTURE OF (H₂-CH₄) - BRINE

Experimental Apparatus and Procedure

A schematic of the experimental apparatus can be seen in Fig. C.1.

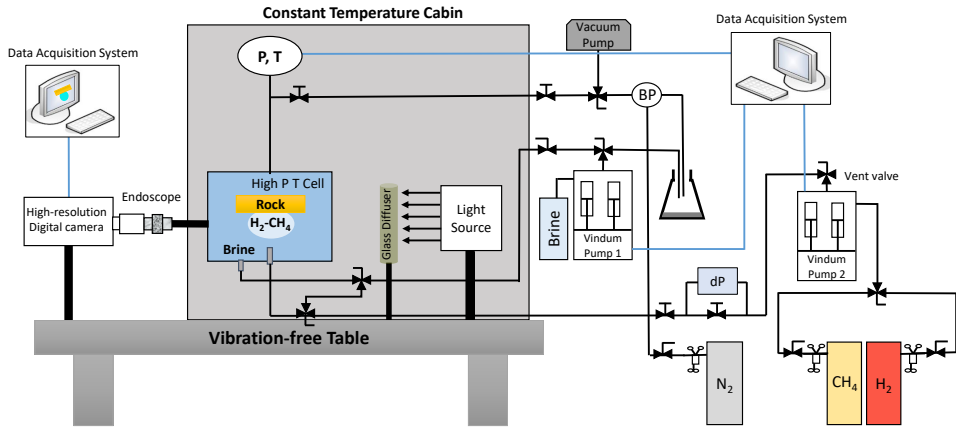


Figure C.1: Schematic of the captive-bubble cell device used for the experiments.

Contact angle measurements

In the following, the contact angles for the gas/brine/Bentheimer systems, measured directly from the images, at different pressure, temperature, and salinity values are listed (Tables C.1 -C.11). For completeness, the contact angles for H₂ which were presented in [63] are included as well. In addition, the density values used in the calculation of the contact angles can be found in Tables C.12 -C.22. The densities of the mixtures were calculated based on the pure gas densities according to

$$\rho_m = (\rho_1 V_1 + \rho_2 V_2) / (V_1 + V_2). \quad (C.1)$$

Here, ρ is density [kg/m³], V is volume [m³], and subscripts m , 1, 2 stand for mixture, gas 1 and gas 2, respectively. This can conveniently be calculated using the website www.fluidat.com.

Table C.1: Contact angle values of H₂/pure water/Bentheimer [63]

Test No.	Temp. (°C)	Press. (bar)	θ_{ave} (°)	θ_{range} (°)	Vol. _{ave} (mm ³)	Vol. _{range} (mm ³)
T~30°C	31.9	22	33.7	[30.6, 37.1]	3.48	[2.21, 4.66]
	32.5	51.8	30.5	[29.4, 32.9]	3.09	[2.20, 3.66]
	32.8	71.5	33.9	[32.6, 36.5]	3.39	[2.38, 4.48]
	33.2	100.5	31.7	[29.0, 39.0]	5.27	[1.93, 9.49]
T~50°C	49.1	19.8	28.4	[26.1, 29.2]	7.42	[3.96, 10.65]
	49.2	50.6	33.2	[29.4, 39.3]	4.7	[1.68, 8.39]
	49.3	70.2	29.8	[28.6, 31.2]	4.41	[2.66, 6.33]
	49.3	101.2	32.8	[29.9, 38.0]	4.12	[2.14, 6.35]

Table C.2: Contact angle values of H₂/brine (5000 ppm NaCl)/Bentheimer[63]

Test No.	Temp. (°C)	Press. (bar)	θ_{ave} (°)	θ_{range} (°)	Vol. _{ave} (mm ³)	Vol. _{range} (mm ³)
T~30°C	31.7	21	29.5	[28.7, 30.5]	4.61	[2.67, 6.55]
	32.2	49.9	34.9	[30.8, 42.2]	3.42	[1.21, 5.77]
	32.7	71.1	36	[32.8, 41.6]	2.8	[1.19, 4.72]
	33.1	98.9	31.9	[31.1, 34.1]	5.59	[2.08, 11.13]
T~50°C	47.4	20.7	33.6	[29.2, 40.2]	4.48	[1.51, 7.78]
	48.3	51.3	33.6	[29.9, 41.4]	4.03	[1.40, 6.45]
	49	70.6	34.2	[30.0, 41.5]	4.34	[1.50, 7.91]
	49.2	100.7	33.7	[29.9, 41.6]	5.7	[1.31, 12.66]

Table C.3: Contact angle values of (80% H₂ - 20% CH₄)/pure water/Bentheimer

Test No.	Temp. (°C)	Press. (bar)	θ_{ave} (°)	θ_{range} (°)	Vol. _{ave} (mm ³)	Vol. _{range} (mm ³)
T~30°C	32.1	21.1	32.6	[29.6, 36.0]	6.20	[2.27, 11.23]
	32.1	49.0	31.8	[25.7, 36.7]	6.40	[2.44, 10.77]
	32.1	68.4	32.9	[29.8, 36.1]	6.20	[2.02, 12.17]
	32.1	100.8	33.2	[27.2, 37.1]	6.03	[2.32, 10.72]
T~50°C	48.2	22.2	32.7	[29.5, 36.6]	6.10	[2.36, 11.33]
	48.3	49.5	32.2	[27.1, 36.1]	6.31	[1.99, 11.20]
	48.4	70.3	32.4	[29.2, 36.6]	6.42	[2.14, 11.74]
	48.4	99.9	33.3	[31.5, 37.5]	6.89	[1.97, 13.25]

Table C.4: Contact angle values of (80% H₂ - 20% CH₄)/brine (5000 ppm NaCl)/Bentheimer

Test No.	Temp. (°C)	Press. (bar)	θ_{ave} (°)	θ_{range} (°)	Vol. _{ave} (mm ³)	Vol. _{range} (mm ³)
T~30°C	33.1	19.7	30.0	[24.7, 35.1]	6.47	[2.00, 12.18]
	32.8	50.1	30.3	[25.6, 33.6]	6.10	[2.32, 12.13]
	32.8	71.3	30.3	[27.9, 33.9]	6.72	[2.78, 11.72]
	32.7	99.4	30.4	[25.8, 34.3]	6.58	[2.36, 12.64]
T~50°C	48.9	21.3	31.6	[26.9, 36.3]	6.62	[2.38, 10.78]
	49.0	49.4	32.3	[28.5, 37.3]	7.03	[2.81, 12.21]
	49.0	70.8	34.6	[32.5, 37.4]	4.47	[2.61, 6.02]
	49.1	99.0	32.5	[28.0, 37.1]	5.61	[2.29, 8.72]

Table C.5: Contact angle values of (50% H₂ - 50% CH₄)/pure water/Bentheimer

Test No.	Temp. (°C)	Press. (bar)	θ_{ave} (°)	θ_{range} (°)	Vol. _{ave} (mm ³)	Vol. _{range} (mm ³)
T~30°C	31.8	20.7	32.7	[29.2,38.1]	5.72	[2.05,9.93]
	31.9	46.7	35.7	[33.6,39.3]	3.86	[1.61,6.52]
	32.0	68.2	34.5	[32.2,37.8]	4.54	[1.94,6.79]
	32.0	104.2	33.4	[26.8,39.4]	5.74	[1.71,11.59]
T~50°C	47.7	21.3	32.1	[29.8,34.2]	5.39	[2.44,8.22]
	47.7	52.2	32.4	[27.3,35.9]	3.72	[1.76,5.59]
	47.7	69.6	33.2	[27.6,37.7]	5.98	[2.22,10.59]
	47.7	98.3	32.9	[29.2,39.0]	3.72	[1.71,6.27]

Table C.6: Contact angle values of (50% H₂ - 50% CH₄)/brine (5000 ppm NaCl)/Bentheimer

Test No.	Temp. (°C)	Press. (bar)	θ_{ave} (°)	θ_{range} (°)	Vol. _{ave} (mm ³)	Vol. _{range} (mm ³)
T~30°C	32.1	20.9	27.2	[24.7,31.4]	6.71	[3.28,10.78]
	32.2	49.2	31.4	[29.5,34.6]	5.47	[2.43,9.06]
	32.2	71.3	31.9	[26.6,35.7]	6.17	[2.13,10.70]
	32.3	100.5	35.0	[29.1,40.8]	4.52	[1.48,9.13]
T~50°C	48.2	20.2	29.9	[25.6,34.3]	6.04	[2.61,9.93]
	48.2	50.5	33.9	[31.9,35.3]	3.26	[2.24,4.43]
	48.0	70.5	30.1	[27.2,34.4]	5.08	[2.26,8.48]
	48.0	100.7	34.6	[34.2,35.7]	5.20	[3.67,6.88]

Table C.7: Contact angle values of (20% H₂ - 80% CH₄)/pure water/Bentheimer

Test No.	Temp. (°C)	Press. (bar)	θ_{ave} (°)	θ_{range} (°)	Vol. _{ave} (mm ³)	Vol. _{range} (mm ³)
T~30°C	32.1	21.0	31.4	[26.5,34.3]	6.82	[2.92,12.16]
	32.1	51.1	33.7	[31.1,36.3]	4.88	[2.21,8.31]
	32.0	68.6	32.8	[29.6,38.6]	6.10	[1.74,11.61]
	32.1	101.4	34.7	[28.8,38.7]	3.42	[1.57,6.20]
T~50°C	47.9	21.0	31.6	[28.3,35.7]	6.24	[2.51,10.78]
	48.2	49.9	32.9	[30.5,35.4]	4.23	[2.26,6.47]
	48.4	69.3	33.5	[29.9,36.4]	4.56	[2.09,8.16]
	48.6	102.9	34.3	[29.3,38.8]	4.82	[1.44,10.01]

Table C.8: Contact angle values of (20% H₂ - 80% CH₄)/brine (5000 ppm NaCl)/Bentheimer

Test No.	Temp. (°C)	Press. (bar)	θ_{ave} (°)	θ_{range} (°)	Vol. _{ave} (mm ³)	Vol. _{range} (mm ³)
T~30°C	31.8	20.6	32.4	[29.0,37.0]	6.25	[2.11,10.92]
	31.9	48.8	33.5	[29.6,39.1]	5.86	[1.59,11.42]
	32.0	70.8	32.5	[26.8,37.7]	5.91	[1.97,11.52]
	32.1	102.0	35.2	[31.3,39.9]	3.53	[1.31,6.29]
T~50°C	47.3	19.1	31.9	[26.7,35.0]	6.53	[2.41,11.73]
	47.9	48.8	33.3	[30.6,36.9]	3.95	[2.07,5.65]
	48.5	70.5	34.5	[30.1,37.8]	5.10	[2.92,7.37]
	49.0	102.2	34.5	[31.3,38.9]	4.28	[1.78,7.32]

Table C.9: Contact angle values of CH₄/pure water/Bentheimer

Test No.	Temp. (°C)	Press. (bar)	θ_{ave} (°)	θ_{range} (°)	Vol. _{ave} (mm ³)	Vol. _{range} (mm ³)
T~30°C	31.6	21.1	31.8	[27.5,36.1]	6.08	[2.08,10.99]
	31.8	47.4	31.2	[27.9,34.3]	4.77	[2.32,8.08]
	31.9	70.0	32.6	[28.9,35.3]	5.61	[2.14,8.70]
	32.1	99.1	31.7	[27.5,34.2]	4.97	[2.34,7.61]
T~50°C	48.1	20.5	30.0	[26.4,33.7]	7.37	[2.29,13.21]
	48.2	49.4	30.6	[26.9,34.4]	6.17	[2.73,10.35]
	48.3	70.9	33.8	[31.8,37.5]	2.63	[1.57,3.85]
	48.2	100.0	33.5	[30.9,36.1]	3.05	[1.85,4.52]

Table C.10: Contact angle values of CH₄/brine (5000 ppm NaCl)/Bentheimer

Test No.	Temp. (°C)	Press. (bar)	θ_{ave} (°)	θ_{range} (°)	Vol. _{ave} (mm ³)	Vol. _{range} (mm ³)
T~30°C	32.1	20.7	33.8	[30.3,37.3]	4.66	[3.56,6.33]
	32.3	49.0	34.1	[29.3,40.8]	5.75	[2.02,10.26]
	32.5	69.7	32.6	[28.8,34.8]	4.67	[2.80,6.74]
	32.7	100.1	34.6	[30.7,36.9]	5.87	[2.02,9.29]
T~50°C	47.9	21.6	33.5	[29.7,37.1]	5.67	[2.95,9.78]
	48.1	49.5	33.9	[27.4,39.1]	5.75	[1.88,11.48]
	48.2	71.7	34.8	[28.4,40.2]	5.06	[1.53,10.42]
	48.3	98.7	35.6	[28.6,40.9]	3.71	[1.73,6.14]

Table C.11: Contact angle values of CH₄/brine (50000 ppm NaCl)/Bentheimer

Test No.	Temp. (°C)	Press. (bar)	θ_{ave} (°)	θ_{range} (°)	Vol. _{ave} (mm ³)	Vol. _{range} (mm ³)
T~30°C	32.2	20.3	36.0	[35.0,36.3]	4.57	[3.52,5.63]
	32.3	50.0	33.3	[28.9,37.9]	5.59	[3.38,8.01]
	32.4	73.5	34.9	[31.3,38.9]	3.55	[2.16,5.26]
	32.6	100.4	33.9	[29.5,38.5]	3.66	[2.15,5.32]
T~50°C	48.4	18.0	29.2	[26.6,31.3]	6.42	[5.60,7.34]
	48.6	49.6	32.6	[25.1,38.5]	7.29	[4.64,10.48]
	48.6	71.1	35.2	[29.4,40.4]	3.99	[1.82,6.53]
	48.8	99.7	36.0	[28.9,41.8]	6.31	[4.11,9.31]

Table C.12: Density of liquid and gas phases used for contact angle measurement of H₂/pure water/Bentheimer tests[63]

Temp. (°C)	Press. (bar)	ρ_{liquid} (kg/m ³)	ρ_{gas} (kg/m ³)
31.9	22.0	995.12	1.73
32.5	51.8	996.25	3.99
32.8	71.5	997.01	5.44
33.2	100.5	998.15	7.51
49.1	19.8	989.17	1.47
49.2	50.6	990.44	3.70
49.3	70.2	991.23	5.08
49.3	101.2	992.53	7.20

Table C.13: Density of liquid and gas phases used for contact angle measurement of H₂/brine (5000 ppm NaCl)/Bentheimer tests[63]

Temp. (°C)	Press. (bar)	$\rho_{\text{liquid}}(\text{kg/m}^3)$	$\rho_{\text{gas}}(\text{kg/m}^3)$
31.7	21.0	998.24	1.65
32.2	49.9	999.36	3.85
32.7	71.1	1000.13	5.41
33.1	98.9	1001.21	7.40
47.4	20.7	992.88	1.55
48.3	51.3	993.82	3.76
49.0	70.6	994.35	5.11
49.2	100.7	995.53	7.16

Table C.14: Density of liquid and gas phases used for contact angle measurement of (80% H₂ - 20% CH₄)/pure water/Bentheimer tests

Temp. (°C)	Press. (bar)	$\rho_{\text{liquid}}(\text{kg/m}^3)$	$\rho_{\text{gas}}(\text{kg/m}^3)$
32.1	21.1	995.02	3.98
32.1	49.0	996.24	9.15
32.1	68.4	997.09	12.66
32.1	100.8	998.49	18.34
48.2	22.2	989.62	3.98
48.3	49.5	990.74	8.77
48.4	70.3	991.59	12.34
48.4	99.9	992.83	17.27

Table C.15: Density of liquid and gas phases used for contact angle measurement of (80% H₂ - 20% CH₄)/brine (5000 ppm NaCl)/Bentheimer tests

Temp. (°C)	Press. (bar)	$\rho_{\text{liquid}}(\text{kg/m}^3)$	$\rho_{\text{gas}}(\text{kg/m}^3)$
33.1	19.7	997.77	3.71
32.8	50.1	999.19	9.33
32.8	71.3	1000.11	13.14
32.7	99.4	1001.36	18.07
48.9	21.3	992.31	3.81
49.0	49.4	993.46	8.74
49.0	70.8	994.36	12.40
49.1	99.0	995.50	17.09

Table C.16: Density of liquid and gas phases used for contact angle measurement of (50% H₂ - 50% CH₄)/pure water/Bentheimer tests

Temp. (°C)	Press. (bar)	$\rho_{\text{liquid}}(\text{kg/m}^3)$	$\rho_{\text{gas}}(\text{kg/m}^3)$
31.8	20.7	995.09	7.49
31.9	46.7	996.20	17.25
32.0	68.2	997.11	25.53
32.0	104.2	998.67	39.68
47.7	21.3	989.78	7.31
47.7	52.2	991.09	18.22
47.7	69.6	991.83	24.48
47.7	98.3	993.04	34.88

Table C.17: Density of liquid and gas phases used for contact angle measurement of (50% H₂ - 50% CH₄)/brine (5000 ppm NaCl)/Bentheimer tests

Temp. (°C)	Press. (bar)	$\rho_{\text{liquid}}(\text{kg/m}^3)$	$\rho_{\text{gas}}(\text{kg/m}^3)$
32.1	20.9	998.12	7.56
32.2	49.2	999.33	18.18
32.2	71.3	1000.29	26.26
32.3	100.5	1001.53	36.74
48.2	20.2	992.54	6.92
48.2	50.5	993.82	17.58
48	70.5	994.75	24.77
48	100.7	996.01	35.70

Table C.18: Density of liquid and gas phases used for contact angle measurement of (20% H₂ - 80% CH₄)/pure water/Bentheimer tests

Temp. (°C)	Press. (bar)	$\rho_{\text{liquid}}(\text{kg/m}^3)$	$\rho_{\text{gas}}(\text{kg/m}^3)$
32.1	21.0	995.01	11.13
32.1	51.1	996.33	27.63
32.0	68.6	997.12	37.43
32.1	101.4	998.52	55.93
47.9	21.0	989.69	10.55
48.2	49.9	990.80	25.39
48.4	69.3	991.54	35.48
48.6	102.9	992.88	52.98

Table C.19: Density of liquid and gas phases used for contact angle measurement of (20% H₂ - 80% CH₄)/brine (5000 ppm NaCl)/Bentheimer tests

Temp. (°C)	Press. (bar)	$\rho_{\text{liquid}}(\text{kg/m}^3)$	$\rho_{\text{gas}}(\text{kg/m}^3)$
31.8	20.6	998.20	10.93
31.9	48.8	999.40	26.37
32.0	70.8	1000.33	38.67
32.1	102.0	1001.65	56.26
47.3	19.1	992.85	9.61
47.9	48.8	993.87	24.85
48.5	70.5	994.55	36.09
49.0	102.2	995.68	52.54

Table C.20: Density of liquid and gas phases used for contact angle measurement of CH₄/pure water/Bentheimer tests

Temp. (°C)	Press. (bar)	$\rho_{\text{liquid}}(\text{kg/m}^3)$	$\rho_{\text{gas}}(\text{kg/m}^3)$
31.6	21.1	995.16	13.81
31.8	47.4	996.26	32.26
31.9	70.0	997.21	49.18
32.1	99.1	998.42	72.04
48.1	20.5	989.59	12.63
48.2	49.4	990.78	31.50
48.3	70.9	991.65	46.25
48.2	100.0	992.91	66.97

Table C.21: Density of liquid and gas phases used for contact angle measurement of CH₄/brine (5000 ppm NaCl)/Bentheimer tests

Temp. (°C)	Press. (bar)	$\rho_{\text{liquid}}(\text{kg/m}^3)$	$\rho_{\text{gas}}(\text{kg/m}^3)$
32.1	20.7	998.11	13.51
32.3	49.0	999.29	33.35
32.5	69.7	1000.13	48.80
32.7	100.1	1001.39	72.61
47.9	21.6	989.71	13.34
48.1	49.5	990.82	31.58
48.2	71.7	991.72	46.83
48.3	98.7	992.82	66.00

Table C.22: Density of liquid and gas phases used for contact angle measurement of CH₄/brine (50000 ppm NaCl)/Bentheimer tests

Temp. (°C)	Press. (bar)	$\rho_{\text{liquid}}(\text{kg/m}^3)$	$\rho_{\text{gas}}(\text{kg/m}^3)$
32.2	20.3	1003.16	13.24
32.3	50.0	1004.32	34.11
32.4	73.5	1005.22	51.75
32.6	100.4	1006.14	72.89
48.4	18.0	992.37	11.05
48.6	49.6	993.63	31.59
48.6	71.1	994.53	46.33
48.8	99.7	995.65	66.56

D

**DEVELOPED DYNAMIC PORE
NETWORK MODELS**

Table D.1: Developed dynamic pore network models

Year	Author(s)	Title	Ref.
1985	Koplik, Lasseter	Two-phase flow in random network models of porous media	[124]
1988	Lenorman et al.	Numerical models and experiments on immiscible displacements in porous media	[121]
1991	Blunt, King	Relative permeabilities from two-and three-dimensional pore-scale network modelling	[153]
1996	Lee, Padmanabhan	Simulation of linear displacement experiments on massively parallel computers	[154]
1996	Kamath et al.	Pore network modeling of laboratory experiments on heterogeneous carbonates	[155]
1997	van der Marck et al.	Viscous and capillary pressures during drainage: Network simulations and experiments	[156]
1998	Mogensen, Stenby	A dynamic two-phase pore-scale model of imbibition	[137]
1998	Aker et al.	A two-dimensional network simulator for two-phase flow in porous media	[157]
1999	Dahle, Celia	A dynamic network model for two-phase immiscible flow	[158]
2000	Hughes, Blunt	Pore-scale modeling of rate effects in imbibition	[159]
2002	Constantinides, Payatakes	Pore-scale modeling of fluid transport in disordered fibrous materials	[160]
2003	Singh, Mohanty	Dynamic modeling of drainage through three-dimensional porous materials	[161]
2003	Nordhaug	A pore network model for calculation of interfacial velocities	[162]
2005	Al-Gharbi, Blunt	Dynamic network modeling of two-phase drainage in porous media	[125]
2006	Nguyen et al.	The effect of displacement rate on imbibition relative permeability and residual saturation	[163]
2006	Di Carlo	Quantitative network model predictions of saturation behind infiltration fronts and comparison with experiments	[164]
2007	Piri, Karpyn	Prediction of fluid occupancy in fractures using network modeling and x-ray microtomography. ii: Results	[165]
2010a	Joekar et al.	Non-equilibrium effects in capillarity and interfacial area in two-phase flow: dynamic pore-network modelling	[134]
2010b	Joekar et al.	Network model investigation of interfacial area, capillary pressure, and saturation relationships in granular porous media	[139]
2011	Joekar, Hassanizadeh	Effect of fluids properties on non-equilibrium capillarity effects: Dynamic pore-network modeling	[166]
2011	Joekar, Hassanizadeh	Specific interfacial area: The missing state variable in two-phase flow equations?	[167]
2012	Joekar, Hassanizadeh	Analysis of fundamentals of two-phase flow in porous media using dynamic pore-network models: A review	[136]
2012	Ellis, Bazylak	Dynamic pore network model of surface heterogeneity in brine-filled porous media for carbon sequestration,	[168]
2012	Hammond, Unsal	A dynamic pore network model for oil displacement by wettability altering surfactant solution	[169]
2013	Sheng, Thompson	Dynamic coupling of pore-scale and reservoir-scale models for multiphase flow	[170]

Table D.2: Developed dynamic pore network models (continued).

Year	Author(s)	Title	Ref.
2015	Aghaei, Piri	Direct pore-to-core up-scaling of displacement processes: Dynamic pore network modeling and experimentation	[126]
2015	Bagudu et al.	Pore-to-core-scale network modelling of co2 migration in porous media	[171]
2016	Khayrat, Jenny	Subphase approach to model hysteretic two-phase flow in porous media	[141]
2016	Huang et al.	Multi-physics pore-network modeling of two-phase shale matrix flows	[172]
2016	Qin et al.	Pore-network modeling of water and vapor transport in the microporous layer and gas diffusion layer of a polymer electrolyte fuel cell	[140]
2016	Cao et al.	Supercritical co2 and brine displacement in geological carbon sequestration: Micromodel and pore network simulation studies	[173]
2016	Sheng, Thompson	A unified pore-network algorithm for dynamic two-phase flow	[174]
2017	Regaeig, Moncorge	Adaptive dynamic/quasi-static pore network model for efficient multiphase flow simulation	[175]
2017	Li et al.	Dynamic pore-scale network model (PNM) of water imbibition in porous media	[131]
2017	Yang et al.	Pore to pore validation of pore network modelling against micromodel experiment results	[176]
2017	Boujelben, McDougall	Dynamic pore-scale modelling of multiphase flow during application of eor techniques	[123]
2018	Boujelben et al.	Pore network modelling of low salinity water injection under unsteady-state flow conditions	[177]
2018	Gesho, et al.	Dynamic pore network modeling of two-phase flow through fractured porous media: Direct pore-to-core up-scaling of displacement processes	[178]
2018	Gjennestad, et al.,	Stable and efficient time integration of a a dynamic pore network model for two-phase flow in porous media	[179]
2018	Sweijen et al.	Dynamic pore-scale model of drainage in granular porous media: The pore-unit assembly method	[180]
2019	Qin et al.	A dynamic pore-network model for spontaneous imbibition in porous media	[181]
2019	Qin et al.	Dynamic pore-network modeling of air-water flow through thin porous layers	[182]
2019	Yin, et al.	Dynamic pore-network models development, in: Advances in Mathematical Methods and High-Performance Computing	[183]
2019	Sinha et al.	A dynamic network simulator for immiscible two-phase flow in porous media	[184]
2020	Chen, Guo	Fully implicit dynamic pore-network modeling of two-phase flow and phase change in porous media	[127]
2020	Gong and Piri	Pore-to-core upscaling of solute transport under steady-state two-phase flow conditions using dynamic pore network modeling approach	[185]
2021	Prmikulov et al.	Wettability and lenormand's diagram	[186]

E

PORE NETWORK MODELLING (PNM)

E.1. THE STRUCTURE OF THE NETWORK DATA FILES FOR PNMS

E.1.1. CLASSICAL FORMAT (STATOIL PROTOCOL)

The network data are stored in four ASCII files. The format of these files is that of Statoil. The physical data are given in the SI unit system.

- Throat Data

The data for the throats are read from the link files such as Figure E.1. The structure of the link files is as follows:

Example of <i>prefix_link1.dat</i> file							
26146							
1	-1	8	0.349563E-04	0.297308E-01	0.160000E-03		
2	-1	53	0.171065E-04	0.442550E-01	0.211076E-04		
3	-1	60	0.198366E-04	0.354972E-01	0.300000E-04		

Example of <i>prefix_link2.dat</i> file							
22714	10452	10533	0.178262E-04	0.120716E-03	0.239385E-04	0.218282E-13	0.137097E-14
22715	10452	10612	0.121673E-04	0.747863E-04	0.100000E-04	0.266790E-13	0.355565E-14
22716	10453	10534	0.100000E-04	0.270040E-04	0.139862E-04	0.543278E-13	0.863932E-14

Figure E.1: Examples of *prefix_link1.dat* and *prefix_link2.dat* files

1. *prefix_link1.dat* file

The first line of the file contains a single entry that is the total number of throats say N, followed by N data lines. Each of these lines contains six data entries in the following order presented in Table E.1:

2. *prefix_link2.dat* file

For a network with N throats, the file contains N data lines. Each line has eight data entries in the following order presented in Table E.1:

Table E.1: The structure of throat data files.

Column No.	<i>prefix_link1.dat</i>	<i>prefix_link2.dat</i>
1	Throat index	Throat index
2	Pore 1 index	Pore 1 index
3	Pore 2 index	Pore 2 index
4	Throat radius	Length of pore 1
5	Throat shape factor	Length of pore 2
6	Throat total length	Length of throat
7	(pore center to pore center)	Throat volume
8		Throat clay volume

This section is taken from PhD thesis of Taha Sochi (2007), Appendix I, [187].

- Pore Data

The data for the pores are read from the node files such as Figure E.2. The structure of the node files is as follows:

Example of *prefix_node1.dat* file

```
12349 0.300000E-02 0.300000E-02 0.300000E-02
1 0.350000E-03 0.000000E+00 0.700000E-04 3 796 674 2 0 0 522 523 524
2 0.450000E-03 0.500000E-04 0.000000E+00 3 359 31 1 0 0 525 526 524
3 0.880000E-03 0.100000E-04 0.000000E+00 1 392 0 0 527
```

Example of *prefix_node2.dat* file

```
50 0.373367E-13 0.195781E-04 0.336954E-01 0.784623E-16
51 0.155569E-14 0.821594E-05 0.326262E-01 0.471719E-16
52 0.171126E-13 0.122472E-04 0.329865E-01 0.148506E-15
```

Figure E.2: Examples of *prefix_node1.dat* and *prefix_node2.dat* files

E

1. *prefix_node1.dat* file

The first line of the file contains four entries: the total number of pores, the length (x-direction), width (y-direction), and height (z-direction) of the network. For a network with M pores, the first line is followed by M data lines each containing the following data entries presented in Table E.2: Note that for a pore with a connection number i there are $2(i + 1)$ entries as follows:

- The first i entries are the connecting pores indices
- The $(i + 1)$ st entry is the pore “inlet” status (0 for false and 1 for true)
- The $(i + 2)$ nd entry is the pore “outlet” status (0 for false and 1 for true)
- The last i entries are the connecting throats indices

Note: the inlet/outlet pores are those pores that are connected to a throat whose other pore is the inlet/outlet reservoir, i.e. the other pore has an index of $-1/0$. So if the $(i + 1)$ st entry is 1, one of the connecting pores indices is -1 , and if the $(i + 2)$ nd entry is 1, one of the connecting pores indices is 0.

2. *prefix_node2.dat* file

For a network with M pores, the file contains M data lines. Each line has five data entries in the following order presented in Table E.2:

Table E.2: The structure of pore data files.

Column No.	<i>prefix_node1.dat</i>	<i>prefix_node2.dat</i>
1	Pore index	Pore index
2	Pore x -coordinate	Pore volume
3	Pore y -coordinate	Pore radius
4	Pore z -coordinate	Pore shape factor
5	Pore connection number	Pore clay volume

E.1.2. DUMUX FORMAT

DuMux can read grids in two ways:

1. From a file using the Dune Grid Format (DGF), an example is shown in Figure E.3.

```

1 DGF
2 % Vertex parameters: PoreInscribedRadius PoreLabel PoreGeometry
3 % Element parameters: ThroatInscribedRadius ThroatLength ThroatLabel
  ThroatCrossSectionShape ThroatShapeFactor ThroatCrossSectionalArea
4 Vertex % Coordinates and volumes of the pore bodies
5 parameters 3
6 3.000000e-03 1.360000e-03 2.200000e-04 2.276560e-05 3 5
7 5.600000e-04 1.390000e-03 2.400000e-04 2.452120e-05 -1 5
8 ...
9 #
10
11 SIMPLEX % Connections of the pore bodies (pore throats)
12 parameters 6
13 144 145 1.300780e-05 1.604900e-05 2 0 4.811000e-02 8.792500e-10
14 188 189 2.673390e-05 1.000010e-05 3 0 1.945670e-02 9.183230e-09
15 3572 4064 9.937020e-06 1.280630e-04 -1 0 2.590690e-02 9.528771e-10
16 ...
17 #

```

Figure E.3: DGF file format.

2. Generate a statistical network using the following parameters, in Figure E.4.

```

[Grid]
UpperRight = 4e-4 4e-4 4e-4
LowerLeft = 0 0 0
NumPores = 5 5 5
ParameterType = lognormal
MeanPoreInscribedRadius = 1e-5
StandardDeviationPoreInscribedRadius = 0.0 #4e-6
PoreGeometry = Cube
ThroatCrossSectionShape = Square
ParameterRandomNumberSeed = 1
BoundaryFaceMarker = 2 3 1 1 1 1
MinThroatLength = 1e-10
DeletionProbability = 0.0 0.0 0.0 1 1 1 1 1 1 1 1 1
RemoveThroatsOnBoundary = 0 1
CapPoresOnBoundaries = 0 1 2 3 4 5
Sanitize = true
DeletionRandomNumberSeed = 33

```

Figure E.4: Statistical network generator.

This section is adopted from DuMux: <https://dumux.org/>.

E.2. PORE NETWORK MODELLING

In various fields such as hydrology, environmental engineering, and petroleum engineering, large-scale numerical simulations play a vital role in predicting a wide range of phenomena. These phenomena include the movement of non-aqueous phase liquid (NAPL) through unsaturated soils, enhanced oil recovery, and CO₂ sequestration. To conduct accurate numerical reservoir simulations of multi-phase flow, it is crucial to represent macroscopic properties like capillary pressures and relative permeabilities as functions of phase saturations [188].

Traditionally, laboratory experiments have been employed to measure these macroscopic properties. However, these experiments can be costly, time-consuming, and limited to specific conditions. Alternatively, a reliable physically-based model can be developed to predict multiphase flow at the pore scale. By extrapolating these predictions, it becomes possible to estimate relative permeabilities and capillary pressures at the macroscopic scale [188].

To achieve this, a physically-based model must be rooted in the pore-level physics of displacement mechanisms and rely on an accurate representation of the pore space structure. This structure can be obtained by acquiring a three-dimensional (3D) image using computer tomography (CT) imaging of core samples or through numerical reconstructions from two-dimensional (2D) thin sections using process-based algorithms or statistical methods. Once a 3D image of the pore space is available, fluid flow can be simulated directly using methods like the Lattice-Boltzmann method. However, for multiphase flow, this approach becomes computationally inefficient, leading to the utilization of pore-scale network modeling (PNM) instead [188].

PNM requires a pore network that accurately replicates the topological and geometrical characteristics of the actual pore space. This pore network can be extracted from the 3D images of the pore structure. Additionally, an accurate description of pore-level flow physics is crucial for predicting multiphase flow behavior. Therefore, when a pore network is provided, pore-network modeling becomes an appealing tool for estimating macroscopic transport properties under arbitrary wetting conditions [188].

In Figure E.5, an illustration of alternative workflows from core samples to relative permeabilities and capillary pressure demonstrates the connection between PNM and the estimation of these macroscopic properties

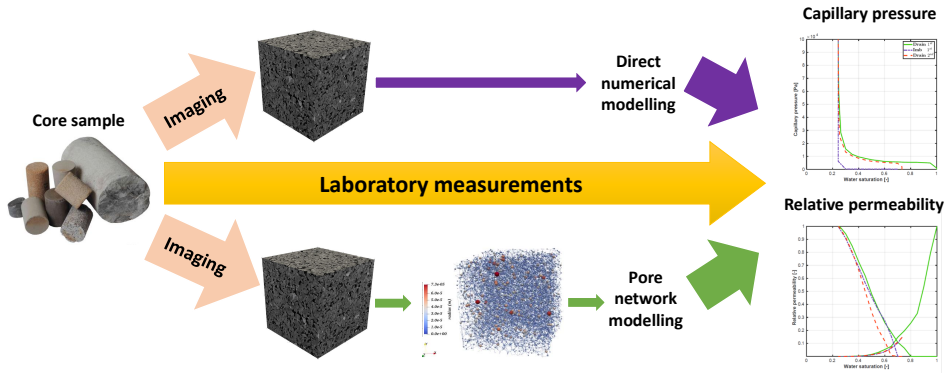


Figure E.5: Different processes for transforming core samples into relative permeabilities and capillary pressure.

E

E.2.1. DESCRIPTION OF THE PORE SPACE

The pore space in this project is characterized using a 3D voxel representation of Berea sandstone, serving as the foundation for the networks utilized, as shown in Figure E.6. Subsequently, a topologically equivalent network is generated, incorporating properties extracted from the original voxel representation.

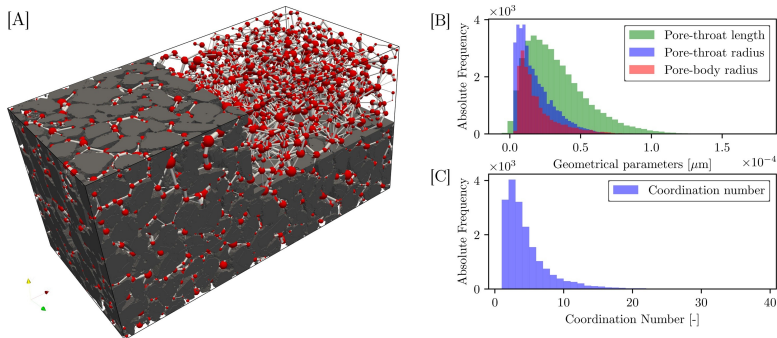


Figure E.6: A. The Nubian Sandstone pore-network is visualized in three dimensions (3D) with a domain size of $1.4 \times 1.4 \times 2.8 \text{ mm}^3$. The solid phase is represented in gray in the voxel SRXTM image, while the extracted pore elements are overlaid. The pore bodies are depicted as red spheres, and the pore throats are illustrated as gray cylinders, although they are scaled down for better visualization. B. Histograms are presented to display the distribution of pore-body radii, pore-throat radii, and pore-throat lengths in the extracted pore network of the Nubian Sandstone. C. The coordination number (Z), which represents the number of connections per pore, is shown in the pore network of the Nubian Sandstone, illustrating the distribution of this parameter [190]. Source: Adapted from Hefny et al. (2020) under CC BY License.

The extracted equivalent network from the rock sample comprises interconnected "pore bodies" connected by "pore throats." These pore throats are uniform conduits with varying cross-sectional shapes, such as circles, squares, and triangles, based on the

This section is taken from PhD thesis [189].

shape factor values ($G = A/P^2$, where A is the cross-sectional area and P is the perimeter length), as illustrated in Figure E.7.

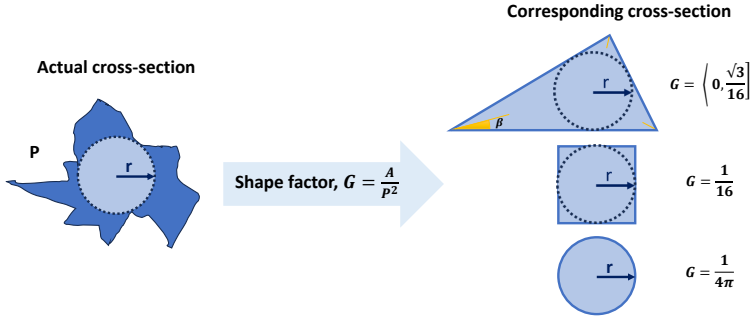


Figure E.7: The shape factor, derived from the area and perimeter of the actual cross-section, categorizes elements into three groups—triangular, square, or circular—depending on the specific value of the shape factor [189].

In triangular cross-sections, the corner half-angles, represented by β_1 , β_2 , and β_3 , are subject to the constraint $\beta_1 \leq \beta_2 \leq \beta_3 \leq \frac{\pi}{2}$. The value of β_2 is randomly determined within the range defined by equation E.1. Subsequently, β_1 and β_3 are calculated using the following equations:

$$\begin{aligned} \beta_{2,\min} &= \arctan \left\{ \frac{2}{\sqrt{3}} \cos \left(\frac{\arccos(-12\sqrt{3}G) + 4\pi}{3} \right) \right\} \\ \beta_{2,\max} &= \arctan \left\{ \frac{2}{\sqrt{3}} \cos \left(\frac{\arccos(-12\sqrt{3}G)}{3} \right) \right\} \\ \beta_1 &= -\frac{1}{2}\beta_2 + \frac{1}{2} \arcsin \left(\frac{\tan \beta_2 + 4G}{\tan \beta_2 - 4G} \sin \beta_2 \right) \\ \beta_3 &= \frac{\pi}{2} - \beta_1 - \beta_2 \end{aligned} \quad (\text{E.1})$$

Here, β represents the corner half-angle, and G denotes the shape factor.

Early network models often assumed circular cross-sections for simplicity. However, circular shapes have limitations as they cannot accommodate more than one fluid in a stable configuration within a single pore. As a result, they do not allow the formation of films or layers of additional phases during displacement processes. In contrast, real pore shapes observed in thin-section images of rocks are highly irregular and contain numerous corners. Experimental evidence has shown that in pores with angular cross-sections, the wetting phase can occupy the corners while the non-wetting phase occupies the central region. These corner-wetting films enhance phase connectivity and can reduce the trapping level of the defending phase. Therefore, network models with circular pore elements are unable to accurately predict experiments where film flow plays a crucial role.

The calculation of the threshold capillary entry pressure can be performed using equation E.2:

$$\begin{aligned}
 E_o^i &= \frac{\pi}{2} - \theta_i - \beta_i \\
 E_2^i &= \frac{\cos\theta_i + \beta_i}{\sin\beta_i} \cos\beta_i \\
 P_{c,PD}^e(\theta_r) &= \frac{\sigma}{r} \cos\beta_r \left(1 + \sqrt{1 - \frac{4G\Sigma_{i=0}^n (E_2^i - E_o^i)}{\cos^2(\theta_r)}} \right)
 \end{aligned}
 \tag{E.2}$$

In the equations above, θ_i represents the receding contact angle, β_i denotes the corner half-angle, and σ and r are parameters related to surface tension and pore radius, respectively.

E.2.2. FLOW PROCESS: DRAINAGE AND IMBIBITION

The **primary drainage** process involves a gradual increase in imposed capillary pressure, leading to the invasion of available elements until further invasion becomes impossible. The flow chart in Figure E.8 illustrates the steps involved in primary drainage.

E

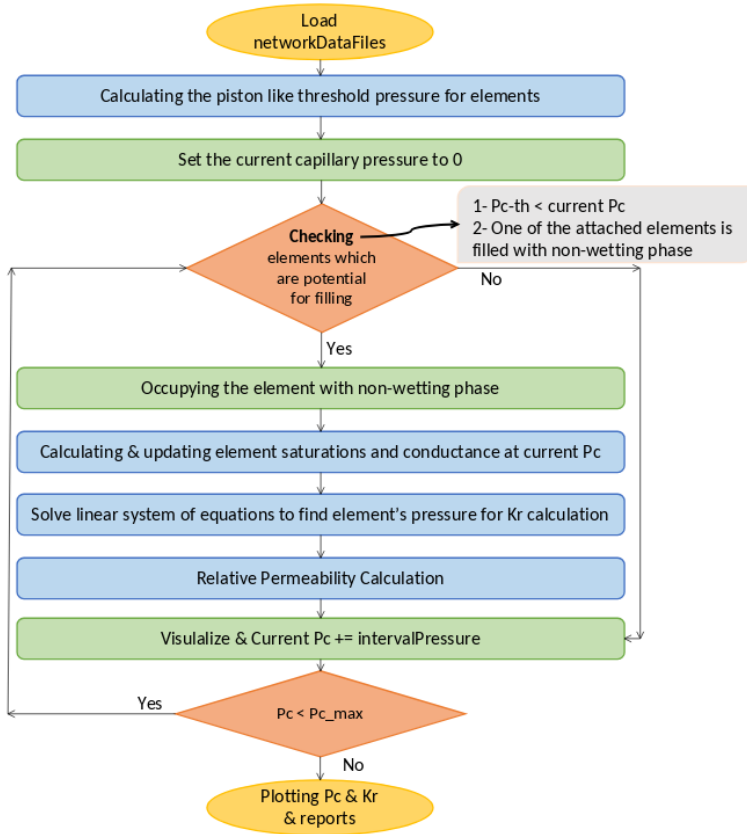


Figure E.8: Flow chart illustrating the sequential steps of the primary drainage process.

In the case of **secondary imbibition**, the angular cross-section of the pores allows the wetting phase to remain at the corners of the elements after primary drainage. Therefore, in addition to the piston-like mechanism, other mechanisms such as pore-body filling and snap-off play a role in secondary imbibition, as shown in Figure E.9.

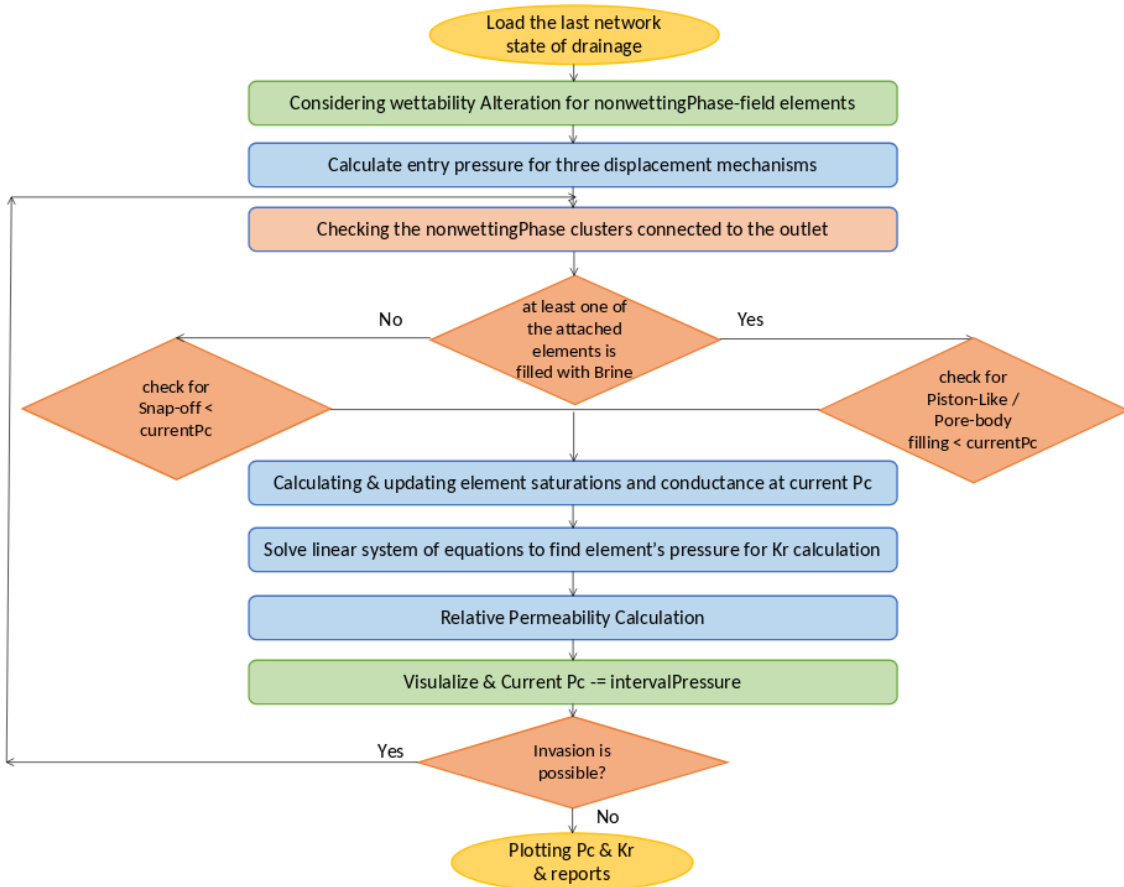


Figure E.9: Flow chart illustrating the sequential steps of the secondary imbibition process.

E.2.3. THRESHOLD CAPILLARY PRESSURES

The threshold capillary pressures associated with each mechanism are explained below and illustrated in Figure E.10.

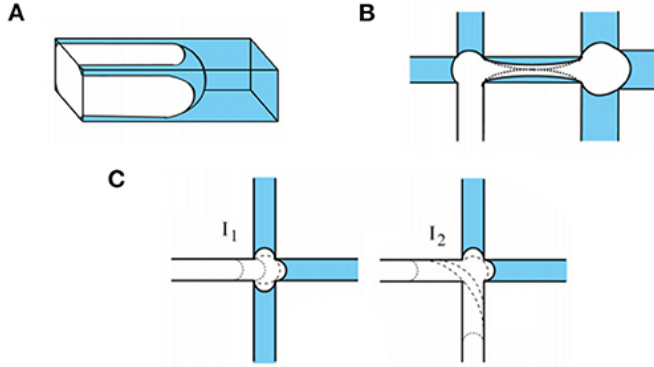


Figure E.10: The schematic diagram illustrates various processes in a rectangular tube: A. The drainage process is depicted using a piston-type displacement, where non-wetting phase is represented in white and wetting-phase in blue. B. The imbibition process showcases the snap-off phenomenon occurring in a pore-throat. C. Pore-body filling is illustrated, along with I1 and I2 events, during the imbibition process, again with non-wetting phase shown in white and wetting-phase shown in blue, I1 and I2 demonstrated cooperated pore-body filling with one and two pore throats filled with non-wetting-phase [191]. Source: Adapted from Kohanpour et al. et al. (2022) under CC BY License.

E

Piston-like displacement:

In this mechanism, the center of the pore throat is invaded by the fluid residing in the center of the neighboring pore body. Hysteresis in contact angle during this cycle leads to a hinging fluid interface between receding and advancing values. The hinging contact angle ($\theta_{h,i}$) and the distance from the corner apex (b_i) are calculated using the following equations:

$$E_1^i = \frac{\cos(\theta_i + \beta_i)}{\sin(\beta_i)}$$

$$\theta_{h,i}(P_c) = \arccos\left(\frac{P_c}{P_c^{max}} \cos(\theta_r + \beta_i)\right) - \beta_i \quad (E.3)$$

$$b_i(P_c, \theta_{h,i}) = \frac{\sigma}{P_c} E_1^i$$

Here, P_c^{max} represents the maximum pressure during the drainage cycle. The capillary entry pressure for piston-like displacement in spontaneous imbibition is iteratively calculated by solving equation E.4:

$$\theta_i = \min\left\{\theta_{h,i}\left(\frac{\sigma}{r_{PL}}\right), \theta_a\right\}$$

$$\theta_{h,i}(P_c) = \arccos\left(\frac{P_c}{P_c^{max}} \cos(\theta_r + \beta_i)\right) - \beta_i$$

$$b_i(P_c, \theta_{h,i}) = \frac{\sigma}{P_c} E_1^i \quad (E.4)$$

$$r_{PL} = \frac{\frac{r^2}{4G} + r_{PL}^2 \sum_{i=1}^n (E_2^i - E_0^i)}{2r_{PL} \sum_{i=1}^n E_0^i + \left(\frac{r}{2G} - 2r_{PL} \sum_{i=1}^n E_1^i\right) \cos(\theta_a)}$$

The imbibition process is considered spontaneous until the maximum advancing contact angle is reached. The equation to calculate the maximum advancing contact angle is given:

$$\theta_{a,max} = \arccos \left(\frac{-4G \sum_{i=1}^n \cos(\theta_r + \beta_i)}{\left(\frac{r P_c^{max}}{\sigma} \right) - \cos(\theta_r) + 4nG \sin(\theta_r)} \right) \quad (E.5)$$

Based on the above equations, three cases are considered for the threshold capillary pressure of the piston-like mechanism (equation E.6):

$$P_{c,PL}^e = \begin{cases} \frac{\sigma}{r_{PL}} & \text{if } \theta_a \leq \theta_{a,max} \\ \frac{2\sigma \cos(\theta_a)}{r} & \text{if } \theta_{a,max} < \theta_a < \frac{\pi}{2} + \min(\beta_i) \\ -P_{c,PD}^e (\pi - \theta_a) & \text{if } \theta_a \geq \frac{\pi}{2} + \min(\beta_i) \end{cases} \quad (E.6)$$

The first case corresponds to spontaneous imbibition, while the other cases refer to forced imbibition processes.

Cooperative pore-body filling:

Pore-body filling occurs when the fluid in the center of the pore body is displaced by invading fluid in the neighboring pore throat. The threshold capillary pressure in this mechanism depends on the number of pore throats filled with the non-wetting phase. If only one connecting pore throat is oil-filled, the calculation is similar to the piston-like mechanism. For other cases, the following equation is used (equation E.7):

$$\bar{R}n = \left[r_0 + W^{(n)} \frac{\sum n - \text{touples} W_{jk\dots n} (r_j + r_k + \dots + r_n)}{\sum_{jk\dots n} W_{jk\dots n}} \right] / \cos \theta_a \quad (E.7)$$

where \bar{R} represents the radius of curvature of the fluid interface, n is the number of oil-filled pore throats, r_0 is the radius of the pore body, r_i is the radius of the pore throat, θ_a is the advancing contact angle, $W_{jk\dots n}$ is a uniform random weight between zero and one, and $W^{(n)}$ allocates relative importance to each mechanism based on the given values (equation E.8):

$$W^{(2)} = 0.72;; W^{(3)} = 0.45;; W^{(4)} = 1.2;; W^{(5)} = 1.5;; W^{(n>5)} = 5 \quad (E.8)$$

Snap-off:

Snap-off is another mechanism where the phase in the corners swells and displaces the fluid in the center of the element. If the advancing contact angle is less than the maximum value given in equation E.9, spontaneous snap-off can occur. Otherwise, imbibition is forced, and the threshold capillary pressure for this mechanism is calculated using equation E.10:

$$\theta_{a,max} = \frac{\pi}{2} - \min(\beta_i) \quad (E.9)$$

$$r_{SO,ij} = r \frac{\cot(\beta_i) + \cot(\beta_j)}{E_1^i + E_1^j}$$

$$P_{c,SO}^e = \begin{cases} \frac{\sigma}{\min(r_{SOij})} & \text{if } \theta_a \leq \theta_{a,max} \\ P_c^{max} \frac{\cos(\theta_a + \min(\beta_i))}{\cos(\theta_r + \min(\beta_i))} & \text{if } \theta_{a,max} < \theta_a < \pi - \min(\beta_i) \\ P_c^{max} \frac{-1}{\cos(\theta_r + \min(\beta_i))} & \text{if } \theta_a \geq \pi - \min(\beta_i) \end{cases} \quad (\text{E.10})$$

Secondary imbibition, also known as mixed invasion-percolation and ordinary percolation process, is different from drainage in that the capillary pressure is gradually decreased, and elements are invaded in descending order of their threshold capillary pressure.

E.2.4. TRANSPORT PROPERTIES

The determination of macroscopic fluid transport properties, such as absolute permeability, relative permeabilities of each phase, and capillary pressure, can be achieved by analyzing the entire pore network.

Absolute permeability is calculated by the simulating single-phase flow on the fully saturated network and solving Darcy's law (equation 5.8). The viscosity of the single-phase fluid (μ_p), length (L), and cross-sectional area (A) of the network are used in the equation. By imposing a potential drop at two parallel surfaces of the network, the total flow rate ($Q_{total,sp}$) is obtained.

$$K = \frac{\mu_p Q_{total,sp} L}{A(\Phi_{inlet} - \Phi_{outlet})} \quad (\text{E.11})$$

To calculate the relative permeability of each phase, the total flow rate of phase p in multiphase flow (Q_{tmp}) is divided by the total flow rate (Q_{tsp}) using equation 5.9.

$$K_{rp} = \frac{Q_{tmp}}{Q_{tsp}} \quad (\text{E.12})$$

Mass conservation at each pore body i is written to find the total flow rate, as shown in equation 5.10, where j refers to all the pore throats connected to pore i.

$$\sum_j q_{p,ij} = 0 \quad (\text{E.13})$$

The assumptions made include considering incompressible fluid and neglecting viscous pressure drops compared to the capillary pressure. The volumetric flow rate between two pore bodies i and j is calculated using the Hagen-Poiseuille equation (equation 5.11), where L represents the length of elements E.11.

$$q_{p,ij} = \frac{g_{p,ij}}{L_{ij}} (\Phi_{p,i} - \Phi_{p,j}) \quad (\text{E.14})$$

Solving a linear set of mass conservation equations allows the calculation of pore body pressures. This linear system of mass conservation equations is depicted below:

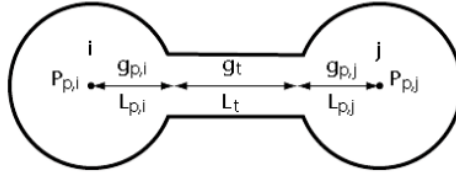


Figure E.11: Fluid conductance between two neighboring pore bodies i and j.

$$\begin{bmatrix}
 \sum \frac{g_{j,i}}{l_{j,i}} & -\frac{g_{j,i}}{l_{j,i}} & 0 & \dots & -\frac{g_{j,i}}{l_{j,i}} & 0 & 0 \\
 -\frac{g_{j,i}}{l_{j,i}} & \sum \frac{g_{j,i}}{l_{j,i}} & -\frac{g_{j,i}}{l_{j,i}} & \dots & 0 & -\frac{g_{j,i}}{l_{j,i}} & 0 \\
 0 & -\frac{g_{j,i}}{l_{j,i}} & \sum \frac{g_{j,i}}{l_{j,i}} & \dots & 0 & 0 & -\frac{g_{j,i}}{l_{j,i}} \\
 \vdots & \vdots & \vdots & \ddots & \vdots & \vdots & \vdots \\
 -\frac{g_{j,i}}{l_{j,i}} & 0 & 0 & \dots & \sum \frac{g_{j,i}}{l_{j,i}} & -\frac{g_{j,i}}{l_{j,i}} & 0 \\
 0 & -\frac{g_{j,i}}{l_{j,i}} & 0 & \dots & -\frac{g_{j,i}}{l_{j,i}} & \sum \frac{g_{j,i}}{l_{j,i}} & -\frac{g_{j,i}}{l_{j,i}} \\
 0 & 0 & -\frac{g_{j,i}}{l_{j,i}} & \dots & 0 & -\frac{g_{j,i}}{l_{j,i}} & \sum \frac{g_{j,i}}{l_{j,i}}
 \end{bmatrix}
 \times
 \begin{bmatrix}
 P_1 \\
 \vdots \\
 P_i \\
 \vdots \\
 P_n
 \end{bmatrix}
 =
 \begin{bmatrix}
 C_{-1,i} \times P_{inlet} \\
 \vdots \\
 \vdots \\
 C_{-1,i} \times P_{inlet} \\
 0 \\
 C_{0,i} \times P_{outlet} \\
 \vdots \\
 \vdots \\
 C_{0,i} \times P_{outlet}
 \end{bmatrix}$$

• Single-phase Conductance

In the case of single-phase flow under laminar conditions, the Hagen-Poiseuille formula can be applied to elements with a circular cross-sectional area. The formula is given by equation E.15. Patzek and Silin have also provided analytical formulas for equilateral triangles and squares. For triangular cross-sections, the conductance is calculated using equation E.16, while for square cross-sections, it is determined using equation E.17.

$$g_p = 0.5 \frac{GA^2}{\mu_p} \quad (\text{E.15})$$

$$g_p = 0.6 \frac{GA^2}{\mu_p} \quad (\text{E.16})$$

$$g_p = 0.5623 \frac{GA^2}{\mu_p} \quad (\text{E.17})$$

• Two-phase Conductance

In the case of multiphase flow, angular elements differ from circular ones as they have two phases. The wetting phase occupies the corners, while the non-wetting phase resides in the central bulk volume of the elements. Therefore, different areas and conductance values are used for each phase. The expressions for calculating

the area opened to flow corresponding to the cross-section of the elements are given as follows:

For circular cross-sections:

$$A_t = \pi R^2 \quad (\text{E.18})$$

For triangular cross-sections:

$$A_t = \frac{R^2}{4G} \quad (\text{E.19})$$

For square cross-sections:

$$A_t = 4R^2 \quad (\text{E.20})$$

The corner area in elements with angular cross-sections is determined by equation E.21. If the condition $\theta + \beta = \frac{\pi}{2}$ is satisfied, the corner area is given by the second expression in equation E.21.

$$A_c = R^2 \left(\cos \theta (\cot \beta - \cos \theta - \sin \theta) + \theta + \beta - \frac{\pi}{2} \right) \quad (\text{E.21})$$

$$A_c = \left(R \frac{\cos(\theta + \beta)}{\sin(\beta)} \right)^2 \sin \beta \cos \beta; \quad \text{if } \theta + \beta = \frac{\pi}{2}$$

The conductance of the elements to the wetting phase in the corners is calculated using the following equation:

$$g = \frac{A_c^2 (1 - \sin \beta)^2 (\phi_2 \cos \theta - \phi_1) \phi_3^2}{12\mu (\sin \beta)^2 (1 - \phi_3)^2 (\phi_2 + \phi_1)^2} \quad \text{if } \theta_1 \leq \pi/2 - \beta \quad (\text{E.22})$$

$$g = \frac{A_c^2 \tan \beta (1 - \sin \beta)^2 \phi_3^2}{12\mu (\sin \beta)^2 (1 - \phi_3)(1 + \phi_3)^2} \quad \text{if } \theta_1 > \pi/2 - \beta \quad (\text{E.23})$$

where:

$$\begin{aligned} \phi_1 &= \left(\frac{\pi}{2} - \beta - \theta \right) \\ \phi_2 &= \cot \beta \cos \theta - \sin \theta \\ \phi_3 &= \left(\frac{\pi}{2} - \beta \right) \tan \beta \end{aligned} \quad (\text{E.24})$$

BIBLIOGRAPHY

- [1] Niklas Heinemann et al. “Enabling large-scale hydrogen storage in porous media – the scientific challenges”. In: *Energy Environ. Sci.* 14 (2 2021), pp. 853–864. URL: <http://dx.doi.org/10.1039/D0EE03536J>.
- [2] Mojdeh Delshad et al. “Hydrogen Storage Assessment in Depleted Oil Reservoir and Saline Aquifer”. In: *Energies* 15.21 (2022). ISSN: 1996-1073. URL: <https://www.mdpi.com/1996-1073/15/21/8132>.
- [3] Samuel Krevor et al. “Subsurface carbon dioxide and hydrogen storage for a sustainable energy future”. In: *Nature Reviews Earth & Environment* 4.2 (2023), pp. 102–118.
- [4] Emmanuel I. Epelle et al. “Perspectives and prospects of underground hydrogen storage and natural hydrogen”. In: *Sustainable Energy Fuels* 6 (14 2022), pp. 3324–3343. URL: <http://dx.doi.org/10.1039/D2SE00618A>.
- [5] Esuru Rita Okoroafor, Sarah D. Saltzer, and Anthony R. Kavscek. “Toward underground hydrogen storage in porous media: Reservoir engineering insights”. In: *International Journal of Hydrogen Energy* 47.79 (2022), pp. 33781–33802. ISSN: 0360-3199. URL: <https://www.sciencedirect.com/science/article/pii/S0360319922033584>.
- [6] Maksim Lysyy et al. “Hydrogen Relative Permeability Hysteresis in Underground Storage”. In: *Geophysical Research Letters* 49.17 (2022), e2022GL100364.
- [7] Johannes Miodic et al. “Underground hydrogen storage: a review”. In: *Geological Society, London, Special Publications* 528.1 (2023), SP528–2022–88.
- [8] Wolf Tilmann Pfeiffer and Sebastian Bauer. “Subsurface Porous Media Hydrogen Storage – Scenario Development and Simulation”. In: *Energy Procedia* 76 (2015). European Geosciences Union General Assembly 2015 - Division Energy, Resources and Environment, EGU 2015, pp. 565–572. ISSN: 1876-6102. URL: <http://www.sciencedirect.com/science/article/pii/S1876610215016483>.
- [9] W.T. Pfeiffer et al. “Porous Media Hydrogen Storage - Dimensioning and Induced Hydraulic, Thermal and Chemical Effect”. In: 2015.1 (2015), pp. 1–5. ISSN: 2214-4609. URL: <https://www.earthdoc.org/content/papers/10.3997/2214-4609.201414259>.
- [10] S. van Gessel, H. Hajibeygi, and et al. *Hydrogen TCP-Task 42 (2023), “Underground Hydrogen Storage: Technology Monitor Report”, 153 pages including appendices*. Tech. rep. Apr. 2023. URL: <https://www.ieahydrogen.org/tasks-reports/>.
- [11] A. Ebrahimiyehta. “Characterization of geochemical interactions and migration of hydrogen in sandstone sedimentary formations : application to geological storage”. PhD thesis. Orleans University, France, 2017.

- [12] M. Panfilov. "4 - Underground and pipeline hydrogen storage". In: *Compendium of Hydrogen Energy*. Ed. by Ram B. Gupta, Angelo Basile, and T. Nejat Veziroğlu. Woodhead Publishing Series in Energy. Woodhead Publishing, 2016, pp. 91–115. ISBN: 978-1-78242-362-1. URL: <http://www.sciencedirect.com/science/article/pii/B9781782423621000043>.
- [13] Behrouz Nemati et al. "A Sustainable Approach for Site Selection of Underground Hydrogen Storage Facilities Using Fuzzy-Delphi Methodology". In: *Settlements and Spatial Planning* 6 (2020), pp. 5–16.
- [14] K. Ramesh Kumar et al. "Geomechanical simulation of energy storage in salt formations". In: *Scientific Reports* 11 (2021), pp. 1–24.
- [15] Radosław Tarkowski. "Underground hydrogen storage: Characteristics and prospects". In: *Renewable and Sustainable Energy Reviews* 105 (2019), pp. 86–94. ISSN: 1364-0321. URL: <http://www.sciencedirect.com/science/article/pii/S1364032119300528>.
- [16] Dilara Gulcin Caglayan et al. "Technical potential of salt caverns for hydrogen storage in Europe". In: *International Journal of Hydrogen Energy* 45.11 (2020), pp. 6793–6805. ISSN: 0360-3199. URL: <http://www.sciencedirect.com/science/article/pii/S0360319919347299>.
- [17] Kavan Khaledi et al. "Stability and serviceability of underground energy storage caverns in rock salt subjected to mechanical cyclic loading". In: *International Journal of Rock Mechanics and Mining Sciences* 86 (2016), pp. 115–131. ISSN: 1365-1609. URL: <http://www.sciencedirect.com/science/article/pii/S1365160916300612>.
- [18] A. Sainz-Garcia et al. "Assessment of feasible strategies for seasonal underground hydrogen storage in a saline aquifer". In: *International Journal of Hydrogen Energy* 42.26 (2017), pp. 16657–16666. ISSN: 0360-3199. URL: <http://www.sciencedirect.com/science/article/pii/S0360319917319420>.
- [19] Katarzyna Luboń and Radosław Tarkowski. "Numerical simulation of hydrogen injection and withdrawal to and from a deep aquifer in NW Poland". In: *International Journal of Hydrogen Energy* 45.3 (2020), pp. 2068–2083. ISSN: 0360-3199. URL: <http://www.sciencedirect.com/science/article/pii/S0360319919342363>.
- [20] T Rudolph. "Underground Hydrogen Storage—Current Developments and Opportunities". In: *EAGE/DGMK Joint Workshop on Underground Storage of Hydrogen*. Vol. 2019. European Association of Geoscientists & Engineers. 2019, pp. 1–2.
- [21] Neda Hassannayebi. "An assessment of underground hydrogen storage: Transport, geochemistry, and bioactivity". PhD thesis. Leoben University, Austria, 2019.
- [22] Birger Hagemann. "Numerical and analytical modeling of gas mixing and bio-reactive transport during underground hydrogen storage". PhD thesis. Clausthal University of Technology, Germany and the University of Lorraine, France, 2017.

- [23] Steven Flesch et al. "Hydrogen underground storage—Petrographic and petro-physical variations in reservoir sandstones from laboratory experiments under simulated reservoir conditions". In: *International Journal of Hydrogen Energy* 43.45 (2018), pp. 20822–20835. ISSN: 0360-3199. URL: <http://www.sciencedirect.com/science/article/pii/S0360319918329793>.
- [24] Markus Pichler. *Assesment of hydrogen - rock interactions during geological storage of CH₄ - H₂ mixtures*. Master thesis. 2013.
- [25] Christina Hemme. "Storage of Gases in Deep Geological Structures: Spatial and Temporal Hydrogeochemical Processes Evaluated and Predicted by the Development and Application of Numerical Modeling". PhD thesis. Clausthal University of Technology, Germany, 2019.
- [26] A. Amid, D. Mignard, and M. Wilkinson. "Seasonal storage of hydrogen in a depleted natural gas reservoir". In: *International Journal of Hydrogen Energy* 41.12 (2016), pp. 5549–5558. ISSN: 0360-3199. URL: <http://www.sciencedirect.com/science/article/pii/S036031991531781X>.
- [27] Dieter Pudlo et al. "The H2STORE Project: Hydrogen Underground Storage – A Feasible Way in Storing Electrical Power in Geological Media?" In: *Clean Energy Systems in the Subsurface: Production, Storage and Conversion*. Berlin, Heidelberg: Springer Berlin Heidelberg, 2013, pp. 395–412.
- [28] Laurent Truche et al. "Sulphide mineral reactions in clay-rich rock induced by high hydrogen pressure. Application to disturbed or natural settings up to 250°C and 30bar". In: *Chemical Geology* 351 (2013), pp. 217–228. ISSN: 0009-2541. URL: <http://www.sciencedirect.com/science/article/pii/S0009254113002313>.
- [29] M. Panfilov et al. "Bio-reactive Two-phase Transport and Population Dynamics in Underground Storage of Hydrogen: Natural Self-organisation". In: *Conference Proceedings, ECMOR XIII - 13th European Conference on the Mathematics of Oil Recovery, Sep 2012, cp-307-00048*. European Association of Geoscientists and Engineers, 2012, p. 265. ISBN: 978-90-73834-30-9.
- [30] Mikhail Panfilov. "Underground Storage of Hydrogen: In Situ Self-Organisation and Methane Generation". In: *Transport in Porous Media* 85.3 (2010), pp. 841–865. URL: <https://doi.org/10.1007/s11242-010-9595-7>.
- [31] G Strobel, B Hagemann, and L Ganzer. "History Matching of Bio-reactive Transport in an Underground Hydrogen Storage Field Case". In: *EAGE/DGMK Joint Workshop on Underground Storage of Hydrogen*. Vol. 2019. European Association of Geoscientists & Engineers. 2019, pp. 1–3.
- [32] WA van Rooijen et al. "Interfacial tensions, solubilities, and transport properties of the H₂/H₂O/NaCl system: A molecular simulation study". In: *Journal of Chemical & Engineering Data* (2023).
- [33] P.O. Carden and L. Paterson. "Physical, chemical and energy aspects of underground hydrogen storage". In: *International Journal of Hydrogen Energy* 4.6 (1979), pp. 559–569. ISSN: 0360-3199. URL: <http://www.sciencedirect.com/science/article/pii/S0360319979900831>.

- [34] Laurent Truche et al. “Kinetics of pyrite to pyrrhotite reduction by hydrogen in calcite buffered solutions between 90 and 180°C: Implications for nuclear waste disposal”. In: *Geochimica et Cosmochimica Acta* 74.10 (2010), pp. 2894–2914. ISSN: 0016-7037.
- [35] Leila Hashemi, Martin Blunt, and Hadi Hajibeygi. “Pore-scale modelling and sensitivity analyses of hydrogen-brine multiphase flow in geological porous media”. In: *Scientific Reports* 11.1 (2021), p. 8348. URL: <https://doi.org/10.1038/s41598-021-87490-7>.
- [36] Tom Bultreys et al. “Verifying Pore Network Models of Imbibition in Rocks Using Time-Resolved Synchrotron Imaging”. In: *Water Resources Research* 56.6 (2020). e2019WR026587 10.1029/2019WR026587, e2019WR026587.
- [37] *Hydrogen Storage*: <https://www.energy.gov/eere/fuelcells/hydrogen-storage>. URL: <https://www.energy.gov/eere/fuelcells/hydrogen-storage>.
- [38] Anozie Ebigo, Fabrice Golfier, and Michel Quintard. “A coupled, pore-scale model for methanogenic microbial activity in underground hydrogen storage”. In: *Advances in Water Resources* 61 (2013), pp. 74–85. ISSN: 0309-1708. URL: <http://www.sciencedirect.com/science/article/pii/S0309170813001565>.
- [39] Paolo Gabrielli et al. “Seasonal energy storage for zero-emissions multi-energy systems via underground hydrogen storage”. In: *Renewable and Sustainable Energy Reviews* 121 (2020), p. 109629. ISSN: 1364-0321. URL: <http://www.sciencedirect.com/science/article/pii/S1364032119308366>.
- [40] Ahmet Ozarslan. “Large-scale hydrogen energy storage in salt caverns”. In: *International Journal of Hydrogen Energy* 37.19 (2012). HYFUSEN, pp. 14265–14277. ISSN: 0360-3199. URL: <http://www.sciencedirect.com/science/article/pii/S0360319912017417>.
- [41] Howard B. J. Stone, Ivo Veldhuis, and R. Neil Richardson. “Underground hydrogen storage in the UK”. In: *Geological Society, London, Special Publications* 313.1 (2009), pp. 217–226. ISSN: 0305-8719.
- [42] Michael L. Szulczewski et al. “Lifetime of carbon capture and storage as a climate-change mitigation technology”. In: *Proceedings of the National Academy of Sciences* 109.14 (2012), pp. 5185–5189. ISSN: 0027-8424.
- [43] S Foh et al. *Underground hydrogen storage. Final report. [Salt caverns, excavated caverns, aquifers and depleted fields]*. Tech. rep. Brookhaven National Lab., Upton, NY (USA), Dec. 1979.
- [44] Birger Hagemann, Mikhail Panfilov, and Leonhard Ganzer. “Multicomponent gas rising through water with dissolution in stratified porous reservoirs – Application to underground storage of H₂ and CO₂”. In: *Journal of Natural Gas Science and Engineering* 31 (2016), pp. 198–213. ISSN: 1875-5100. URL: <http://www.sciencedirect.com/science/article/pii/S1875510016301251>.
- [45] Martin J. Blunt. *Multiphase Flow in Permeable Media: A Pore-Scale Perspective*. Cambridge University Press, 2017.

- [46] V. Joekar-Niasar, S. M. Hassanizadeh, and A. Leijnse. “Insights into the Relationships Among Capillary Pressure, Saturation, Interfacial Area and Relative Permeability Using Pore-Network Modeling”. In: *Transport in Porous Media* 74.2 (2008), pp. 201–219. URL: <https://doi.org/10.1007/s11242-007-9191-7>.
- [47] Qingrong Xiong, Todor G Baychev, and Andrey P Jivkov. “Review of pore network modelling of porous media: Experimental characterisations, network constructions and applications to reactive transport”. In: *Journal of contaminant hydrology* 192 (Sept. 2016), pp. 101–117. ISSN: 0169-7722. URL: <https://doi.org/10.1016/j.jconhyd.2016.07.002>.
- [48] S. Majid Hassanizadeh, Michael A. Celia, and Helge K. Dahle. “Dynamic Effect in the Capillary Pressure–Saturation Relationship and its Impacts on Unsaturated Flow”. In: *Vadose Zone Journal* 1.1 (2002), pp. 38–57.
- [49] Masa Prodanovic and Steven L. Bryant. “A level set method for determining critical curvatures for drainage and imbibition”. In: *Journal of Colloid and Interface Science* 304.2 (2006), pp. 442–458. ISSN: 0021-9797. URL: <http://www.sciencedirect.com/science/article/pii/S0021979706007764>.
- [50] Ayaz Mehmani, Maša Prodanović, and Farzam Javadpour. “Multiscale, Multiphysics Network Modeling of Shale Matrix Gas Flows”. In: *Transport in Porous Media* 99.2 (2013), pp. 377–390. URL: <https://doi.org/10.1007/s11242-013-0191-5>.
- [51] Per H. Valvatne and Martin J. Blunt. “Predictive pore-scale modeling of two-phase flow in mixed wet media”. In: *Water Resources Research* 40.7 (2004).
- [52] *Pore-Scale Modelling and Imaging*. URL: <https://www.imperial.ac.uk/earth-science/research/research-groups/pore-scale-modelling/>.
- [53] M. J. Oak, L. E. Baker, and D. C. Thomas. “Three-Phase Relative Permeability of Berea Sandstone”. In: *Journal of Petroleum Technology* 42.08 (1990), pp. 1054–1061. URL: <https://doi.org/10.2118/17370-PA>.
- [54] Pal-Eric Oren and Stig Bakke. “Reconstruction of Berea sandstone and pore-scale modelling of wettability effects”. In: *Journal of Petroleum Science and Engineering* 39.3 (2003). Reservoir Wettability, pp. 177–199. ISSN: 0920-4105. URL: <http://www.sciencedirect.com/science/article/pii/S0920410503000627>.
- [55] Tom Bultreys, Luc Van Hoorebeke, and Veerle Cnudde. “Multi-scale, micro-computed tomography-based pore network models to simulate drainage in heterogeneous rocks”. In: *Advances in Water Resources* 78 (2015), pp. 36–49.
- [56] Mohammad Piri and Martin J. Blunt. “Three-dimensional mixed-wet random pore-scale network modeling of two- and three-phase flow in porous media. I. Model description”. In: *Phys. Rev. E* 71 (2 Feb. 2005), p. 026301. URL: <https://link.aps.org/doi/10.1103/PhysRevE.71.026301>.
- [57] T.W. Patzek and D.B. Silin. “Shape Factor and Hydraulic Conductance in Non-circular Capillaries: I. One-Phase Creeping Flow”. In: *Journal of Colloid and Interface Science* 236.2 (2001), pp. 295–304. ISSN: 0021-9797. URL: <http://www.sciencedirect.com/science/article/pii/S0021979700974137>.

- [58] I. Fatt. "The Network Model of Porous Media". In: *Transactions of the AIME* 207.01 (1956), pp. 144–181. URL: <https://doi.org/10.2118/574-G>.
- [59] A. E. Yekta et al. "Determination of Hydrogen–Water Relative Permeability and Capillary Pressure in Sandstone: Application to Underground Hydrogen Injection in Sedimentary Formations". In: *Transport in Porous Media* 122.2 (2018), pp. 333–356. URL: <https://doi.org/10.1007/s11242-018-1004-7>.
- [60] Norman R. Morrow. "The Effects of Surface Roughness On Contact: Angle With Special Reference to Petroleum Recovery". In: *Journal of Canadian Petroleum Technology* 14.04 (1975), p. 13. URL: <https://doi.org/10.2118/75-04-04>.
- [61] *Micro-CT Images and Networks*. URL: <https://www.imperial.ac.uk/engineering/departments/earth-science/research/research-groups/pore-scale-modelling/>.
- [62] McMillan Burton, Navanit Kumar, and Steven L. Bryant. "CO₂ injectivity into brine aquifers: Why relative permeability matters as much as absolute permeability". In: *Energy Procedia* 1.1 (2009). Greenhouse Gas Control Technologies 9, pp. 3091–3098. ISSN: 1876-6102. URL: <http://www.sciencedirect.com/science/article/pii/S1876610209007322>.
- [63] Leila Hashemi et al. "Contact Angle Measurement for Hydrogen/Brine/Sandstone System Using Captive-Bubble Method Relevant for Underground Hydrogen Storage". In: *Advances in Water Resources* (2021), p. 103964.
- [64] Stefan Iglauer, Muhammad Ali, and Alireza Keshavarz. "Hydrogen Wettability of Sandstone Reservoirs: Implications for Hydrogen Geo-Storage". In: *Geophysical Research Letters* 48.3 (2021), e2020GL090814. URL: <https://doi.org/10.1029/2020GL090814>.
- [65] Katherine A. Klise et al. "Automated contact angle estimation for three-dimensional X-ray microtomography data". In: *Advances in Water Resources* 95 (2016). Pore scale modeling and experiments, pp. 152–160. ISSN: 0309-1708. URL: <https://www.sciencedirect.com/science/article/pii/S0309170815002651>.
- [66] Zhishang Liu, James E. McClure, and Ryan T. Armstrong. "Influence of wettability on phase connectivity and electrical resistivity". In: *Phys. Rev. E* 98 (4 Oct. 2018), p. 043102. URL: <https://link.aps.org/doi/10.1103/PhysRevE.98.043102>.
- [67] S. Berg et al. "Connected pathway relative permeability from pore-scale imaging of imbibition". In: *Advances in Water Resources* 90 (2016), pp. 24–35. ISSN: 0309-1708. URL: <https://www.sciencedirect.com/science/article/pii/S0309170816300112>.
- [68] P. Kunz, S. M. Hassanizadeh, and U. Nienke. "A Two-Phase SPH Model for Dynamic Contact Angles Including Fluid–Solid Interactions at the Contact Line". In: *Transport in Porous Media* 122.2 (2018), pp. 253–277. URL: <https://doi.org/10.1007/s11242-018-1002-9>.

- [69] M. Rucker et al. "The Effect of Mixed Wettability on Pore-Scale Flow Regimes Based on a Flooding Experiment in Ketton Limestone". In: *Geophysical Research Letters* 46.6 (2019), pp. 3225–3234.
- [70] S.-Y Yang et al. "Mechanisms for contact angle hysteresis and advancing contact angles". In: *Journal of Petroleum Science and Engineering* 24.2 (1999), pp. 63–73. ISSN: 0920-4105. URL: <https://www.sciencedirect.com/science/article/pii/S0920410599000492>.
- [71] Anna V. Prydatko et al. "Contact angle measurement of free-standing square-millimeter single-layer graphene". In: *Nature Communications* 9.1 (2018), p. 4185. URL: <https://doi.org/10.1038/s41467-018-06608-0>.
- [72] Anna E. Peksa, Karl-Heinz A.A. Wolf, and Pacelli L.J. Zitha. "Bentheimer sandstone revisited for experimental purposes". In: *Marine and Petroleum Geology* 67 (2015), pp. 701–719. ISSN: 0264-8172. URL: <https://www.sciencedirect.com/science/article/pii/S0264817215300106>.
- [73] R. Farajzadeh et al. "Cation Exchange in the Presence of Oil in Porous Media". In: *ACS Earth and Space Chemistry* 1.2 (Apr. 20, 2017), pp. 101–112. URL: <https://doi.org/10.1021/acsearthspacechem.6b00015>.
- [74] L Kapetas et al. "Effect of permeability on foam-model parameters-an integrated approach from coreflood experiments through to foam diversion calculations". In: *IOR 2015-18th European Symposium on Improved Oil Recovery*. European Association of Geoscientists & Engineers. 2015, cp-445.
- [75] G. Laskaris. "Effect of Surfactant Concentration, Water Treatment Chemicals, Fatty Acids and Alcohols on Foam Behavior in Porous Media and in Bulk". In: 2015.
- [76] N. Shojai Kaveh et al. "Wettability Evaluation of a CO₂/Water/Bentheimer Sandstone System: Contact Angle, Dissolution, and Bubble Size". In: *Energy & Fuels* 28.6 (June 19, 2014), pp. 4002–4020. URL: <https://doi.org/10.1021/ef500034j>.
- [77] D. Li, P. Cheng, and A.W. Neumann. "Contact angle measurement by axisymmetric drop shape analysis (ADSA)". In: *Advances in Colloid and Interface Science* 39 (1992), pp. 347–382. ISSN: 0001-8686. URL: <https://www.sciencedirect.com/science/article/pii/0001868692800656>.
- [78] Michael Batzle and Zhijing Wang. "Seismic properties of pore fluids". In: *GEO-PHYSICS* 57.11 (1992), pp. 1396–1408.
- [79] Eric W Lemmon, Marcia L Huber, and Jacob W Leachman. "Revised Standardized Equation for Hydrogen Gas Densities for Fuel Consumption Applications". In: *Journal of research of the National Institute of Standards and Technology* 113.6 (Dec. 1, 2008), pp. 341–350. URL: <https://pubmed.ncbi.nlm.nih.gov/27096133>.

- [80] Ahmed Al-Yaseri et al. "N₂+CO₂+NaCl brine interfacial tensions and contact angles on quartz at CO₂ storage site conditions in the Gippsland basin, Victoria/Australia". In: *Journal of Petroleum Science and Engineering* 129 (2015), pp. 58–62. ISSN: 0920-4105. URL: <http://www.sciencedirect.com/science/article/pii/S0920410515000273>.
- [81] Foad Haeri et al. "CO₂-Brine Contact Angle Measurements on Navajo, Nugget, Bentheimer, Bandera Brown, Berea, and Mt. Simon Sandstones". In: *Energy & Fuels* 34.5 (May 21, 2020), pp. 6085–6100. URL: <https://doi.org/10.1021/acs.energyfuels.0c00436>.
- [82] Jong-Won Jung and Jiamin Wan. "Supercritical CO₂ and Ionic Strength Effects on Wettability of Silica Surfaces: Equilibrium Contact Angle Measurements". In: *Energy & Fuels* 26.9 (Sept. 20, 2012), pp. 6053–6059. URL: <https://doi.org/10.1021/ef300913t>.
- [83] Leila Hashemi et al. "A comparative study for H₂-CH₄ mixture wettability in sandstone porous rocks relevant to underground hydrogen storage". In: *Advances in Water Resources* 163 (2022), p. 104165.
- [84] Aliakbar Hassanpouryouzband et al. "Offshore Geological Storage of Hydrogen: Is This Our Best Option to Achieve Net-Zero?" In: *ACS Energy Letters* 6.6 (2021), pp. 2181–2186.
- [85] Davood Zivar, Sunil Kumar, and Jalal Foroozesh. "Underground hydrogen storage: A comprehensive review". In: *International Journal of Hydrogen Energy* 46.45 (2021). Hydrogen Separation, Production and Storage, pp. 23436–23462. ISSN: 0360-3199. URL: <https://www.sciencedirect.com/science/article/pii/S0360319920331426>.
- [86] Alina Kabuth et al. "Energy storage in the geological subsurface: dimensioning, risk analysis and spatial planning: the ANGUS+ project". In: *Environmental Earth Sciences* 76.1 (2017), pp. 1–17.
- [87] JB Taylor et al. "Technical and economic assessment of methods for the storage of large quantities of hydrogen". In: *International Journal of Hydrogen Energy* 11.1 (1986), pp. 5–22.
- [88] Christopher Schaber, Patrick Mazza, and Roel Hammerschlag. "Utility-scale storage of renewable energy". In: *The Electricity Journal* 17.6 (2004), pp. 21–29.
- [89] AB Walters. "Technical and environmental aspects of underground hydrogen storage". In: *1st World Hydrogen Energy Conference, Volume 2*. Vol. 2. 1976, 2B_65–2B_79.
- [90] Mikhail Panfilov, G Gravier, and S Fillacier. "Underground storage of H₂ and H₂-CO₂-CH₄ mixtures". In: *ECMOR X-10th European conference on the mathematics of oil recovery*. European Association of Geoscientists & Engineers. 2006, cp–23.
- [91] Olaf Kruck et al. "Assessment of the potential, the actors and relevant business cases for large scale and seasonal storage of renewable electricity by hydrogen underground storage in Europe". In: *KBB Undergr. Technol. GmbH* (2013).

- [92] RAG. “UNDERGROUND SUN STORAGE 2030”. In: (2021). URL: <https://www.rag-austria.at/forschung-innovation/underground-sun-storage-2030.html>.
- [93] Ariel Pérez et al. “Patagonia wind-hydrogen project: underground storage and methanation”. In: *de 21st World Hydrogen Energy Conference*. 2016.
- [94] M. Laban. “Hydrogen Storage in Salt Caverns: Chemical modelling and analysis of large-scale hydrogen storage in underground salt caverns”. In: *MSc Thesis* (2020), pp. 1–86.
- [95] Muhammad Ali et al. “Influence of pressure, temperature and organic surface concentration on hydrogen wettability of caprock; implications for hydrogen geo-storage”. In: *Energy Reports* 7 (2021), pp. 5988–5996. ISSN: 2352-4847.
- [96] Pierre-Gilles De Gennes. “Wetting: statics and dynamics”. In: *Reviews of modern physics* 57.3 (1985), p. 827.
- [97] Thomas Young. “III. An essay on the cohesion of fluids”. In: *Philosophical transactions of the royal society of London* 95 (1805), pp. 65–87.
- [98] Amer M Alhammadi et al. “In situ characterization of mixed-wettability in a reservoir rock at subsurface conditions”. In: *Scientific Reports* 7.1 (2017), pp. 1–9.
- [99] Muhammad Arif, Sidqi A Abu-Khamsin, and Stefan Iglauer. “Wettability of rock/CO₂/brine and rock/oil/CO₂-enriched-brine systems: Critical parametric analysis and future outlook”. In: *Advances in colloid and interface science* 268 (2019), pp. 91–113.
- [100] W. van Rooijen et al. “Microfluidics-based analysis of dynamic contact angles relevant for underground hydrogen storage”. In: *Under Review X* (2021), pp. X–X.
- [101] Scott Higgs et al. “In-situ hydrogen wettability characterisation for Underground Hydrogen Storage”. In: (2021).
- [102] RAG. “UNDERGROUND SUN STORAGE”. In: (2017). URL: https://www.underground-sun-storage.at/fileadmin/bilder/03_NEU_SUNSTORAGE/Downloads/Underground_%20Sun.Storage_Publizierbarer_Endbericht_English.pdf.
- [103] Aliakbar Hassanpouryouzband et al. “Thermodynamic and transport properties of hydrogen containing streams”. In: *Scientific Data* 7.1 (2020), pp. 1–14.
- [104] Mehmet Rasin Tek. *Underground storage of natural gas: theory and practice*. Vol. 171. Springer Science & Business Media, 2012.
- [105] Jesús Simon, Ana María Férriz, and Luis Carlos Correas. “HyUnder–hydrogen underground storage at large scale: case study Spain”. In: *Energy procedia* 73 (2015), pp. 136–144.
- [106] Alvaro Sainz-Garcia, Elena Abarca, and Fidel Grandia. “Efficiency and impacts of hythane (CH₄+ H₂) underground storage”. In: *EGU General Assembly Conference Abstracts*. 2016, EPSC2016–16603.
- [107] Maja Rucker et al. “The effect of mixed wettability on pore-scale flow regimes based on a flooding experiment in Ketton limestone”. In: *Geophysical Research Letters* 46.6 (2019), pp. 3225–3234. URL: <https://doi.org/10.1029/2018GL081784>.

- [108] Bin Pan et al. "Underground hydrogen storage: Influencing parameters and future outlook". In: *Advances in Colloid and Interface Science* (2021), p. 102473. URL: <https://doi.org/10.1016/j.cis.2021.102473>.
- [109] PO Carden and Lincoln Paterson. "Physical, chemical and energy aspects of underground hydrogen storage". In: *International Journal of Hydrogen Energy* 4.6 (1979), pp. 559–569. URL: [https://doi.org/10.1016/0360-3199\(79\)90083-1](https://doi.org/10.1016/0360-3199(79)90083-1).
- [110] Nicolas J. Alvarez, Lynn M. Walker, and Shelley L. Anna. "A non-gradient based algorithm for the determination of surface tension from a pendant drop: Application to low Bond number drop shapes". In: *Journal of Colloid and Interface Science* 333.2 (2009), pp. 557–562. ISSN: 0021-9797. URL: <https://www.sciencedirect.com/science/article/pii/S0021979709002161>.
- [111] Volker Hessel, Holger Lowe, and Steffen Hardt. *Chemical micro process engineering: fundamentals, modelling and reactions*. Vol. 1. John Wiley & Sons, 2004.
- [112] John C Berg. *An introduction to interfaces & colloids: the bridge to nanoscience*. World Scientific, 2010.
- [113] Jaroslaw Drelich. "The Effect of Drop (Bubble) Size on Contact Angle at Solid Surfaces". In: *The Journal of Adhesion* 63.1-3 (1997), pp. 31–51.
- [114] YT Florence Chow, Geoffrey C Maitland, and JP Martin Trusler. "Interfacial tensions of (H₂O+ H₂) and (H₂O+ CO₂+ H₂) systems at temperatures of (298–448) K and pressures up to 45 MPa". In: *Fluid Phase Equilibria* 475 (2018), pp. 37–44.
- [115] Bin Pan et al. "The interfacial properties of clay-coated quartz at reservoir conditions". In: *Fuel* 262 (2020), p. 116461.
- [116] URL: <https://dumux.org/docs/doxygen/releases/3.5/a18529.html>.
- [117] Zhenkai Bo et al. "Impact of experimentally measured relative permeability hysteresis on reservoir-scale performance of underground hydrogen storage (UHS)". In: *International Journal of Hydrogen Energy* (2023).
- [118] Andrey Ryazanov et al. "Pore scale network modelling of residual oil saturation in mixed-wet systems". PhD thesis. Heriot-Watt University, 2012.
- [119] Martin J Blunt et al. "Pore-scale imaging and modelling". In: *Advances in Water resources* 51 (2013), pp. 197–216.
- [120] Amir Raouf and S Majid Hassanzadeh. "A new method for generating pore-network models of porous media". In: *Transport in porous media* 81 (2010), pp. 391–407.
- [121] Roland Lenormand, Eric Touboul, and Cesar Zarcone. "Numerical models and experiments on immiscible displacements in porous media". In: *Journal of fluid mechanics* 189 (1988), pp. 165–187.
- [122] Mosayeb Shams. "Modelling two-phase flow at the micro-scale using a volume-of-fluid method". In: (2018).

- [123] Ahmed Hamdi Boujelben and Steven Robert McDougall. “Dynamic Pore Scale Modelling of Multiphase Flow during Application of EOR Techniques”. In: *19th European Symposium on Improved Oil Recovery: Price World Sustainable IOR in a Low Oil*. 2017.
- [124] J Koplik and TJ Lasseter. “Two-phase flow in random network models of porous media”. In: *Society of Petroleum Engineers Journal* 25.01 (1985), pp. 89–100.
- [125] Mohammed S Al-Gharbi and Martin J Blunt. “Dynamic network modeling of two-phase drainage in porous media”. In: *Physical Review E* 71.1 (2005), p. 016308.
- [126] Arash Aghaei and Mohammad Piri. “Direct pore-to-core up-scaling of displacement processes: Dynamic pore network modeling and experimentation”. In: *Journal of hydrology* 522 (2015), pp. 488–509.
- [127] Sidian Chen, Chaozhong Qin, and Bo Guo. “Fully Implicit Dynamic Pore-Network Modeling of Two-Phase Flow and Phase Change in Porous Media”. In: *Water Resources Research* 56.11 (2020), e2020WR028510.
- [128] K Weishaupt and R Helmig. “A Dynamic and Fully Implicit Non-Isothermal, Two-Phase, Two-Component Pore-Network Model Coupled to Single-Phase Free Flow for the Pore-Scale Description of Evaporation Processes”. In: *Water Resources Research* 57.4 (2021), e2020WR028772.
- [129] Senyou An et al. “Transition From Viscous Fingering to Capillary Fingering: Application of GPU-Based Fully Implicit Dynamic Pore Network Modeling”. In: *Water Resources Research* 56.12 (2020), e2020WR028149.
- [130] Yanbin Gong, Mohammad Sedghi, and Mohammad Piri. “Dynamic pore-scale modeling of residual fluid configurations in disordered porous media”. In: *E3S Web of Conferences*. Vol. 366. 2023, p. 01018.
- [131] Juan Li, Steven Robert McDougall, and Kenneth Stuart Sorbie. “Dynamic pore-scale network model (PNM) of water imbibition in porous media”. In: *Advances in Water Resources* 107 (2017), pp. 191–211.
- [132] Kilian Weishaupt. *Model concepts for coupling free flow with porous medium flow at the pore-network scale: from single-phase flow to compositional non-isothermal two-phase flow*. Stuttgart: Eigenverlag des Instituts für Wasser- und Umweltsystemmodellierung ..., 2020.
- [133] Hu Dong and Martin J. Blunt. “Pore-network extraction from micro-computerized-tomography images”. In: *Phys. Rev. E* 80 (3 Sept. 2009), p. 036307. URL: <https://link.aps.org/doi/10.1103/PhysRevE.80.036307>.
- [134] V Joekar-Niasar, S Majid Hassanizadeh, and HK Dahle. “Non-equilibrium effects in capillarity and interfacial area in two-phase flow: dynamic pore-network modelling”. In: *Journal of Fluid Mechanics* 655 (2010), pp. 38–71.
- [135] Tad W Patzek. “Verification of a complete pore network simulator of drainage and imbibition”. In: *Spe Journal* 6.02 (2001), pp. 144–156.
- [136] V Joekar-Niasar and SM Hassanizadeh. “Analysis of fundamentals of two-phase flow in porous media using dynamic pore-network models: A review”. In: *Critical reviews in environmental science and technology* 42.18 (2012), pp. 1895–1976.

- [137] Kristian Mogensen and Erling H Stenby. "A dynamic two-phase pore-scale model of imbibition". In: *Transport in Porous Media* 32.3 (1998), pp. 299–327.
- [138] Karsten E Thompson. "Pore-scale modeling of fluid transport in disordered fibrous materials". In: *AIChE Journal* 48.7 (2002), pp. 1369–1389.
- [139] V Joekar-Niasar et al. "Network model investigation of interfacial area, capillary pressure and saturation relationships in granular porous media". In: *Water Resources Research* 46.6 (2010).
- [140] Chao-Zhong Qin, S Majid Hassanizadeh, and Lucas M Van Oosterhout. "Pore-network modeling of water and vapor transport in the micro porous layer and gas diffusion layer of a polymer electrolyte fuel cell". In: *Computation* 4.2 (2016), p. 21.
- [141] Karim Khayrat and Patrick Jenny. "Subphase approach to model hysteretic two-phase flow in porous media". In: *Transport in porous media* 111.1 (2016), pp. 1–25.
- [142] Kishan Ramesh Kumar et al. "Comprehensive review of geomechanics of underground hydrogen storage in depleted reservoirs and salt caverns". In: *Journal of Energy Storage* 73 (2023), p. 108912. ISSN: 2352-152X.
- [143] A. Lassin, M. Dymitrowska, and M. Azaroual. "Hydrogen solubility in pore water of partially saturated argillites: Application to Callovo-Oxfordian clayrock in the context of a nuclear waste geological disposal". In: *Physics and Chemistry of the Earth, Parts A/B/C* 36.17 (2011). Clays in Natural and Engineered Barriers for Radioactive Waste Confinement, pp. 1721–1728. ISSN: 1474-7065. URL: <http://www.sciencedirect.com/science/article/pii/S1474706511002336>.
- [144] Marco [De Lucia] et al. "Measurements of H₂ Solubility in Saline Solutions under Reservoir Conditions: Preliminary Results from Project H₂STORE". In: *Energy Procedia* 76 (2015). European Geosciences Union General Assembly 2015 - Division Energy, Resources and Environment, EGU 2015, pp. 487–494. ISSN: 1876-6102. URL: <http://www.sciencedirect.com/science/article/pii/S1876610215016689>.
- [145] Daoyong Yang, Yongan Gu, and Paitoon Tontiwachwuthikul. "Wettability determination of the reservoir brine- reservoir rock system with dissolution of CO₂ at high pressures and elevated temperatures". In: *Energy & Fuels* 22.1 (2008), pp. 504–509.
- [146] John Mills, Masoud Riazi, and Mehran Sohrabi. "Wettability of common rock-forming minerals in a CO₂-brine system at reservoir conditions". In: *International symposium of the society of core analysts*. Society of Core Analysts Fredrickton, Canada. 2011, pp. 19–21.
- [147] Daniel Broseta, Nicolas Tonnet, and Virenkumar Shah. "Are rocks still water-wet in the presence of dense CO₂ or H₂S?" In: *Geofluids* 12.4 (2012), pp. 280–294.
- [148] Shibo Wang, Ian M Edwards, and Andres F Clarens. "Wettability phenomena at the CO₂-brine-mineral interface: implications for geologic carbon sequestration". In: *Environmental science & technology* 47.1 (2013), pp. 234–241.

- [149] Raheleh Farokhpoor et al. “Wettability behaviour of CO₂ at storage conditions”. In: *International Journal of Greenhouse Gas Control* 12 (2013), pp. 18–25. ISSN: 1750-5836. URL: <https://www.sciencedirect.com/science/article/pii/S1750583612002551>.
- [150] Matthew Andrew, Branko Bijeljic, and Martin J Blunt. “Pore-scale contact angle measurements at reservoir conditions using X-ray microtomography”. In: *Advances in Water Resources* 68 (2014), pp. 24–31.
- [151] Muhammad Arif et al. “CO₂ storage in carbonates: Wettability of calcite”. In: *International Journal of Greenhouse Gas Control* 62 (2017), pp. 113–121.
- [152] Mihaela S.P Stevar et al. “Wettability of calcite under carbon storage conditions”. In: *International Journal of Greenhouse Gas Control* 84 (2019), pp. 180–189. ISSN: 1750-5836. URL: <https://www.sciencedirect.com/science/article/pii/S1750583618308855>.
- [153] Martin Blunt and Peter King. “Relative permeabilities from two- and three-dimensional pore-scale network modelling”. In: *Transport in porous media* 6.4 (1991), pp. 407–433.
- [154] SH Lee, L Padmanabhan, and HA Al-Sunaidi. “Simulation of linear displacement experiments on massively parallel computers”. In: *SPE Journal* 1.03 (1996), pp. 327–340.
- [155] J Kamath et al. “Pore network modeling of laboratory experiments on heterogeneous carbonates”. In: *SPE Annual Technical Conference and Exhibition*. OnePetro. 1996.
- [156] S.C. van der Marck, T. Matsuura, and J. Glas. “Viscous and capillary pressures during drainage: Network simulations and experiments”. In: *Physical Review E - Statistical Physics, Plasmas, Fluids, and Related Interdisciplinary Topics* 56.5 (1997). cited By 31, pp. 5675–5687.
- [157] Eyvind Aker et al. “A two-dimensional network simulator for two-phase flow in porous media”. In: *Transport in porous media* 32.2 (1998), pp. 163–186.
- [158] Helge K Dahle and Michael A Celia. “A dynamic network model for two-phase immiscible flow”. In: *Computational Geosciences* 3.1 (1999), pp. 1–22.
- [159] Richard G Hughes and Martin J Blunt. “Pore scale modeling of rate effects in imbibition”. In: *Transport in Porous Media* 40.3 (2000), pp. 295–322.
- [160] George N Constantinides and Alkiviades C Payatakes. “Effects of precursor wetting films in immiscible displacement through porous media”. In: *Transport in porous media* 38.3 (2000), pp. 291–317.
- [161] Mohit Singh and Kishore K Mohanty. “Dynamic modeling of drainage through three-dimensional porous materials”. In: *Chemical Engineering Science* 58.1 (2003), pp. 1–18.
- [162] Hans Fredrik Nordhaug, M Celia, and Helge K Dahle. “A pore network model for calculation of interfacial velocities”. In: *Advances in Water Resources* 26.10 (2003), pp. 1061–1074.

- [163] Viet Hoai Nguyen et al. "The effect of displacement rate on imbibition relative permeability and residual saturation". In: *Journal of Petroleum Science and Engineering* 52.1-4 (2006), pp. 54–70.
- [164] David A DiCarlo. "Quantitative network model predictions of saturation behind infiltration fronts and comparison with experiments". In: *Water resources research* 42.7 (2006).
- [165] Mohammad Piri and Zuleima T Karpyn. "Prediction of fluid occupancy in fractures using network modeling and X-ray microtomography. II: Results". In: *Physical Review E* 76.1 (2007), p. 016316.
- [166] Vahid Joekar-Niasar and S Majid Hassanizadeh. "Effect of fluids properties on non-equilibrium capillarity effects: Dynamic pore-network modeling". In: *International Journal of Multiphase Flow* 37.2 (2011), pp. 198–214.
- [167] V Joekar-Niasar and SM Hassanizadeh. "Specific interfacial area: The missing state variable in two-phase flow equations?" In: *Water Resources Research* 47.5 (2011).
- [168] Jonathan S Ellis and Aimy Bazylak. "Dynamic pore network model of surface heterogeneity in brine-filled porous media for carbon sequestration". In: *Physical Chemistry Chemical Physics* 14.23 (2012), pp. 8382–8390.
- [169] Paul S Hammond and Evren Unsal. "A dynamic pore network model for oil displacement by wettability-altering surfactant solution". In: *Transport in porous media* 92.3 (2012), pp. 789–817.
- [170] Qiang Sheng and Karsten Thompson. "Dynamic coupling of pore-scale and reservoir-scale models for multiphase flow". In: *Water Resources Research* 49.9 (2013), pp. 5973–5988.
- [171] U Bagudu, SR McDougall, and EJ Mackay. "Pore-to-Core-Scale Network Modelling of CO₂ Migration in Porous Media". In: *Transport in Porous Media* 110.1 (2015), pp. 41–79.
- [172] Xinwo Huang, Karl W Bandilla, and Michael A Celia. "Multi-physics pore-network modeling of two-phase shale matrix flows". In: *Transport in Porous Media* 111.1 (2016), pp. 123–141.
- [173] Shuang Cindy Cao, Sheng Dai, and Jongwon Jung. "Supercritical CO₂ and brine displacement in geological carbon sequestration: Micromodel and pore network simulation studies". In: *International Journal of Greenhouse Gas Control* 44 (2016), pp. 104–114.
- [174] Qiang Sheng and Karsten Thompson. "A unified pore-network algorithm for dynamic two-phase flow". In: *Advances in Water Resources* 95 (2016), pp. 92–108.
- [175] Mohamed Regaieg and Arthur Moncorgé. "Adaptive dynamic/quasi-static pore network model for efficient multiphase flow simulation". In: *Computational Geosciences* 21.4 (2017), pp. 795–806.
- [176] Jianhui Yang et al. "Pore to pore validation of pore network modelling against micromodel experiment results". In: *Computational Geosciences* 21.5 (2017), pp. 849–862.

- [177] Ahmed Boujelben et al. “Pore network modelling of low salinity water injection under unsteady-state flow conditions”. In: *Journal of Petroleum Science and Engineering* 165 (2018), pp. 462–476.
- [178] Masakazu Gesheo et al. “Dynamic Pore Network Modeling of Two-Phase Flow Through Fractured Porous Media: Direct Pore-to-Core Up-scaling of Displacement Processes”. In: ().
- [179] Magnus Aa Gjennestad et al. “Stable and efficient time integration of a dynamic pore network model for two-phase flow in porous media”. In: *Frontiers in Physics* 6 (2018), p. 56.
- [180] Thomas Sweijen et al. “Dynamic pore-scale model of drainage in granular porous media: The pore-unit assembly method”. In: *Water resources research* 54.6 (2018), pp. 4193–4213.
- [181] Chao-Zhong Qin and Harald van Brummelen. “A dynamic pore-network model for spontaneous imbibition in porous media”. In: *Advances in Water Resources* 133 (2019), p. 103420.
- [182] Chao-Zhong Qin et al. “Dynamic pore-network modeling of air-water flow through thin porous layers”. In: *Chemical Engineering Science* 202 (2019), pp. 194–207.
- [183] X Yin et al. “Dynamic Pore-Network Models Development”. In: *Advances in Mathematical Methods and High Performance Computing*. Springer, 2019, pp. 337–356.
- [184] Santanu Sinha et al. “A dynamic network simulator for immiscible two-phase flow in porous media”. In: *arXiv preprint arXiv:1907.12842* (2019).
- [185] Yanbin Gong and Mohammad Piri. “Pore-to-core upscaling of solute transport under steady-state two-phase flow conditions using dynamic pore network modeling approach”. In: *Transport in Porous Media* 135.1 (2020), pp. 181–218.
- [186] Bauyrzhan K Primkulov et al. “Wettability and Lenormand’s diagram”. In: *Journal of Fluid Mechanics* 923 (2021).
- [187] Taha Sochi. *Pore-Scale Modeling of Non-Newtonian Flow in Porous Media*. 2007.
- [188] Andrey Ryazanov. “Pore-Scale Network Modelling of Residual Oil Saturation in Mixed-Wet Systems”. PhD thesis. Heriot-Watt University, Edinburgh, 2012.
- [189] Per Henrik Valvatne. “Predictive pore-scale modelling of multiphase flow”. PhD thesis. Imperial College London (University of London), 2003.
- [190] Mahmoud Hefny et al. “Synchrotron-based pore-network modeling of two-phase flow in Nubian Sandstone and implications for capillary trapping of carbon dioxide”. In: *International Journal of Greenhouse Gas Control* 103 (2020), p. 103164. ISSN: 1750-5836. URL: <https://www.sciencedirect.com/science/article/pii/S1750583620305892>.
- [191] Amir H Kohanpur, Yu Chen, and Albert J Valocchi. “Using direct numerical simulation of pore-level events to improve pore-network models for prediction of residual trapping of CO₂”. In: *Frontiers in Water* 3 (2022), p. 710160.

CURRICULUM VITÆ

Leila HASHEMI



05-01-1994 Born in Tehran, Iran.

EDUCATION

2012–2016 Shiraz University, Shiraz, Iran
Bachelor of Science in Petroleum (Reservoir) Engineering

2017–2019 Petroleum University of Technology, Tehran, Iran
Master of Science in Reservoir Management

2020–2024 Delft University of Technology, Delft, the Netherlands
Delft Institute of Applied Mathematics (DIAM)
Faculty of Electrical Eng., Mathematics and Computer Science (EEMCS)
Ph.D. in Computational Mathematics and Numerical Analysis

WORK EXPERIENCE AND INTERNSHIPS

- Apr 2016 - Jun 2016 Researcher, **Shiraz University, Iran**
"Analysis of the effect of chemicals on the emulsion stability"
- Jun 2016 - Sep 2016 Reservoir Engineer, **Research Institute of Petroleum Industry (RIPI), Iran**
Intern in reservoir rock and fluid research group, "gas chromatography"
- Sep 2016 - Sep 2017 Researcher, **Palafarayandrastin Company, Iran**
R&D team, "Develop chemical productions for oil and gas industry specifically on the application of gel polymer to control water production for oil and gas reservoir"
- Feb 2018 - Apr 2018 Researcher, **Research Center of Petroleum University of Tech., Iran**
"The evaluation of national and international gas companies to develop key performance indicators in the reservoir"
- Mar 2022 - Apr 2022 Researcher, **Stuttgart University, Germany**
Visiting researcher, "Dynamic pore network modelling using DuMux"
- Jul 2023 - Sep 2023 Researcher intern, **TNO, The Netherlands**
"Geochemical and Flow Numerical Modeling of Hydrogen Storage in the Depleted Gas Fields"

SCIENTIFIC CONTRIBUTIONS

JOURNAL PAPERS

5. **L. Hashemi**, C. Vuik, Critical assessment of the validity of quasi-static pore network modelling in the application of underground hydrogen storage, *Advances in Water Resources*, submitted.
4. W. van Rooijen, **L. Hashemi**, M. Boon, W. Glerum, R. Farajzadeh, H. Hajibeygi, [Microfluidics-based analysis of dynamic contact angles relevant for underground hydrogen storage](#), *Advances in Water Resources*, **164**, (2022) 104221.
3. **L. Hashemi**, M. Boon, W. Glerum, R. Farajzadeh, H. Hajibeygi, [A comparative study for H₂-CH₄ mixture wettability in sandstone porous rocks relevant to underground hydrogen storage](#), *Advances in Water Resources*, **163**, (2022) 104165.
2. **L. Hashemi**, W. Glerum, R. Farajzadeh, H. Hajibeygi, [Contact angle measurement for hydrogen/brine/sandstone system using captive-bubble method relevant for underground hydrogen storage](#), *Advances in Water Resources*, **154**, (2021) 103964.
1. **L. Hashemi**, M. Blunt, H. Hajibeygi, [Pore-scale modelling and sensitivity analyses of hydrogen-brine multiphase flow in geological porous media](#), *Scientific reports*, **11**, 1 (2021) 1-13.

ORAL PRESENTATIONS

4. Pore-scale simulation of hydrogen transport in porous media. Burgers Symposium. Lunteren, The Netherlands. 31 May - 01 June 2023.
3. Pore scale simulation of hydrogen transport in porous media. International Society of Porous Media (InterPore). Edinburgh, Scotland. 22 - 25 May 2023.
2. Modelling and Experimental study of hydrogen transport at micro scale in porous media. Porous Media Tea Time Talk (PMTTT). (Online). 5 October 2021.
1. Pore-scale modelling and sensitivity analyses of hydrogen-brine multiphase flow in geological porous media. International Society of Porous Media (InterPore). (Online). 31 May - 04 June 2021.

POSTER PRESENTATIONS

2. Pore-scale simulation of hydrogen transport in porous media. Society of Applied Mathematics (SIAM) Conference on Computational Science and Engineering in the Geoscience (GS). Bergen, Norway. 19 - 22 June 2023.
1. Pore-scale simulation of hydrogen transport in porous media. Society of Applied Mathematics (SIAM) Conference on Computational Science and Engineering (CSE). Amsterdam, The Netherlands. 26 February - 03 March 2023.

RESEARCH ACTIVITIES

3. Challenger winner at Hackathon in Society of Applied Mathematics (SIAM) Conference on Computational Science and Engineering (CSE). Amsterdam, The Netherlands. 26 February - 03 March 2023.
2. Participation at The Study Group Mathematics with Industry (SWI). Research report on "The heat transition – Mathematical models and optimization". Groningen, The Netherlands. 30 January - 03 February 2023.
1. Participation at the Pore Network Modelling workshop. Stuttgart, Germany. 26 - 28 September 2022.

TEACHING ASSISTANT WORK

3. Subsurface Storage, Delft University of Technology. 2022.
2. Subsurface Storage, Delft University of Technology. 2021.
1. Subsurface Storage, Delft University of Technology. 2020.

SUPERVISING WORK

4. Master project (together with Dr. H. Hajibeygi), Static Contact Angle Measurements for Subsurface Hydrogen Storage, W. Glerum, Delft University of Technology. 2021.
3. Master project (together with Dr. H. Hajibeygi), Dynamic Contact Angle measurement using microfluidic experiments relevant for Hydrogen Subsurface Storage, W. van Rooijen, Delft University of Technology. 2021 - 2022.
2. Bachelor project (together with Dr. H. Hajibeygi), Underground Storage for the North Sea Hydrogen Production Plant: a conceptual study, J. Yassien, Delft University of Technology. 2020.
1. Master project (together with Dr. H. Hajibeygi), Seasonal Hydrogen Storage in Dutch Depleted Gas Reservoirs: A Feasibility Study for The Netherlands, T. Visser, Delft University of Technology. 2020.

ACKNOWLEDGEMENTS

I am grateful to acknowledge the invaluable assistance, support, and involvement of numerous individuals who made this remarkable four-year journey and all its accompanying adventures possible. Although these words may appear modest, I want to express my deep appreciation for these extraordinary individuals.

My sincere thanks go to my supervisor, **Prof. Hadi Hajibeygi**, who recognized the potential in my work during my MSc thesis and invited me to join his research team at TU Delft's reservoir engineer section. This journey began in January 2020, albeit with a challenging start due to the onset of the pandemic. Despite the difficulties, I am grateful for the warm welcome and support from my colleagues (**Mousa, Kishan, Fanxiang, Sara, Yuhang, Johno**) at TU Delft and newfound friends (**Yosra, Ramin, Farinaz, Mousa, Hoda, Sayeh, Solmaz**) in Delft. I would also like to express my heartfelt thanks to my mentor during my MSc thesis, **MohammadHossein Golestan**. His guidance extended beyond research challenges, helping me grow not only in my academic pursuits but also as an individual, especially during the transition to the Netherlands.

Hadi, you provided me with the opportunity to introduce pore network modeling to MSc students as part of the Energy Storage course, which brought me great joy in sharing my knowledge on this fascinating topic. Additionally, it was a distinct pleasure to collaborate with **Prof. Martin Blunt** and **Dr. Sajjad Foroughi** from Imperial College London, which resulted in my first publication on the intriguing subject of underground hydrogen storage. This collaboration allowed us to address critical knowledge gaps, marking the next significant step in my research journey at TU Delft.

During ongoing pandemic restrictions, I embarked on experimental work in the laboratory, under the co-supervising of **Dr. Rouhi Farajzadeh**. That gave me the opportunity to co-supervise master's students, **Wuis Glerum** and **Willemijn van Rooijen**. Later, I had the privilege of working alongside **Dr. Maartje Boon** during the final stages of my experimental work. I believe that the time spent in the laboratory was particularly transformative for my journey, allowing me to develop greater resilience while gaining invaluable experiences. I would like to also thank the lab staff in CiTG laboratory who helped us in different stages of the experiments: **Michiel, Karel, Marc, Joost, Ellen**, and other colleagues that made the atmosphere more friendly and active, including **Sian** and **Chris**."

Thanks to Hadi for giving me the opportunity to assist in the committee program for organizing the first online InterPore2020 conference, which proved to be a valuable learning experience. I also want to express my gratitude to my colleagues who worked together on this endeavor: **Prof. Majid Hassanizadeh, Karolin, Amy, and Megan**.

Recognizing the potential for further research, funding was secured, and I transitioned to the Math department under the supervision of **Prof. Cornelis (Kees) Vuik**. I would like to send a big and special thanks to you for not only supervising me during our

weekly meetings on my research work but also for helping me rebuild my confidence and being there to listen whenever I needed to talk. Your professional and personal characters have always been an inspiration to me, and I am grateful to have had the chance to have you as my guide on this journey of PhD.

I would also like to express my appreciation to **Prof. Arnold Heemink, Prof. Timo Heimovaara, Prof. Martin Blunt, Prof. Karsten Thompson, Prof. Maša Prodanović, and Prof. Bill Rossen** on my PhD committee for taking the time to read my thesis and providing valuable suggestions. Additionally, I would like to extend my thanks to **Prof. Arnold Heemink** for his participation in the committee of my Go/No-Go assessment.

I am really thankful for the friendly atmosphere and the great colleagues who made it a nice place to grow personally and academically. I want to say thanks to my colleagues and friends from DIAM, including **Alice, Xiaoshan, Ye, Hugo, Jun, Gijs, Merel, Elisa, Buu-Van, Kewang, Giorgio, Artur, Ziliang, Anouk, Daniel, and Jingqiang**. I hold all our lunch and coffee times dear, as they provided chances for great conversations, and I'm thankful for the connections we made. **Alice**, you were the first person who came to my office to welcome me warmly, and your support has meant a lot to me. I also want to thank my office mates, **Ye, Hugo, and Jun**, for being open to starting yoga sessions in our office. **Hugo**, I will never forget our commitment to doing yoga even when we went to Efteling. Later on, **Gijs** joined our office, and I appreciate him practicing Dutch speaking with me sometimes. **Xiaoshan** and **Giorgio**, I'm excited that you encouraged me to join you for bouldering and climbing sessions, and we found a shared passion for it. **Merel**, the lunchtime moments we spent together, sometimes combined with chess games, are special to me. **Merel** and **Xiaoshan**, it has been now three years that each new year for us is combined with a 30-day yoga challenge, which reminds me of our very nice commitments and teamwork. **Ye**, when we both moved to the numerical analysis office, we became active colleagues, and our regular presence in the office allowed us to create great memories. Our joint participation in the Hackathon, along with **Kewang**, where we not only attended but also won the challenge, was a nice experience.

I want to say a big thank you to the **ADMIRE group** and all my colleagues, both new and old, for all the teamwork we've had since I joined TU Delft. Even when COVID-19 forced us to work from home during the time I had my office in the Geoscience and Engineering department, we stayed connected through online meetings. **Mousa**, a special thank you to you for always being kind and offering advice whenever I needed it. Your experience as the senior PhD in the group was incredibly helpful. You've always been clear and rational in your advice, and I appreciate that. **Kishan** and I joined the group at around the same time, and over these four years, we've become good friends while learning and exploring our research journeys together. **Willemijn**, I'm thrilled that you continued your research work with our team after your master's thesis. It allowed us to become friends, support each other, and learn together. Our trips to conferences in Edinburgh and Bergen, along with **Sara, Herminio, Thejas, Maartje, Ziliang, Mengjie**, and the extended hiking trip afterward, created unforgettable memories in my mind, with **Willemijn, Kishan, Fanxiang**, and other colleagues **Mohsen, Michiel, and Xiaoming**. I would also like to mention other bachelor's and master's students that I had the chance to work with **Artur, Nordin, Thomas, Pieter, Jonas**. I had the opportunity to organize our weekly progress meetings during your theses, which provided a valuable experience.

My academic journey took me to international conferences, collaborations in Germany, and learning experiences in dynamic pore network modeling. I would like to thank Prof. Rainer Helmig for hosting me in Stuttgart.

I was fortunate to have **Christianne Wilmink** as my mentor. We first met during a cooperation course at the Graduate School, and our connection grew stronger over time. She was always there for guidance and support, which played a big role in my personal growth and self-discovery. She also introduced me to the Women Leading Energy Transition network, where I connected with inspiring women who helped and motivated me, including **Anouk Creusen**.

Participating in Dutch language courses not only facilitated my integration into the culture of the Netherlands but also led to the making of new friendships. These connections, nurtured with individuals including **Lucia, Samikshya, Carla, Maria, Andres, Tutu, Ines, Paulina, Kamila, Dajana** have been great in initiating various activities and gatherings. Together we have built lasting bonds and shared memorable moments. So I extend my heartfelt gratitude to my dear friends. A special thank goes to **Shokofeh**, for her kindness and support in my journey. Despite not knowing me initially, she became a valued friend, and through this friendship, I had the chance to get to know **Maryam** and a special connection between us.

Later, I voluntarily participated in a research software development workshop. This workshop greatly enhanced my programming skills and gave me valuable insights into developing research software while considering FAIRness if it. I am grateful to **Maurits** and their team, who made the 12-week workshop both informative and enjoyable.

One of the most rewarding experiences of my journey was my internship at TNO, which provided me with a unique opportunity to collaborate with experts from diverse backgrounds and expand my professional network. During this enriching experience, I had the privilege of working closely with individuals who guided and supported me throughout. I would like to express my sincere gratitude to my supervisors, **Dr. Cintia Goncalves Machado** and **Dr. Paul Egbert**, for their invaluable mentorship and for granting me the chance to have this remarkable learning experience.

I would like to express my heartfelt gratitude to my dear family. Despite the long distances that separated us, your unwavering support and encouragement never wavered. You have always stood by my side, motivating me to pursue my goals, no matter where or when. I could not have come this far without your help and support. To **my grandparents**, you have always been there for me and your support has been a constant presence throughout my life. Whenever faced with challenges, the thought of you served as a source of inspiration, urging me to press on and make you proud. I hope that I have been successful in this endeavor. To **my parents**, I am thankful for raising us to be independent and fearless, instilling in us the determination to follow our dreams, no matter how hard the path may be. Your guidance has been invaluable. I also want to extend my special gratitude to **my sister** and **brother**, who have been my closest friends throughout my life. The three of us have continually encouraged and supported each other whenever needed.

*Leila Hashemi
Delft, October 2, 2023*

